Conceptual research of a multi megawatt downwind turbine

Wanke, Gesine

Link to article, DOI:
10.11581/dtu:00000060

Publication date:
2019

Document Version
Publisher's PDF, also known as Version of record

Conceptual Research of a Multi Megawatt Downwind Turbine

Department of Wind Energy PhD Report 2019

Gesine Wanke

DOI number: https://doi.org/10.11581/dtu:00000060
DTU Wind Energy PhD-0094

December 2019

DTU Wind Energy
Department of Wind Energy

Authors: Gesine Wanke
Title: Conceptual Research of a Multi Megawatt Downwind Turbine
Department: Wind Energy

2019

Project Period:
December 2016 - December 2019

Education:
PhD

Supervisors:
Morten H. Hansen, Professor, DTU Wind Energy (December 2016 to October 2017)
Torben J. Larsen, Senior Scientist, DTU Wind Energy (November 2017 to March 2019)
Frederik Zahle, Senior Scientist, DTU Wind Energy (since April 2019)

Co-Supervisors:
Jens I. Madsen, Senior Specialist and Vice President, Suzlon Blade Science Center (since December 2016)
Thomas Buhl, Vice President, Suzlon Blade Science Center (December 2016 to June 2019)
Leonardo Bergami, Senior Engineer, Suzlon Blade Science Center (since December 2016)
Torben J. Larsen, Senior Scientist, DTU Wind Energy (Mai 2017 to October 2017)
Morten H. Hansen, Professor, Mads Clausen Institute, SDU (November 2017 to January 2019)
David R. Verelst, Scientist, DTU Wind Energy (since February 2019)

DTU Wind Energy is a department of the Technical University of Denmark with a unique integration of research, education, innovation and public/private sector consulting in the field of wind energy. Our activities develop new opportunities and technology for the global and Danish exploitation of wind energy. Research focuses on key technical-scientific fields, which are central for the development, innovation and use of wind energy and provides the basis for advanced education.

DTU Wind Energy has a staff of approximately 240 and a further 35 PhD-students, spread across 38 different nationalities. The variety of research, education, innovation, testing and consultancy is reflected in the employment profile which includes faculty with research and teaching responsibilities, researchers and technical academic staff, highly skilled technicians and administrative staff.

Our facilities are situated at DTU Risø Campus and at DTU Lyngby Campus. Furthermore the department is running the national test stations in Høvsøre and Østerild.

Technical University of Denmark
Department of Wind Energy
Frederiksborgvej 399
Building 118
4000 Rosilde
Denmark

www.vindenergi.dtu.dk

Abstract

This thesis investigates the advantages and disadvantages of a downwind wind turbine rotor concept compared to an upwind rotor concept. A commercial Suzlon 2.1 MW upwind turbine is used as the baseline and converted into a downwind configuration by moving the rotor downwind from the tower. The effect of the conversion on the loads is investigated. Dynamic stability investigations are made regarding the difference in edgewise damping and a free-yawing downwind option. Finally, new rotors are designed for the upwind and the downwind configuration to evaluate differences in turbine mass and cost. The overall objective of the thesis is to evaluate the possible economic benefits of the downwind configuration compared to the upwind configuration for the chosen example turbine.

A comparison of a full design load basis simulated with HAWC2 according to IEC-standard shows that the minimum blade tip to tower clearance can be increased by the turbine conversion. The downwind configuration shows a 10% lower extreme flapwise blade root moment due to the coning direction. The tradeoff is a 0.75% lower annual energy production and a 14% higher extreme tower bending moment as moments from the thrust and gravity on the rotor nacelle assembly are aligned. The tower shadow effect increases the blade fatigue loads, and for the edgewise direction a decrease in damping leads to further load increase.

Consequently, the difference in edgewise damping of the downwind configuration in comparison to the upwind configuration is studied. This shows that the turbine conversion changes the interaction of the aerodynamic forces, the rotor, and the tower torsional motion. This interaction influences the out-of-plane component of the edgewise modes which is the main contributor to the change in damping. Turbine design parameter such as cone angle and tower torsional stiffness could be used to increase the edgewise damping.

Furthermore, a free yawing downwind configuration is investigated as it could reduce the complexity of the yaw system. The equilibrium free yaw angle of the example turbine can be larger than 19° misalignment with the wind direction for high wind speeds. The tilt angle causes external moments from wind and

torque projection onto the yaw bearing leading to the misalignment. A larger cone angle can be used to decrease the misalignment with the wind direction and also to increase the dynamic stability of the equilibrium yaw position. Flapwise blade flexibility can destabilize the equilibrium yaw position, as the steady-state blade deflection at high wind speeds counteracts the cone angle.
Conclusively, the rotor for the upwind configuration and the downwind configuration are redesigned with a combination of a low fidelity optimization tool and the HAWTOpt2 framework. Turbine costs are scaled based on blade and tower masses as well as loads resulting from full load basis simulations with HAWC2. As a consequence of the load difference observed previously, the resulting rotor mass for the downwind configuration is 4.4% lower while the tower mass is 8.6% higher than for the downwind configuration. Both configurations show very similar capital expenditures, but due to the lower annual energy production of the downwind configuration, the cost of energy for the upwind configuration is 1% lower than for the downwind configuration.

Dansk sammenfatning

Denne afhandling sammenligner fordele og ulemper for vindmøller bygget efter to forskellige koncepter: bagløbere (downwind) versus mere traditionelle forløbere (upwind). Der tages udgangspunkt i en kommerciel tilgængelig Suzlon S-111 vindmølle (en forløber med 2.1 MW ydelse), der konverteres til en bagløber konfiguration ved at placere rotoren nedstrøms for mølletårnet. Den lastmæssige effekt af denne konvertering til en bagløber undersøges. Analyse af dynamisk stabilitet foretages med henblik på at afklare forskelle i dæmpning af specielt kantvise egensvingninger samt potentialet for at eliminere brugen af et aktivt krøjesystem for bagløbere. Endelig er der foretaget et omdesign af rotoren for både for- og bagløber for at evaluere forskelle i rotorvægt og -omkostning mellem disse to konfigurationer. Det overordnede mål med afhandlingen er, at evaluere mulige besparelser forbundet med en bagløber vindmølle baseret på det specifikke eksempel.

En sammenligning af det fulde lastgrundlag, beregnet med HAWC2 i henhold til IEC design standarden, viser, at den minimale frigang mellem vingespids og tårn kan øges ved konvertering af vindmøllen til en bagløber. I denne konfiguration opnås ydermere en 10 % reduktion af det ekstreme flapvise vingemoment med baggrund i den omvendte kegleform af møllens rotor. Ulempen er et relativt tab af årlig energiproduktion på 0,75 % og en 14% forøgelse af det ekstreme bøjningsmoment i mølletårnet, hvilket skyldes en ensretning af belastningerne på rotor og møllehus betinget af trykforskelle (thrust) og tyngdekraft. Endelig øges udmattelseslaster på vinger grundet den nedstrøms skyggeeffekt fra tårnet og grundet mindre aeroelastisk dæmpning i den kantvise retning.

Netop de komplekse ændringer i kantvise egensvingninger, for en bagløber i forhold til den konventionelle forløber, er blevet studeret i detaljer. Konklusionen er, at konverteringen fra for-til bagløber ændrer samspillet mellem de aerodynamiske kræfter, rotoren og tårnets torsionsbevægelse. Effekten er ændringer i de komponenter af de kantvise svingninger, der falder ud af rotorplanet, hvilket er

hovedbidragsyder til den reducerede dæmpning. Forskellige design parametre for vindmøllen, såsom rotorens keglevinkel (cone angle) og tårnets torsionsstivhed kan bruges til at øge den kantvise dæmpning.
Dernæst undersøgtes en passivt krøjende mølle-konfiguration, hvilket potentielt ville kunne forsimple møllens krøjesystem betydeligt. Det viser sig dog at møllen for høje vindhastigheder kan opnå krøjepositioner, der afviger mere end 19° fra vindretningen. Denne afvigelse skyldes en forandret moment-ligevægt for krøjesystemet, der opstår baseret på kraft-projektioner relateret til rotorens tilt. En rotor med større keglevinkel (cone angle) kan bruges til at formindske den systematiske afvigelse mellem møllens og vindens retning samtidig med at den dynamiske stabilitet af ligevægtspositionen forbedres. Øget flapvis fleksibilitet af vingerne vil derimod have den modsatte effekt, det vil sige en yderligere forskubbelse af ligevægten ved høje vindhastigheder.
Endelig er både den oprindelige rotorkonfiguration (forløber) og den tilsvarende bagløber konfiguration redesignet med en kombination af et optimeringsværktøj og HAWTOpt2. Til dette formål anvendes en forsimplet kostmodel, der skalerer omkostningen på hele vindmøllen baseret på vægt af vinge og tårn samt visse nøglelaster, der er bestemt udfra simulering af et fuldt lastgrundlag vha. HAWC2. Grundet de observerede forskelle i laster kan en bagløber-mølle designes med en 4,4 % lavere rotorvægt, mens tårnet bliver 8,6 % tungere end for forløber konfigurationen. Begge koncepter har sammenlignelige totale omkostninger, men på grund af den mindre årlige energiproduktion er produktionsprisen for energi med bagløberen 1% højere end for den konventionelle mølle (forøberen).

Preface

This thesis is submitted in partial fulfillment of the requirements for acquiring the *Doctor of Philosophy* at the Technical University of Denmark. The work is performed in the department of Wind Energy in the period December 2016 to December 2019.

The thesis deals with the investigation of design opportunities and challenges when changing an existing upwind wind turbine into a downwind concept. The work investigates the implication on wind turbine loads, the passive rotor alignment with the wind direction, as well as the tower shadow effect and turbine cost associated with the change of concept. The presentation of the different aspects are either embedded as a journal paper written within this project or are summaries of previously unpublished work. The thesis is split into two parts, a general part with an introduction to the topic, a summary and conclusion and a second part with chapters regarding the different aspects of downwind turbines in detail.

The study has been performed as an industrial PhD-project in cooperation with the Technical University of Denmark as well as Suzlon Blade Science Center. The research has been supported by the Innovation Fund Denmark (grant number 5189-00180B).

Gesine Wanke, Vejle, 14-December-2019

Acknowledgments

I would like to thank my supervisor team who has greatly supported this work: Their support, help and, guidance have been greatly appreciated. From the team I would like to thank Thomas Buhl and Jens I. Madsen for supporting the project within Suzlon with great dedication to scientific research, allowing the freedom to shape the project. I want to thank Morten H. Hansen for the always truly honest discussion of results, as well as motivating supervision. I appreciate the contribution with experience in the downwind turbine design of Torben J. Larsen and David R. Verelst. I am also grateful for the support of the rotor design task by Frederik Zahle. I want to especially thank my colleague Leonardo Bergami, for his support and his guidance throughout the project. His help and expertise have been very much appreciated.
My gratitude goes also to my family and friends for being understanding and supportive through the years, especially my boyfriend, Amin Ghadirian for his love, support, and trust in me, when I needed it the most.

Contents

Part I

Chapter 1

Introduction

With a growing world population, the demand for energy is constantly increasing. Supplying industrial plants, houses or transport systems with electricity is therefore a growing task. Figure 1.1 shows the electrical energy capacity of the OECD countries. The largest source of electricity for the OECD states are the

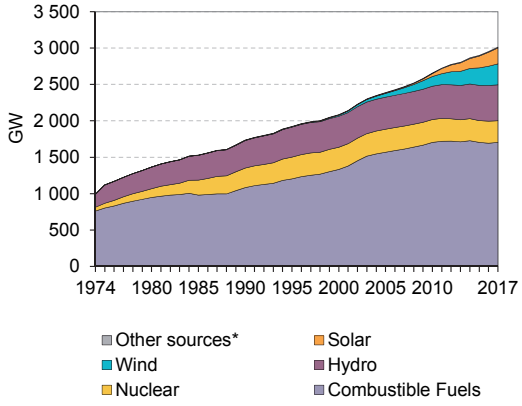

Figure 1.1: OECD net electrical capacity by source (source: International energy agency (2019))

combustible fuels (oil and gas). While nuclear power became a common source of electricity in the late 1980s wind power did not have a significant share of the electrical capacity before mid-2000s in the OECD states.
The first wind turbines were built already in the 1970s as there were many opponents of nuclear power among the population of many countries, searching for alternative energy sources. High costs for heating and electricity as well as the movement against nuclear power inspired for example a group of teachers and students of the Tvind school to build the "Tvindkraft" turbine in 1975. Tvindkraft (2019). As most of the turbines of that time, it was constructed as a

Figure 1.2: Pioneer wind turbine in Tvind (Denmark) (source: Tvindkraft (2019))

downwind turbine, placing the rotor behind the tower relative to the incoming wind. This was considered the safest configuration under operation, as the blades would not hit the tower when deforming under the loading from the wind. The support and cooperation with research institutes such as the Technical University of Stuttgart (Germany) or Danmarks Tekniske Højskole (today Denmark's Technical University) led to a successfully constructed turbine, which is still operating today. Constructed to supply a full school with electricity the turbine was untypically large for that time with a rotor diameter of 54m and a 53m tower height. Figure 1.3 shows that the typical rotor sizes of the 1980s were around 17m for machines of around 75kW. As many downwind turbines the "Tvindkraft" turbine was found to be very noisy which was one of the reasons to reduce the name plate power from 2MW to 900kW.
The noise from wind turbines in downwind configurations was found to be a general problem. Residents close to the DOE/NASA MOD-1 2000kW experimental wind turbine reported "thumping" impulse noise, causing annoyance, especially when occurring during the night. Research by Metzger and Klatte (1981) concluded that the turbine emitted low-frequency noise that was above an acceptable

limit. Upwind configurations on the other hand, where the rotor is placed in front of the tower were found to be significantly less noisy by Greene (1981). Upwind turbines became, therefore, the dominant turbine configuration in industrial applications in the 1990s.

With research and innovation, the rotor size was increased over the years, as

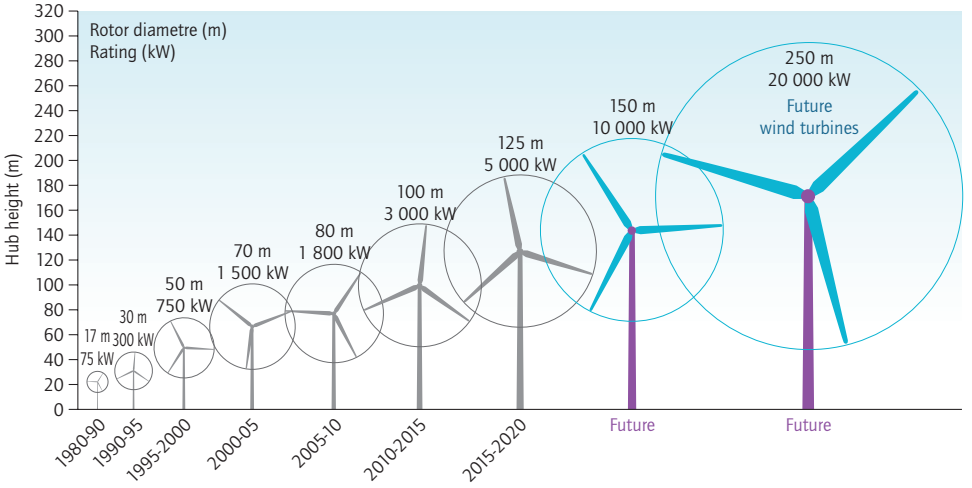

Figure 1.3: Groth in size of wind turbines since 1980 and prospects (source: International energy agency (2013))

shown in Fig. 1.3. Larger rotors were found to be more cost-efficient as more energy can be captured from a larger swept rotor area. To decrease the rotor mass and the levelized cost of energy (LCOE) rotor blades are nowadays built as light and flexible as possible. However, with the increase in rotor diameter the flexibility of the blades has to be constrained to avoid collision with the tower. Tower strikes could be fatal and lead to total turbine failure. The downwind concept does, therefore, re-experience an increase in research interest: As the blades under operation deflect away from the tower, blades for downwind rotors could potentially be designed without the tower clearance constraint on the blade deflection. As large future turbines rotate much slower than turbines in the 1980s and the airfoil design for wind turbines has advanced the noise emission could be expected to be significantly lower. The downwind concept might be a cost-efficient solution for future, extremely large wind turbines as predicted in Fig. 1.3.

Work at the Norwegian University of Science and Technology (NTNU) by Reiso (2013) for example investigated in detail the tower shadow effect on modern sized

downwind turbines. Their work showed that very flexible blades could overcome the increased fatigue load that would be expected from the blade response to the velocity deficit behind the tower.
At the Laboratory of Energy Conversion at ETH Zürich the advantages of downwind configurations were investigated, in cooperation with the Japanese manufacturer Hitachi. Their work investigated several aspects for downwind turbines, such as cone and tilt design or yaw stability (e.g. Kress et al. (2016a), Kress et al. (2015)). From their measurement in a water tunnel with a scaled model of a Hitachi turbine they concluded, that downwind turbines are advantageous in complex terrain as the alignment of tilt and flow inclination angle leads to higher power output (Kress et al. (2016b)).
Research efforts in the US regarded in further detail the cost advantages of downwind turbines compared to conventional upwind turbines. Ning and Petch (2016) evaluated the cost of energy of different turbine sizes and different wind classes within an optimization framework. Their design work is done under quasi-steady analysis. While the group showed that generally lower blade mass is achievable in a downwind configuration, the downwind configurations are also shown to generally come with higher tower mass as the gravity moment from the rotor nacelle assembly at the tower foundation is aligned with the moment from the thrust. Due to the associated tower cost the wind class III (low wind speeds) showed the largest design potential for downwind turbines.
Inspired by palm trees deflecting under extreme winds during storms Ichter et al. (2016) investigated a 2-bladed "morphing downwind-aligned rotor" where a joint at the hub could be unlocked for operation above rated power to allow the blades to align with the forces in the wind field. Due to a massive reduction in bending loads peak stresses in the blade material could be reduced, indicating a potential rotor mass saving.
In a parallel study Loth et al. (2017) proposed a downwind pre-aligned rotor concept without morphing. Aligning the cone angle and blade curvature (prebend) with the forces from gravity, aerodynamics and centrifugal force results into a reduction of maximum bending stresses. The study indicated a potential mass saving of 25 % compared to a conventional upwind turbine.
High extreme wind speeds in typhoon areas could make the downwind concept attractive for markets in Asia. Hosted by Japan, the "IEA-task 40: downwind technologies" is aiming to combine research efforts of research institutes and manufacturers (iea wind (international energy agency wind)). The Japanese manufacturer Hitachi commercialized a 2.0MW and a 5.2MW 3-bladed downwind concept (Kiyoki et al. (2016), Hitatchi (2019)) and the Chinese manufacturer Ming Yang has tested a 6.5MW 2-bladed downwind prototype (Smith (2014)).
A more radical approach is chosen by the Spanish start-up X1wind. Instead of a conventional tower, the rotor nacelle assembly is hanging underneath a floating

pyramid lattice structure, as shown in Figure 1.4. Compared to conventional

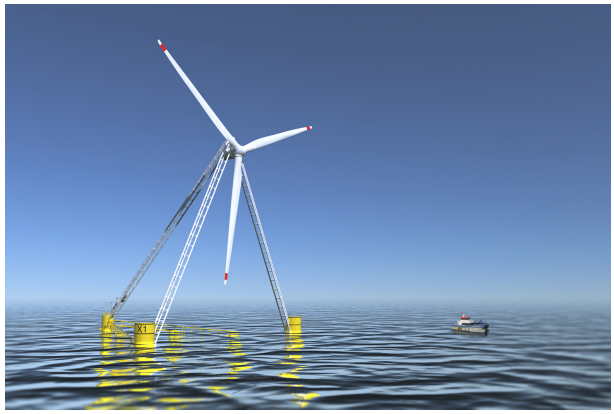

Figure 1.4: Innovative passive yawing downwind turbine concept on a floating single point mooring system called PivotBuoy® (source: x1wind (2019)).

floating wind turbine X1wind estimates a cost reduction of 50% and a mass saving of around 80% with their innovative downwind concept. To prove the concept a prototype will be installed at a test site at the Oceanic Platform of the Canary Islands in 2020.

1.1 Motivation and thesis outline

This project is investigating the potential cost savings that could be achieved if the Suzlon S111 2.1MW turbine had been designed as a downwind configuration. The example turbine is a pitch regulated class IIIA turbine with an asynchronous induction variable speed generator. The turbine has a rotor diameter of 111.8m and a tubular tower of 90m height (see also Sulzon (2019)). It is expected that the blade deflection constraint can be relaxed, and therefore rotor mass could be saved when converting the example turbine from the upwind rotor configuration into a downwind configuration. The impact of such configuration change is investigated within the thesis.
The research has been focused on several aspects of the downwind turbine concept. The results are documented in this thesis as a collection of accepted papers, submitted manuscripts and additionally written chapters.

In the initial investigations, the upwind configuration has been converted into a downwind configuration by realigning the different turbine components. A full load assessment is made and the loads are compared between the upwind and the downwind configuration. Chapter 4 includes the article "Changes in design driving load cases: Operating an upwind turbine with a downwind rotor configuration" published in the Journal of Wind Energy by Whiley and Sons.
Chapter 5 investigates the reduction in edgewise damping when the upwind configuration is changed into the downwind configuration causing high extreme and fatigue loads. "Differences in damping of edgewise whirl modes operating an upwind turbine in a downwind configuration" is a manuscript under discussion in the Journal of Wind Energy Science.
The major disadvantage of downwind configurations, the tower shadow effect, is regarded in more detail in the additionally written chapter 6. Literature has been reviewed to elaborate on the tower shadow effect and possible mitigation techniques for the example turbine in the downwind configuration.
One of the often stated advantages of the downwind configuration is that the rotor could passively align with the wind direction. Chapter 7 regards the passive alignment with the wind direction and the dynamic yaw stability in the article "Qualitative yaw stability analysis of free-yawing downwind turbines" published in the Journal of Wind Energy Science.
The additionally written chapter 8 regards additions, made to the controller to eliminate certain load cases from the design driving situations. With these additions the design process using an optimization tool could be simplified.
In the last chapter a rotor is redesigned for both configurations and possible mass and cost reductions for the Suzlon S111 class III 2.1MW turbine, associated with the redesigns are estimated. Chapter 9 is the manuscript "Estimated mass and cost savings converting an upwind wind turbine into a downwind rotor concept." submitted to the Journal of Wind Energy Science.

Bibliography

Greene, G. C. (1981). Measured and calculated characteristics of wind turbine noise. *NASA Report*, CP-2185.

Hitatchi (2019). Hitatchi 5200kw wind turbine, htw5.2-127, htw5.2-136. *Product catalogue*. url: http: //www.hitachi.com /products /energy /wind /Catalog / __icsFiles /afieldfile /2018 /01 /31 /HTW5.2 _EG-E109.pdf; Date of Access: 2019-09-30.

Ichter, B., Steele, A., Loth, E., Moriarty, P., and Selig, M. (2016). A morphing downwind-aligned rotor concept based on a 13-mw wind turbine. *Wind Energy*, 19:625–637. https://doi.org/10.1002/we.1855.

iea wind (international energy agency wind) (2019). Task 40: downwind turbine technologies. url: https://community.ieawind.org/task40/home; Date of Access: 2019-10-03.

International energy agency (2013). Technology roadmap wind energy (2013 edition). *energy technology perspectives*, page 27.

International energy agency (2019). electricity information: overview (2019 edition). *iea statistics*, page 6.

Kiyoki, S., Sakamoto, K., Inamura, S., Tobinaga, I., Saeki, M., and Yokoyama, K. (2016). Development of 5-mw downwind turbine and floating substation facility for offshore wind power. *Hitatichi Review*, 65(4):938–943. http://www.hitachi.com/rev/pdf/2016/r2016_04_all.pdf. Accessed: April 26, 2018.

Kress, C., Chokani, N., and Abhari, R. (2015). Downwind wind turbine yaw stability and performance. *Renewable Energy; Vol. 83; p. 1157-1165.* https://doi.org/10.1016/j.renene.2015.05.040.

Kress, C., Chokani, N., and Abhari, R. (2016a). Passive minimization of load fluctuations on downwind turbines. *Renewable Energy*, 89:543–551–147. https://doi.org/10.1016/j.renene.2015.12.009.

Kress, C., Chokani, N., Abhari, R., Hashimoto, T., Watanabe, M., Sano, T., and Saeki, M. (2016b). Impact of flow inclination on downwind turbine loads and power. *Journal of Physics: Conference Series 753: The Science of Making Troque from Wind (TORQUE2016).* https://doi.org/10.1088/1742-6596/753/2/022011.

Loth, E., Steele, A., Qin, C., Ichter, B., Selig, M. S., and Moriarty, P. (2017). Downwind pre-aligned rotors for extreme-scale wind turbines. *Wind Energy*, 20:1241–1259. https://doi.org/10.1002/we.2092.

Metzger, F. and Klatte, R. (1981). Status report on downwind horizontal axis wind turbine noise prediction. *NASA Report*, N82-23684 14-44:425–430.

Ning, A. and Petch, D. (2016). Integrated design of downwind land-based wind turbines using analytic gradients. *Wind Energy*, 19:2137–2152. https://doi.org/10.1002/we.1972.

Reiso, M. (2013). The tower shadow effect in downwind turbines. *Thesis for degree of Philosophiae Doctor, Norwegian University of Science and Technology.*

Smith, P. (2014). Ming yang installs 6.5mw prototype. *Wind power offshore.* https//www.windpoweroffshore.com /article/1320170 /ming-yang-installs-65mw-prototype; Date of Access: 2019-10-02.

Sulzon (2019). S111 2.1mw platform doing more with less. *Product catalogue.* url: https://www.suzlon.com /pdf /S111_product _brochure _Feb _2019.pdf; Date of Access: 2019-10-02.

Tvindkraft (2019). Tvindkraft. url: https://www.tvindkraft.dk/en /; Date of Access: 2019-10-02.

x1wind (2019). x1wind redesigning offshore wind. url: https://www.x1wind.com /; Date of Access: 2019-11-21.

Chapter 2

Summary

This synopsis gives an overview of the investigations done within the project and the main results. The investigations started out with load investigations to understand the difference between the two turbine concepts. Due to the observed high edgewise loads the difference of edgewise damping was investigated in more detail. The tower shadow effect of downwind turbines has been studied in literature to reflect on its impact on fatigue loads and low-frequency noise, as the tower wake is only partly resolved in the aeroelastic simulations. Downwind turbines are often associated with a passive yaw alignment. Therefore, one part of the project focuses on the ability of the turbine to align passively with the wind direction and the dynamic stability of a free yawing turbine configuration. To reflect an industrial control set-up, that aims for a turbine design driven by normal operation, modifications are made to the used academic controller and the impact on loads and energy production is shown for both turbine configurations. Finally, the rotor is redesigned with an optimization routine for the turbine in upwind and in downwind configuration to compare achievable mass and cost savings between the configurations.
The study is based on the Suzlon S111 turbine which is used as an upwind baseline. The turbine characteristics are shown in Table 2.1.

Table 2.1: Turbine characteristics of the Suzlon S111 upwind baseline (see also Sulzon (2019))

Turbine data	value
wind class	IIIA
rotor diameter	111.8m
tower height	90m
rated power	2.1MW
cut-in wind speed	3m/s
rated wind speed	9.5m/s
cut-out wind speed	21m/s
regulation	pitch regulated
generator type	asynchronous induction variable speed

2.1 Changes in design driving load cases: Operating an upwind turbine with a downwind rotor configuration

Investigating the response of a wind turbine structure to the applied loads during its lifetime is crucial when it comes to turbine design. The extreme and fatigue loads set the limits of the structural design of the turbine and therefore drive the material costs. The differences in loads between the upwind and the downwind configuration have to be understood to be able to choose an appropriate design strategy for a downwind turbine. In this project, a full design load basis for the downwind configuration is compared to the upwind configuration. The published article for this topic can be found in Chapter 4.
In the investigations of this paper, the upwind baseline turbine is reassembled in a downwind configuration. In the downwind configuration the turbine tilt and cone angle increase the blade tip to tower distance (tower clearance). As the original prebent is towards the blade pressure side it decreases the tower clearance in the downwind configuration. As the latter is not a realistic design configuration a second downwind configuration without prebend is investigated. For all three configurations, a full design load basis is calculated according to the IEC-standard (IEC (2014)). The aeroelastic simulations are done with HAWC2 (Madsen et al. (2019)) applying the DTU-control set-up (Hansen and Henriksen (2013)). From the design load basis, the design driving loads are identified. Additionally, the annual energy production (AEP) is calculated from simulations at normal operation without inclination angle or yaw error. These simulations are also used to investigate the difference in 10-minute mean loads for the different

configurations. To quantify the effect of the tower shadow the downwind configurations are additionally simulated with the tower shadow model of the upwind configuration.
The analysis shows, that the tower clearance is increased when the upwind configuration is changed into the downwind configurations. Figure 2.1 shows the tower clearance of all three investigated configurations normalized with the unloaded blade tip to tower clearance of the upwind configuration. It can be seen, that

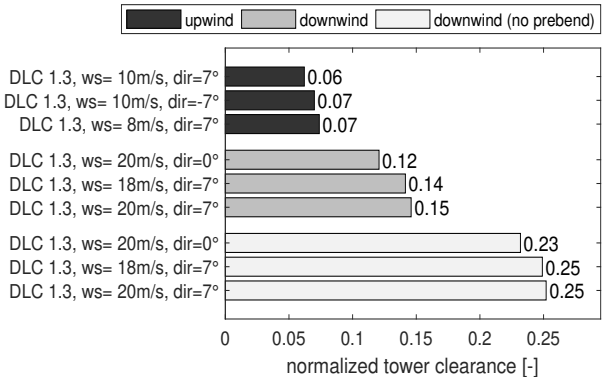

Figure 2.1: Normalized tower clearance compared between the upwind, the downwind and the downwind configuration without prebend from the load cases with the three lowest values. The values are normalized with the unloaded blade tip to tower distance of the upwind configuration. Design load case: DLC 1.3: power production in extreme turbulence.

the design driving situation for the tower clearance is the operation at extreme turbulence. For the upwind configuration, the operation at the thrust peak leads to the minimum tower clearance. The operation at high wind speeds is on the other hand design driving for downwind configurations. Since the operation at high pitch angles can lead to negative lift values at the outboard part of the blade the blades deflect towards the tower. The prebend changes the blade tip to tower distance for the same blade deflection in the two downwind configurations.
Coning in the downwind direction results into a different loading of the blade than in the upwind direction. Coning downwind aligns the blade lengthwise direction with the force resulting out of the thrust, the gravity and the centrifugal force. Compared to the upwind configuration the downwind configurations are subject to lower flapwise bending moments, but higher tension loads. This has also been shown by Loth et al. (2017), Ichter et al. (2016) and Zalkind et al. (2019). Figure 2.2 shows the 10-minute mean value of the flapwise blade root

moment normalized with the maximum value of the upwind configuration. This

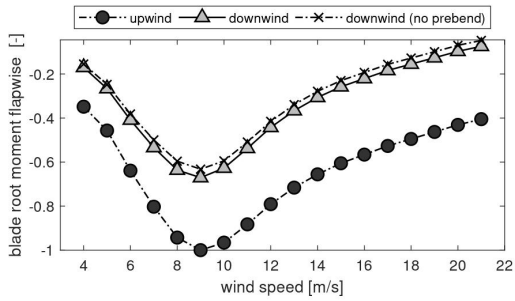

Figure 2.2: Comparison of flapwise blade root bending moments between the upwind, downwind and the downwind configuration without prebend. Comparison of the normalized 10-minute mean flapwise blade root bending moments over wind speed.

significant reduction in flapwise bending load is probably the major advantage of the downwind configuration and significant mass changes can be expected on the rotor when it comes to design.
With the downwind configuration several challenges arise. Firstly, the alignment of the gravity overhanging moment of the rotor nacelle assembly coincides with the thrust in the downwind configuration. As also shown by other researches, this effect increases the tower loads significantly (e.g. Ning and Petch (2016))
Also, the increase of fatigue loads, especially for the flapwise blade root bending moment and the main bearing tilt moment is expected, due to the tower shadow in the downwind configurations (e.g. Zahle et al. (2009a)or Reiso (2013)). Less expected is the observed increase in the edgewise blade root extreme and fatigue loads. Figure 2.3 shows the design driving extreme loads cases for the edgewise blade root bending moment normalized with the highest value of the upwind configuration. It can be seen that the increase in edgewise loads can be significant, especially for a downwind configuration without prebend. The increase in edgewise extreme and fatigue loads could be associated with a decrease in damping when the upwind configuration is changed into the downwind configuration.
In agreement with the work of Zalkind et al. (2019), the AEP of the downwind configurations is lower than the AEP of the upwind configuration. Due to the coning direction, the area decrease associated with blade deflection and the tower shadow the AEP is 1.97% lower in the downwind configuration and 2.78% lower in the downwind configuration without prebend.

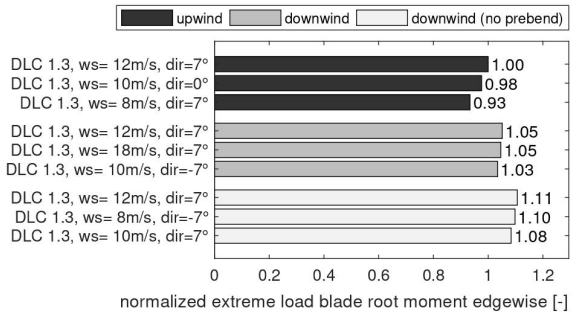

Figure 2.3: Comparison of edgewise blade root bending moments between the upwind, downwind and the downwind configuration without prebend. Comparison of the highest three edgewise blade root bending moments normalized with the highest value of the downwind configuration. Design load case is: DLC 1.3 power production in extreme turbulence.

2.2 Difference in damping of edgewise whirl modes: operating an upwind turbine with a downwind rotor configuration

The observed decrease in damping when the upwind configuration is changed into a downwind configuration could decrease the design potential of the downwind configurations. High edgewise loads could require high blade masses, eliminating potential material savings. The decrease in damping and the design parameter influencing the edgewise damping are therefore investigated. The submitted manuscript for the investigations can be found in chapter 5.
The edgewise damping is calculated from timeseries of aeroelastic simulations. The geometry and the wind field are simplified and gravity is neglected to be able to calculate the damping ratio from peak to peak counting. The damping is calculated for the upwind and the downwind configuration with all degrees of freedom (fully flexible, FF). The main contributors to the difference in edgewise damping are identified by increasing the stiffness of several components. Further investigations are subsequently made on configurations with a flexible rotor and tower torsion (RTT). The RTT configurations are used for further investigations regarding the mode shapes, as well as parameter variations of shaft length, cone angle and tower torsional stiffness. For both configurations, the investigated cone angle increases the tower clearance.

The interaction of the aerodynamic forces with the rotor and the tower torsion could be identified as the main contributor to the difference in edgewise damping. Figure 2.4 shows the calculated damping for the upwind and the downwind configurations at the top for the backward whirling mode (a) and the foreward whirling mode (b) of the upwind and the downwind configurations. It can be seen

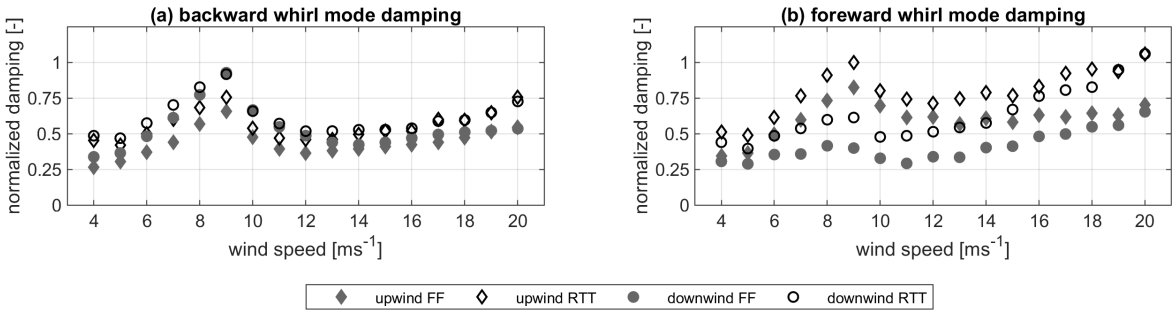

Figure 2.4: Normalized damping ratio as function of wind speed for the back whirl mode (a) and the foreward whirl mode (b) for the upwind RTT and the downwind RTT configuration and the fully flexible FF configurations. The damping is normalized with the damping of the upwind RTT configuration at 9 ms^{-1} of the foreward whirl mode.

from the figure, that the change of configuration increases the edgewise damping in the backward whirl mode while it decreases the edgewise damping in the foreward whirl mode. Compared to the upwind configuration the downwind configuration has a higher damped backward whirl mode than foreward whirl mode. The reason is that the backward whirl mode of the downwind configuration has a higher out-of-plane component of the edgewise whirl mode. Figure 2.5 shows the modal out-of-plane displacements at $9ms^{-1}$ for both modes and both turbine RTT configurations in multi-blade coordinates. Due to the phasing of the rotor motion and the tower torsional motion, the summed sine out-of-plane motion in the foreward whirl mode is decreased and the damping reduced for the downwind configuration. It has further been concluded that the difference in forcing due to the configuration gives a difference in the modal phases. The modal phases do consequently result in a difference in damping.
The effect can be amplified with the increase in shaft length. The cone angle on the other hand dominantly changes the cosine out-of-plane displacements of the modes. Mapping the edgewise damping over wind speed shows that upwind

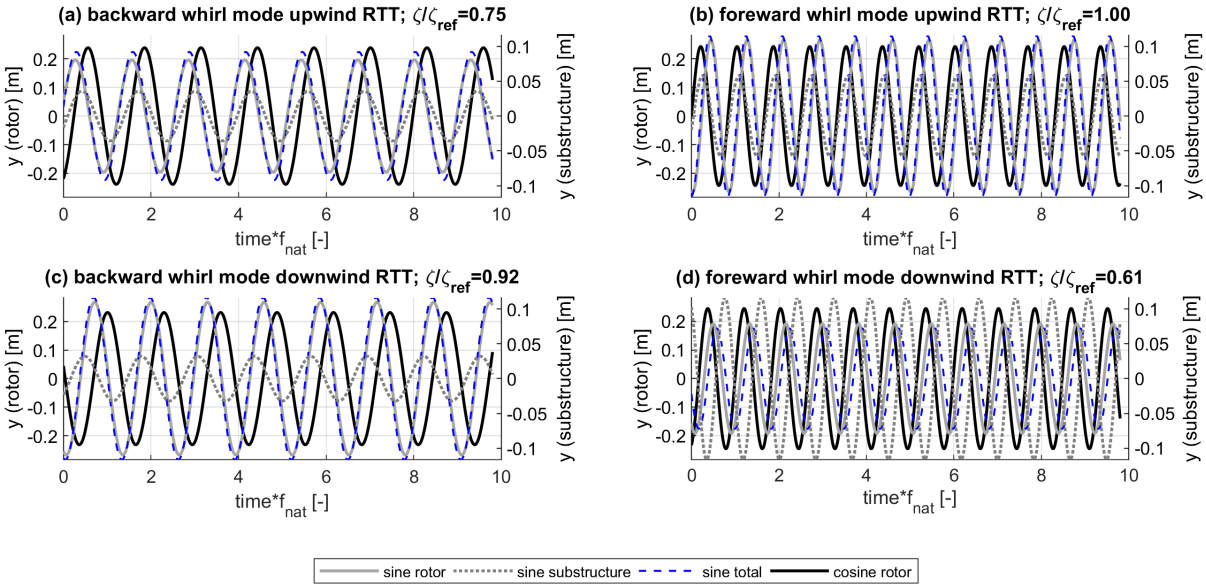

Figure 2.5: Modal out-of-plane displacements at the rotor position at r/R=75% at 9ms^{-1} for the backward whirl mode ((a), (c)) and foreward whirl mode ((b), (d)) of the upwind RTT ((a), (b)) and downwind RTT configuration ((c), (d)). The time axis is normalized with the blade edgewise natural frequency.

configuration benefits from large cone angles, while the downwind configuration benefits from a decrease in cone angles. A significant decrease in tower torsional stiffness, e.g. a lattice tower configuration is shown to be an opportunity for the downwind configuration to increase the edgewise damping in both edgewise modes.

2.3 Review of tower shadow effect and the implications on loads and noise

The tower shadow has been shown to increase the fatigue loads in the downwind configuration. The tower shadow is also known to increase the noise level of

downwind configurations. Chapter 6 reviews the tower shadow effect and reflects on the modeling approach used throughout the current study.
In the aeroelastic code HAWC2, the downwind tower shadow model is a pure velocity deficit model. The expected increase in turbulence behind the tower is neglected. From literature review it can be concluded, that this is not sufficient (e.g. Zahle et al. (2009b) or Reiso (2013)). Fatigue and also extreme loads are under-predicted as the increased turbulence intensity is neglected and the blade vortex interaction is not captured.
From the literature review also a significant increase in the low-frequency noise level can be expected, when the upwind configuration is changed into a downwind configuration (Madsen (2011)). Noise calculations have to be made for the downwind configuration to assure that the emitted noise level especially close to residential areas is within the permitted range.
Measures would need to be taken to alleviate the tower shadow effect for noise and load reduction. The most efficient, but also most costly, complicated and maintenance intense would be an airfoil-shaped fairing on the tower aligning with the wind direction. Literature shows that the tower shadow effect could be eliminated (e.g. Wilmshurst et al. (1985) or Reiso and Muskulus (2013)). However, a negative effect of the fairings has been stated in case of misalignment with the wind direction (Noyes et al. (2018)) Also incidents of the blades colliding with the fairing during field measurements have been reported by Wilmshurst et al. (1985).
Less efficient but cheaper alleviation techniques could aim to destroy coherent vortex structures behind the tower. Such devices could be vortex generators or helix wires on the tower surface. Independent of the alleviation technique chosen, further investigations should be made, quantifying the effect on turbine loads and noise level.

2.4 Qualitative yaw stability analysis of free-yawing downwind turbines

Downwind turbines could potentially be designed to align passively with the wind direction (e.g. Corrigan and Viterna (1982) or Verelst and Larsen (2010)) . Realizing a free yawing downwind option might be economically attractive: yaw drives could be smaller as their functionality could be reduced to cable unwinding. The yaw system could be reduced in complexity and maintenance cost could be reduced. The article in chapter 7 investigates the equilibrium yaw angle of a free-yawing downwind configuration and the dynamic stability of the equilibrium

position.
The study of the free yawing downwind turbine is split into two parts. For the investigations of the equilibrium yaw position a Blade-Element-Momentum (BEM)-code, including a skewed wake model is used. From the BEM-code the yaw position for a zero-yaw moment is found from the interpolation between the calculations at different yaw positions. The method is validated against the free yaw position simulated with HAWC2 and used for parameter investigations of tilt angle, cone angle and shaft length. In the second part, a two-degree-of-freedom (2DOF) model is set-up including the free yaw and the tower side-side motion. The stability of the yaw alignment is investigated from an eigenanalysis and validated against HAWCStab2. The 2DOF model is used for parameter investigations of cone angle and shaft length. Finally, HAWCStab2 (Hansen (2004)) is used to extend the 2DOF model to the full turbine flexibility.
The equilibrium yaw position of a tilted and coned downwind rotor shows high yaw misalignments with the wind direction for high wind speeds, as displayed in Fig. 2.6. Two external moments due to the tilt angle have to be balanced by

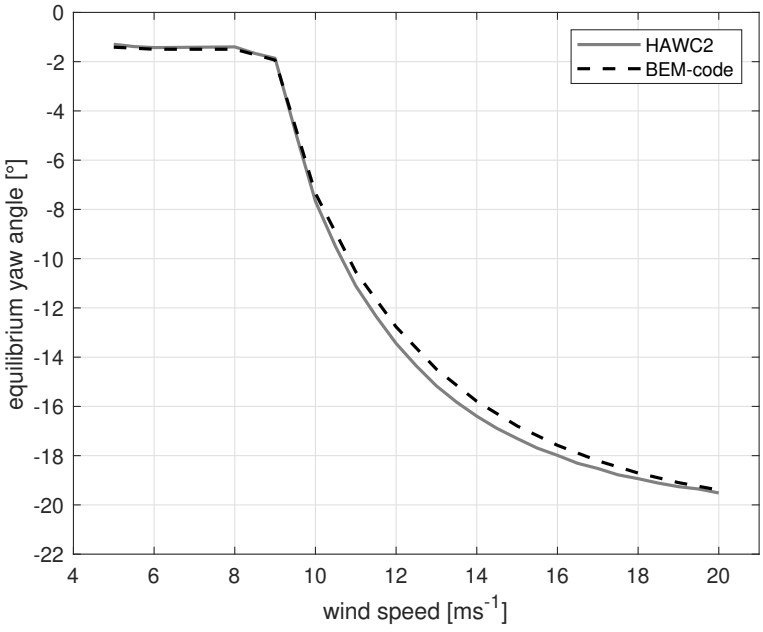

Figure 2.6: Comparison of the equilibrium yaw angle over wind speed from HAWC2 and the BEM-code for the original turbine configuration with 5° tilt and 3.5° cone.

the restoring moment due to aerodynamic stiffness. The first is the projection of the torque onto the yaw bearing with the sine of the tilt angle. The second external moment is a projection of the wind speed onto the rotor plane causing a difference in angle of attack when the blade is moving upwards compared to moving downwards. These external moments have to be balanced by the aerodynamic stiffness generated from the induction imbalance on the yawed rotor, the wind speed projection on the yawed rotor and the wind speed projection due to a combination of yaw and cone angle. The total external moment increases with the wind speed. As the induction, on the other hand, decreases with increasing wind speed large yaw angles are required to create more stiffness from wind speed projections. Large tilt angles increase the equilibrium yaw positions. Large cone angles, on the other hand, decrease the equilibrium yaw positions as they increase the aerodynamic stiffness.
Large cone angles can also be used to achieve a dynamically stable equilibrium yaw position on a rotor without tilt angle. The analysis of the 2DOF model shows that this is again an effect of increased aerodynamic stiffness rather than an increase in aerodynamic damping. Extending the 2DOF model shows that at least the blade flapwise flexibility has to be included to predict the wind speed limit for the dynamic stability of the yaw equilibrium correctly, as it can be seen in Figure 2.7. This is partly due to the blade flexibility and the associated interaction with the yaw motion. Other than that the steady-state deflection of the blade decreases the aerodynamic yaw stiffness as the blade deflects towards the tower due to a negative lift on the outboard part of the blades at high wind speeds and high pitch angles.

2.5 Control modifications for extreme turbine loads driven by normal operation load cases

The opportunities and challenges of the conversion of turbine configuration have been investigated. In chapter 8 the impact of control modifications is investigated. These modifications aim to eliminate fault cases from the design driving load cases of the turbine. This reflects a more industrial controller set-up. It has further the advantage to simplify the load assessment during turbine design, especially if optimization routines are employed. The investigated modifications aim to reduce loads of the tower, the blades and the main bearing. A full load basis is recalculated with the same set-up as previously in the project, to evaluate the impact of the changes made.

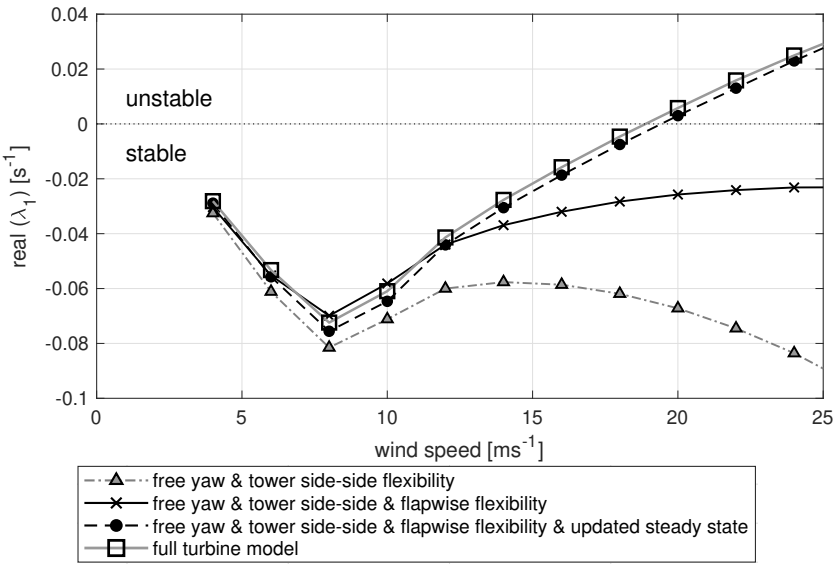

Figure 2.7: Comparison real part of the first eigenvalue of the yaw mode, for the imitation of the 2DOF model, the model containing additionally the blade flapwise flexibility, the model with the additional blade flapwise flexibility and the linearization around the deformed steady state and the full turbine model with a linearization around the deformed steady state and updated operational data from HAWCStab2.

The start-up and stopping routines need to be adjusted for the downwind configuration to avoid high tower loads. As the gravity overhanging moment of the rotor nacelle assembly coincides with the moment of the thrust, high thrust fluctuations should be avoided. Compared to an upwind configuration the pitch speed during start-up should be lower especially for the start-up at high wind speeds (DLC 3.x). Further, the pitch speed during shut-down should be faster, reducing high loads during extreme operational gusts (DLC 4.2), when the extreme loads are due to the gust rather than the shut-down procedure.
Loads due to the extreme operational gust are also targeted by a PD-controller employed additionally to the DTU-controller. The controller measures the flapwise blade root moment signal as an estimate of the thrust. The PD-controller is tuned to calculate a limited pitch offset, which aims at keeping the thrust equal to a moving average. The pitch offset is added to the pitch signal of the DTU-controller. With wind speed dependent gain scheduling, this feature can be

employed above rated wind speed only, to avoid power losses. Figure 2.8 shows the longitudinal tower bottom bending moment for the upwind and the downwind configuration with the original and the advanced control. The longitudinal tower

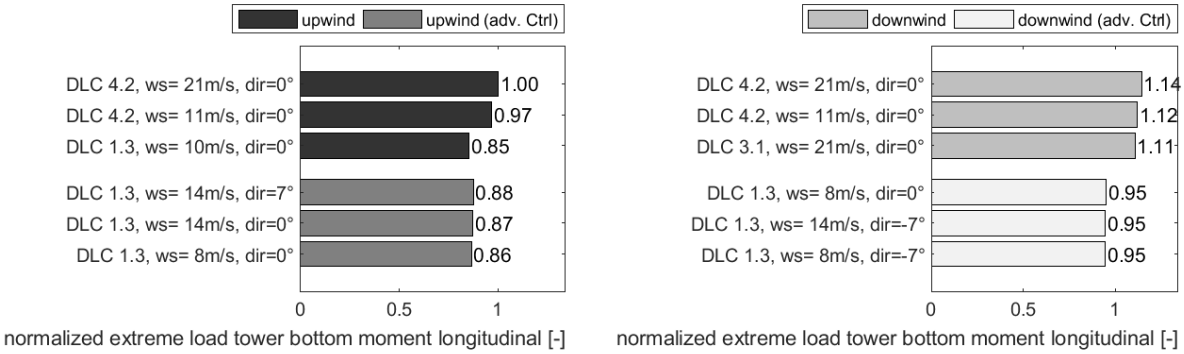

Figure 2.8: Comparison of tower bottom longitudinal bending moments between the upwind and the downwind configuration, without and with advanced control (adv. Ctrl), for the highest three bending moments, normalized with the extreme of the upwind configuration. Design driving load cases are: DLC 4.2 shut down during extreme operational gust, DLC 3.1 start-up and DLC 1.3 power production in extreme turbulence.

bottom bending moment can be significantly reduced with the control addition. The control addition also reduced the difference in tower loading between the two configurations by half. This control modification comes at the expense of a small AEP reduction for both turbine configurations. Also slight blade root torsion fatigue load increase for both turbine configurations. Exclusively in the downwind configuration, an increase of tower bending fatigue loads has been observed.
To reduce the flapwise blade root loads from the operation at extreme yaw error (DLC 2.2y), the wind direction and wind speed are supervised. If both are above a certain threshold a turbine shut-down is initiated. Figure 2.9 shows that DLC 2.2y can be eliminated from the design driving load cases and design loads can be driven by the operation at extreme turbulence for the flapwise blade root moment. In the case of the flapwise blade root moment, the difference between the two configurations increases if the design is driven by extreme turbulence.
Inspired by a commercial solution for downwind turbines by Hitachi (Hitatchi (2019)) both turbine configurations can be free yawing during gird loss. As this load case simulates wind directions from 360°, this solution is as valid for down-

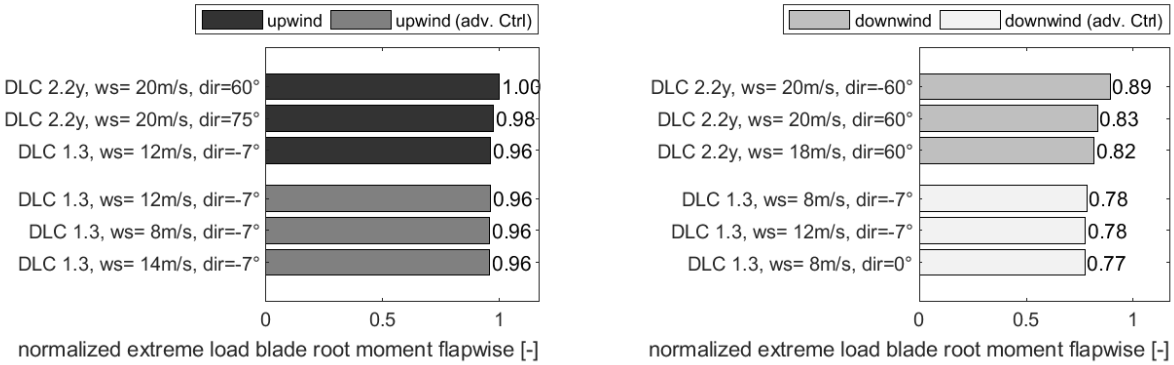

Figure 2.9: Comparison of flapwise blade root bending moments between the upwind and the downwind configuration, without and with advanced control (adv. Ctrl), for the highest three bending moments, normalized with the extreme of the upwind configuration. Design driving load cases are: DLC 2.2y power production with abnormal yaw error and DLC 1.3 power production in extreme turbulence.

wind configurations as for upwind configurations. This control addition reduces blade root torsion and tower side-side extreme loads. The latter is however still driven by stand-still loads, not by a normal operation load cases.

2.6 Re-design of an upwind rotor for a downwind configuration: design changes and cost evaluation

As a conclusion of the previous research effort, the mass and cost savings of the downwind concept in comparison to the upwind concept are evaluated in the article in chapter 9. To do a fair comparison the rotor is redesigned for the upwind and the downwind configuration. A low fidelity in-house tool is used to design the rotor. For the upwind configuration, a planform design is made. In the case of the downwind configuration, two scenarios are considered. Firstly, a structural redesign with a planform kept the same as the baseline. This scenario corresponds to a turbine conversion and a pure material saving while keeping the

blade molds. The second scenario is a full planform design comparable to the upwind design case. The resulting planform and stiffness distribution are fitted in the HAWTOpt2 framework (Zahle et al. (2016)) to generate a full HAWC2 set-up. A full design load basis and the AEP are evaluated for all the designs. The resulting loads are used to calculate the required tower mass for a tubular tower configuration. A cost model is used to evaluate the turbine cost of the designs as well as the cost of energy (COE) based on the calculated masses and the loads.

The new designs in both cases have a larger thickness over chord distribution compared to the baseline rotor blade, as high stiffness can be utilized with less material. The maximum material strain is utilized over a larger radial blade span. In contrast to the upwind design, none of the downwind designs are constrained in the blade tip to tower clearance. Among the two comparable planform designs, the downwind configuration achieves the lowest rotor weight. The required tower mass, on the other hand, is higher for the downwind configurations. Figure 2.10 shows the CAPEX of the upwind baseline S111uw, the downwind baseline S111dw, the planform designs S111uw PF and S111dw PF, as well as S111dw. The figure further shows the costs that are not affected by the redesign. The design changes impact around 2/3 of the CAPEX. Due to the reduced flapwise blade root moment of the downwind configurations savings are achieved on the rotor as well as the nacelle. These savings are offset by higher tower and foundation costs due to the increased loads discussed previously. Overall, similar CAPEX can be achieved with the two planform designs S111uw PF and S111dw PF. In the applied cost model the OPEX costs scale with the AEP, resulting in lower OPEX costs for the downwind configurations. Regarding the total COE, the upwind configuration remains 1% cheaper than the downwind configuration for the same reason.

The design work concludes overall, that the work is too limited to draw a general conclusion on the competitiveness of downwind configurations in comparison to upwind configurations. But the following conclusion could be drawn: the downwind concept can be competitive if the market would be turbine cost driven rather than COE driven. Downwind configurations are competitive if the baseline turbine has a comparably expensive rotor and cheap tower. This could be for example the case with wired towers where wires take the bending moments rather than thick tower walls. Control features for the upwind configuration such as peak-shaving could outperform the downwind configurations since they come with the same characteristics of blade loads and AEP, and a decrease in tower bending loads.

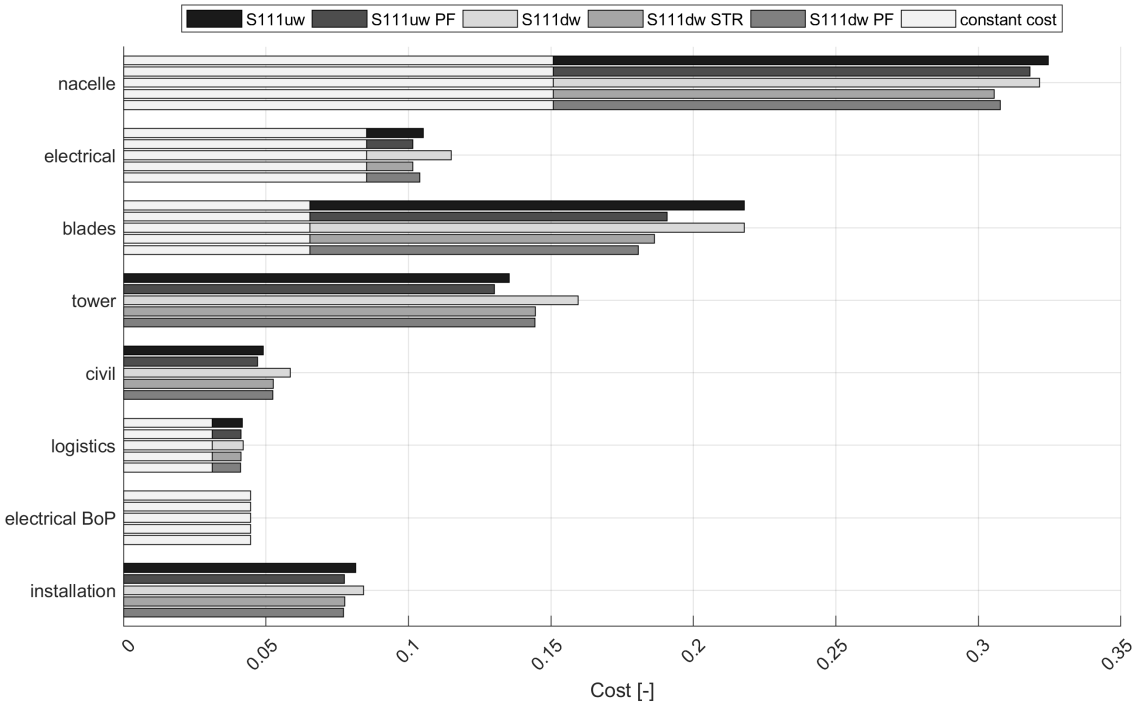

Figure 2.10: Turbine CAPEX cost split by main cost components normalized by the sum of the S111uw configuration with indication of constant costs not affected by redesign process.

Bibliography

Corrigan, R. and Viterna, L. (1982). free yaw performance of the mod-0 large horizontal axis 100kw wind turbine. *NASA-Report*, TM-83(19235):103–122.

Hansen, M. (2004). Aeroelastic stability analysis of wind turbines using an eigenvalue approach. *Wind Energy*, 7:113–143. https://doi.org/10.1002/we.116.

Hansen, M. and Henriksen, L. (2013). Basic dtu wind energy controller. *DTU-Wind-Energy-Report*, E-0028.

Hitatchi (2019). Hitatchi 5200kw wind turbine, htw5.2-127, htw5.2-136. *Product catalogue*. url: http: //www.hitachi.com /products /energy /wind /Catalog /

__icsFiles /afieldfile /2018 /01 /31 /HTW5.2 _EG-E109.pdf; Date of Access: 2019-09-30.

Ichter, B., Steele, A., Loth, E., Moriarty, P., and Selig, M. (2016). A morphing downwind-aligned rotor concept based on a 13-mw wind turbine. *Wind Energy*, 19:625–637. https://doi.org/10.1002/we.1855.

IEC (2014). Iec 61400-1 ed.3 wind turbines- part1: Design requirements. Technical report, International Electronical Commission.

Loth, E., Steele, A., Qin, C., Ichter, B., Selig, M. S., and Moriarty, P. (2017). Downwind pre-aligned rotors for extreme-scale wind turbines. *Wind Energy*, 20:1241–1259. https://doi.org/10.1002/we.2092.

Madsen, H. A. (2011). Low frequency noise from wind turbines mechanisms of generation and its modelling. *Journal of low frequency noise, vibration and active control; Vol. 29; p. 239-251.*

Madsen, H. A., Larsen, T. J., Pirrung, G. R., and Zahle, F. (2019). Implementation of the blade element momentum model on a polar grid and its aeroelastic load impact. *Wind Energy Science Discussion.* https://doi.org/10.5194/wes-2019-53, in review.

Ning, A. and Petch, D. (2016). Integrated design of downwind land-based wind turbines using analytic gradients. *Wind Energy*, 19:2137–2152. https://doi.org/10.1002/we.1972.

Noyes, C., Quin, C., Loth, E., and Schreck, S. (2018). Measurements and predictions of wind turbine tower shadow and fairing effects. *Journal of Wind Engineering and Industrial Aerodynamics*, 179:297–307. https://doi.org/10.1016/j.jweia.2018.06.012.

Reiso, M. (2013). The tower shadow effect in downwind turbines. *Thesis for degree of Philosophiae Doctor, Norwegian University of Science and Technology.*

Reiso, M. and Muskulus, M. (2013). The simultaneous effect of a fairing tower and increased blade flexibility on a downwind mounted rotor. *Journal of Renewable and Sustainable Energy*, 5(3):033106–1–1033106–11. https://doi.org/10.1063/1.4803749.

Sulzon (2019). S111 2.1mw platform doing more with less. *Product catalogue.* url: https://www.suzlon.com /pdf /S111_product _brochure _Feb _2019.pdf; Date of Access: 2019-10-02.

Verelst, D. R. and Larsen, T. J. (2010). Yaw stability of a free-yawing 3-bladed and downwind wind turbine. *EAWE PhD Seminar.*

Wilmshurst, S., Powles, S., and Wilson, D. (1985). The problem of tower shadow. *Proceedings of the Bwea Wind Energy Conference (british Wind Energy Association)*, pages 95–102.

Zahle, F., Madsen, H., and Sørensen, N. (2009a). Evaluation of tower shadow effects on various wind turbine concepts. *Research in Aeroelasticity DTU Report EFP-2007-II*, 1698:1–147.

Zahle, F., Sørensen, N., and Johansen, J. (2009b). Wind turbine rotor-tower interaction using an incompressible overset grid method. *Journal of Wind Energy*, 12:594–619. https://doi.org/10.1002/we.327.

Zahle, F., Tibalidi, C., Pavese, C., McWilliam, M. K., Blasques, J. P. A. A., and Hansen, M. H. (2016). Design of an aeroelastically tailored 10mw wind turbine rotor. *Journal of Physics: Conference Series 753; p.1-11.* https://doi.org/10.1088/1742-6596/753/6/062008.

Zalkind, D., Ananda, G. K., Chetan, M., Martin, D. P., Bay, C. J., Johnson, K. E., Loth, E., Griffith, D. T., Selig, M. S., and Pao, L. Y. (2019). System-level design studies for large rotor. *Wind Energy Science*, 4:595–618. https://doi.org/10.5194/wes-4-595-2019.

Chapter 3

Conclusions

The commercial Suzlon S111 2.1MW class IIIA wind turbine has been compared in the conventional upwind rotor configuration to the downwind rotor configuration.
This study has shown, that the tower clearance can be increased by changing an upwind configuration into a downwind configuration since the design driving wind speed changes. The downwind coned rotor is subject to lower flapwise bending loads than the upwind rotor. The major drawbacks of the downwind configuration are firstly an increased tower bottom bending load, as the gravity overhanging moment of the rotor-nacelle assembly coincides with the moment due to the thrust. Secondly, the downwind coned rotor shows a lower AEP production than the upwind rotor. Thirdly, the tower shadow effect increases the fatigue loads.
A lower edgewise damping of the foreward whirl mode has caused high edgewise fatigue and extreme loads. The change in configuration from upwind to downwind has decreased to out-of-plane components of the edgewise mode shapes. Cone angle and tower torsional stiffness are an opportunity to increase the modal out-of-plane components. The downwind configuration would benefit from a smaller cone angel than the upwind configuration and could benefit from a lattice tower structure due to the low tower torsional stiffness.
Within the employed simulation framework the impact of the tower shadow onto the fatigue and also extreme loads is most likely under predicted, since increased vorticity behind the tower has been neglected. From literature it can be concluded that measures need to be taken to alleviate the impact of the tower shadow, onto the downwind rotor. Not only to alleviate load fluctuations, but also to reduce

low frequency noise.
Despite a common perception of downwind rotors the investigations for a free yawing configuration showed severe yaw misalignment. The tilt angle introduces a projection of the turbine torque onto the yaw bearing as well as a moment due to the wind speed projection. These external moments are balanced due to aerodynamic stiffness from wind speed projections but also induction of a yawed rotor. As the induction decreases the misalignment increases above the optimal tip speed ratio. High cone angles can be used to increase the aerodynamic yaw stiffness and therefor improve the alignment with the wind direction. The increased aerodynamic stiffness from high cone angles can also be used to stabilize a dynamic equilibrium yaw position of non-tilted rotors.
Due to the alignment of the overhanging gravity moment of the rotor-nacelle assembly the starting and stopping routines require different pitch speed in the downwind configuration than in the upwind configuration. For the start-up the pitch speed has to be lower in the downwind configuration, for the shut-down the pitch speed has to be faster. In both cases the pitch speed is driven by the tower bottom bending loads.
Rotors designed for downwind configurations can be lighter than for upwind configurations, due to the decrease in flapwise extreme loads and the release in the tower clearance constraint. However, due to the increased tower loads hardly any difference in the turbine CAPEX is achieved between the upwind and the downwind configuration for the S111. Due to the lower AEP of the downwind configuration the COE of the upwind redesign remained lower than the COE of the downwind redesign.
Future work should investigate the impact of the tower shadow in more detail. The impact of the additional vorticity on the rotor loads has to be quantified. Also tower shadow mitigation solutions should be investigated regarding the impact on the loads the turbine noise, but also regarding reliability and costs.
The studies of the difference in edgewise damping could identify a difference in the modal displacement as the main reason for the difference in damping. The causation of the change in the mode shapes should be investigated in depth. Understanding this phenomena is important to be able to design turbines with a high edgewise damping to decrease turbine loads.
If the design of a free yawing downwind configuration is chosen more investigations need to be done regarding the rotor configuration required to guarantee a yaw alignment within certain limits. Alternative future work could also regard a stable yaw position through a cyclic pitch system.
Particular design options and solutions need to be regarded from an economical point of view. This means that more comprehensive but still realistic cost models are required to evaluate design changes. This should include the reflection of design changes like the tower configuration e.g. a wired tower or a lattice tower.

Also a realistic reflection of off-the-shelf components such as generator or gearbox would be important to evaluate the impact of rotor diameter changes.
Especially regarding the rotor design many more parameter, such as cone and tilt angle or rotor diameter are expected to impact the design costs from either a load or AEP perspective. The investigations within this study should be extended to much broader design space to evaluate the downwind configuration against the upwind configuration. A full turbine redesign including also hub, nacelle, shaft and tower could benefit the downwind configuration.
For broader investigations the impact controller should be part of the design investigations rather than a retro-fit. Upwind configuration could benefit from peak-shaving with increased tower clearance, reduced flapwise loads, no penalty on the tower bending moments, but reduced AEP. Such an upwind configuration could be hard to out-compete by a downwind configuration.
Overall, it can be concluded from this study, that the 2.1MW example turbine has a lower COE in the upwind configuration than the downwind configuration if the rotor design is restricted to planform and structural redesign.

Part II

Chapter 4

Changes in design driving load cases: Operating an upwind turbine with a downwind rotor configuration

---

The following chapter presents the article written for the comparison of a full design loads bases between the upwind turbine configuration and the downwind turbine configuration, in the accepted version, formatted for the thesis format, with friendly permission of John Wiley & Sons.

Changes in design driving load cases: Operating an upwind turbine with a downwind rotor configuration; Gesine Wanke, Leonardo Bergami, Torben J. Larsen and Morten H. Hansen; *Wind Energy*; Vol. 22; p. 1500-1511;
 DOI: https://doi.org/10.1002/we.2384

Manuscript received: 24 August 2018
Manuscript revised: 29 March 2019
Manuscript accepted: 24 May 2019

Changes in design driving load cases: operating an upwind turbine with a downwind rotor configuration.

Gesine Wanke[1], Leonardo Bergami[1], Torben J. Larsen[2], Morten H. Hansen[3]

[1] Blade Science Center Suzlon, Vejle Denmark
[2] DTU Wind Energy, Technical University of Denmark, Roskilde, Denmark
[3] Mads Clausen Institute, University of Southern Denmark, Sønderborg, Denmark

Correspondence: Gesine Wanke, Suzlon Blade Science Center, Havneparken 1, 7100 Vejle, Denmark. E-mail: gesine.wanke@suzlon.com

Abstract

This work considers the design driving load cases from a full design load basis analysis on an upwind turbine changed into a downwind configuration. The upwind turbine is a commercial class IIIA 2.1MW turbine, manufactured by Suzlon. The downwind turbine shows an increase in the normalized tower clearance by 6%, compared to the upwind concept. Removing the blade prebend increases the normalized minimum tower clearance by 17% in the downwind configuration compared to the upwind configuration. The extreme loads on the longitudinal tower bottom bending moment are seen to generally increase by 17% due to the overhanging gravity moment of the rotor-nacelle assembly. The extreme blade root bending moments are reduced by 10% flapwise, due to the coning of the rotor in downwind direction. The fatigue loads suffer from the tower shadow, leading to an overall increase of the fatigue loads in the blades with up to 5% in flapwise direction in the downwind configuration. Due to blade deflection and coning direction, the downwind configuration shows a 0.75% lower annual energy production. Removing the prebend increases the annual energy production loss to 1.66%.

Keywords downwind rotor, design loads basis, extreme loads, fatigue loads

4.1 Introduction

Over the recent years, most research effort has been focused on wind turbines with an upwind concept, where the rotor is placed in front of the tower with respect to the wind direction. The aeroelastic behavior of wind turbines is well known for upwind concepts. In this case, the clearance between tower and blades is a major restriction in the blade design. Placing the rotor behind the tower could give the freedom of larger rotors for higher power production or more flexible blades, saving on the blade material and potentially decreasing the loads on tower, nacelle and hub. Although, load cases of fault situations, such as the emergency stop of the turbine, where the blades are unloaded, may restrict the blade flexibility with a minimum tower clearance in a downwind configuration.
This work investigates the following hypothesis: changing an upwind into a downwind concept leads to major changes in the design driving load cases, increasing the freedom for blade design.
According to Kiyoki et al. (2016) only the Japanese manufacturer Hitachi is commercially selling a downwind concept of 2MW and testing a 5MW prototype. The relaxation of the tower clearance in the design constraints made the concept attractive for typhoon sites.
More flexible blades may lead to loss in power production, due to a decrease of the rotor area under blade deflection. However, a power increase has been observed in several studies. Kress et al. (2016) observed a power increase of 3% of the downwind configuration compared to the upwind configuration in a Computational Fluid Dynamic (CFD) simulations. The authors observed a higher output due to a higher angle of attack across the blade spanwise direction originating from a favorable blockage effect of the nacelle in the downwind configuration. Yoshida (2006) observed an increase in annual energy production (AEP) by 7.5% in field tests, comparing an upwind configuration against a downwind configuration in complex terrain. The study showed a power increase due to the rotor alignment with the inclination angle of the wind field of 1 to 11%. In the downwind configuration, the tilt angle counteracted the inclination angle of the wind resulting into a more perpendicular inflow on the rotor plane, than in the upwind configuration.
Ning and Petch (2016) compared the cost advantage of upwind concepts of 5 - 7MW turbines for different wind classes with corresponding downwind concepts. In their work, a multidisciplinary optimization framework was used to design several rotors of different diameter for different wind conditions, with and without tower clearance constraint. Their work showed clear dependencies of the results on the site conditions. The highest cost advantage of a downwind concept was found for the 5MW turbine for sites of lower average wind speed and moderate

turbulence, with a cost advantage of 1-2% of levelized cost of energy (LCOE). Sites with higher average wind speeds showed an increase in cost, due to the increase in tower bending moments from extreme loads, caused by the overhanging moment of the rotor. Furthermore, a clear dependency of the LCOE on the rotor diameter was observed, showing the lowest LCOE for medium sized rotors.
The downwind concept comes further with the option of a passive yaw mechanism for the alignment of the rotor, as the aerodynamic forces could potentially align the rotor with the wind direction. It should be noted that the advantage of a passive yaw mechanism comes from the elimination of load cases with extreme yaw error in the design load assessment. These cases are often associated with very high loads that are restricting the turbine design. The cost advantage of a passive yaw system in itself is small, since a yaw mechanism will still be required for cable unwinding. Glasgow and Corrigan (1983) investigated the alignment and stability of a passive yaw system already in 1983, by testing the passive yaw alignment of different rotors in a downwind configuration on a 100kW machine. They observed significant differences in the equilibrium yaw position, where some rotors were not able to align passively with the wind direction. Also they observed yaw motions around these equilibrium positions. If the equilibrium position of the rotor shows severe misalignment with the wind direction, power losses can be expected, as shown in field measurements already by Corrigan and Viterna (1982) in 1982.
The major challenge of a downwind concept is the change of loading on the blades when they are passing the tower. The velocity deficit behind the tower gives a reduction in normal force on the blade of about 20%, as observed for example by Zahle et al. (2009) The velocity deficit leads also to a rapid fluctuation in the angle of attack as the blade passes through the wake.
Glasgow et al. (1981) compared the flapwise bending loads of a blade of a 100kW machine with lattice tower in an upwind configuration and a downwind configuration. While they were not able to measure a difference in the mean flapwise bending load, they observed a significant increase in the cyclic flapwise bending load within one rotor revolution due to the flow disturbance from the tower.
Reiso and Muskulus (2013) studied the fatigue load of a downwind configuration compared to an upwind configuration of the 5MW NREL reference turbine. They observed an increase of around 20% in the damage equivalent fatigue load for the flapwise blade root bending moment and for the tower base bending moment. Their study further investigates the reduction of the fatigue load due to an airfoil-shaped tower fairing combined with a mass and stiffness reduction of the blade. This approach shows 5% fatigue load reduction for the blade root flapwise bending moment compared to the upwind configuration. However, due to the size of the fairing the rotor overhang had to be increased. This resulted into a mean tower bottom bending moment increase by around 20%.

For this numeric study, a commercial 2.1MW Suzlon turbine is changed from an upwind configuration into a downwind configuration by realigning the turbine components. Assembling the turbine with the same components could be economically beneficial, as blade moulds could be reused. As the direct change of configuration is seen to be only little beneficial a downwind configuration without blade prebend is also compared to the upwind configuration. Full design load basis are calculated according to the IEC-Standard (IEC (2014)) and the three configurations are compared in terms of minimum tower clearance, the extreme loads and the fatigue loads. From the load basis calculation the design driving load cases are identified. The 10-minute mean load is shown for certain sensors to explain major load differences between the upwind and the downwind configurations. It is shown that the design driving load situations for the tower clearance change from high blade loading in the upwind configuration to negative blade loading in the downwind configurations. The flapwise blade root moment is seen to decrease due to the coning direction in the downwind configurations when compared to the upwind configuration. The edgewise blade root moments for the downwind configurations are observed to increase for high wind speeds, due to the projection of the centrifugal force. It is confirmed that the tower loads increase in the downwind configurations relative to the upwind configuration due to the overhanging moment of the rotor nacelle assembly. While the flapwise fatigue load of the blade root is seen to increase in the downwind configurations, compared to the upwind configuration, purely due to the tower shadow, the edgewise blade root fatigue load is further increasing due to lower damping of the edgewise forward whirling turbine mode. AEP losses for the downwind configurations due to the tower shadow and the effect of prebend on the AEP are quantified. Finally, the fluctuation of the produced power is assessed.

4.2 Methods

For the study the Suzlon 2.1MW turbine S111 (wind class IIIA) is used. The turbine has a rotor diameter of 112m and a tubular tower of 90m height. The rotor is tilted and coned. The blades are prebended. The turbine is pitch regulated at a rated wind speed of 9.5m/s and the operational range is simulated between 4m/s and 21m/s.
To compare the upwind configuration with the downwind configuration, the downwind configuration is reassembled with the same turbine bodies: The rotor is moved behind the tower, the nacelle structure with the shaft is rotated 180° around the yaw axis. The assembly results into a downwind configuration, where tilt and cone increase the clearance between blades and tower. The

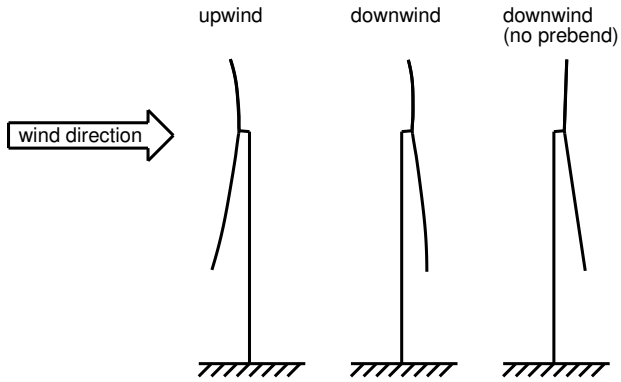

Figure 4.1: Sketch of the side view of the the turbine configurations upwind, downwind and downwind without prebend.

rotational direction seen from a global frame of reference is clockwise for all configurations when looking at the turbine with the wind in the back. Since the blades are prebended towards the pressure side, the prebend increases the distance between blades and tower in the upwind configuration, but decreases it in the downwind configuration. The unloaded tower clearance, normalized with the distance between the blade tip and tower of the upwind configuration, is 100% for the upwind configuration, while the downwind configuration has an unloaded tower clearance of only 62%. In a more realistic design, the downwind rotor blade has no prebend, to increase the freedom in the blade design. The downwind configuration without prebend is therefore also simulated to see the effect of the prebend. The downwind configuration without prebend has an unloaded tower clearance of 81%. Figure 4.1 shows a sketch of the three evaluated configurations from the side view, scaled from the original turbine measures without any loading. A full design load basis (DLB) is calculated with HAWC2 (Larsen and Hansen (2014) simulations (Version 12.7)), according to IEC 61400-1 standard edition 3(IEC (2014)). The IEC 61400-1 standard gives a guideline to calculate loads on the wind turbine created within different situations (Design Load Cases (DLC)). These situations regard normal operation with different wind conditions (DLC 1.x), failure of the control system or the electrical systems (DLC 2.x), start-up and shut-down scenarios (DLC 3.x to DLC 5.x), scenarios with parked turbine configurations (DLC 6.x) and situations with a locked rotor (DLC 7.x and DLC 8.x). The standard prescribes the turbulence intensity for each load case and wind speed, as well as the wind shear to be applied. To each design load case, a different safety factor is assigned by the standard. For the load calculation the DLB is set up according to the design load basis for onshore turbines by Hansen

et al. (2015), which is a fully documented interpretation of the IEC standard. The design load basis contains a tabulated description of the wind field parameter and safety factors. The simulation setup applies the Beddoes-Leishman dynamic stall model and Prandtl's tipp loss correction for the aerodynamics of the blade. Yawed inflow is regarded by HAWC2 by adjusting the mean induction and applying a correction on the induction depending on the azimuth position of the blade. The background of the model has been described by Madsen et al. (2011). All simulations are performed with a pitch imbalance of $\pm$ 0.3° and a mass imbalance of 1% on one rotor blade. All simulations are performed with a flow inclination angle of 8°. It is assumed that the turbine operates under normal condition 50% of the time at 0° average yaw angle and 25% of the time at + 7° and − 7° average yaw angle. The number of turbulence seeds realized are according to the DLB and the same turbulence seeds are used for the upwind and the downwind configurations. For the upwind configuration, a potential flow tower shadow model is used, while a jet-flow deficit model is used for the downwind configurations, as described in the HAWC2 manual(Larsen and Hansen (2014)). For simulations with a wind direction of yaw errors between + 90° and + 270°, the upwind configuration is subject to the jet-flow deficit model and the downwind configuration is subject to the potential flow model. An exception are rotating wind fields, where the range of wind direction covers 360°. Here the jet-flow deficit tower shadow model is applied for the downwind configurations and the potential flow model for the upwind configuration. Additionally, the downwind configurations have been simulated with a potential flow model during normal operation to quantify the effect of the tower shadow model, especially on fatigue loads and the AEP.
For "publishability", the controller set-up from the technical university of Denmark (DTU)(Hansen and Henriksen (2013)) has been adopted. It is a controller for pitch regulated, variable speed wind turbines with a partial load and full load control strategy, as well as a switching routine between the two. In the partial load region, the balance between generator torque and aerodynamic torque is used for optimal C_p tracking. In the full load region, torque limits are applied by following a constant torque or constant power strategy. Different events can be initiated from the controller, such as start-up, shut-down or failure situations. For the design load case 2.2b, failure of pitch systems (one blade getting stuck), the suggested routine from Hansen et al. has been changed. In the failure scenario the pitch actuator has been adjusted according to the controller routine of the turbine. In this case, the pitch angle on one blade will be kept constant at the current pitch angle at the time of failure. The deviation of the pitch angle from the set point of the controller initiates a stop of the turbine. Further, a pitch run away (DLC 2.2p) is not included, as the failure mode is prevented from the type of pitch actuators used. For the scenario of a parked turbine with high yaw errors (DLC 7.1), the yaw error is interpreted as wind direction change of

360° within 570 seconds.
For the AEP and fatigue load calculation, a mean wind speed of 7.5m/s and a shape factor k=2 are used for the Weibull distribution of the wind, as specified for class III turbines in the IEC standard. The power curves are calculated with wind speeds steps of 1.0 m/s with 6 turbulence seeds per wind speed bin with the normal turbulence model and without yaw error. For further investigation on energy production the AEP is also calculated from simulations without inclination angle. The normalized power fluctuation is regarded for each wind speed bin to investigate the power quality. Therefore the standard deviation of the power is divided by the mean of the power for each wind speed bin. From the load simulations including the inclination angle the 10-minute mean load is calculated over wind speed to show general changes in loading between the configurations.
For the post-processing of the extreme values, the safety factors are applied and the resulting extreme values are averaged over the six highest extremes from simulations differing only in turbulence seeds. If less than six turbulence seeds were simulated, the average represents values from all the available seeds. For the tower clearance the safety factor is applied to the blade deflections. The normalized tower clearance $TC_{normalized}$ is calculated from the simulated tower clearance $TC_{simulated}$ as

$$TC_{normalized} = \frac{TC_{unloaded}\,(1 - SF) + TC_{simulated} SF}{TC_{upwind,\ unloaded}} \tag{4.1}$$

Where $TC_{unloaded}$ is the unloaded tower clearance individual for each configuration, $TC_{upwind,\ unloaded}$ is the unloaded tower clearance of the upwind configuration and SF is the combined safety factor containing a load case specific contribution and a contribution for the elastic properties of the material. The tower clearance is calculated as an average over simulations with different turbulence seeds.
Further investigations had to be made regarding fatigue loads and the stability tool HAWCStab2 (Hansen (2004) (Version 2.14)) has been used to determine the damping of certain aeroelastic turbine modes.

4.3 Results

In the following section, the results of the load simulations for the full design load basis are presented. Presented are the minimum tower clearance, extreme loads and fatigue loads for selected sensors and the power production. For the minimum tower clearance and the extreme values the three most extreme results are plotted to give a better overview about the general load level. However, design driving for

the load sensor is only the design load case giving the highest extreme load or the minimum tower clearance. The selected load sensors are the blade root moment sensor, the main bearing yaw and tilt sensor in a non rotating reference frame, and the tower bottom sensors. These sensors are selected as they represent the loads on the most costly components of the turbine. These sensors also give a good overview over the over all trends in change in loading situations when changing the upwind configuration into a downwind configuration. However, with only being able to present a limited number of sensors this work does not present a complete picture of all load sensor on a wind turbine. All results are shown as relative comparison between the downwind configurations and the upwind configuration. They are expressed relative to the result of the upwind configuration. The results for the different load cases are identified with the number of the design load case (DLC), the wind speed (ws) and the wind direction (dir). Blade root bending moments in flap and edgewise are stated in the pitched blade root coordinate system.

4.3.1 Tower clearance

The tower clearance is normalized with the distance of the unloaded blade tip to the tower of the upwind configuration. Figure 4.2 shows the comparison of the normalized tower clearance for the upwind, the downwind and the downwind configuration without prebend. The figure shows, that none of the configurations is subject to tower strikes. Under loading the tower clearance has decreased to 6% in the upwind configuration, to 12% in the downwind configuration and to 23% in the downwind configuration without prebend. The deflection of the blade tip in the upwind configuration from the unloaded position towards the tower is 94%, due to the loading. In the downwind configuration the blade tip deflects from an unloaded position of 62% by 50% under loading. The downwind configuration without prebend shows under loading a blade tip deflection of 58% decreasing tower clearance from 81% to 23%. With the change of configuration the load cases driving the minimum tower clearance have not changed. Determining is the operation in extreme turbulence (DLC 1.3). The critical wind speeds have changed from wind speeds around rated power in the upwind configuration, to high wind speeds in both downwind configurations.
Characteristic cases in the upwind configuration regarding the minimum tower clearance are cases with high blade loading. The high loading leads to high deformations, for example the operation at extreme turbulence around the thrust peak. In contrast to this, the characteristic situations for the minimum tower clearance in the two downwind configurations are situations, where the blades

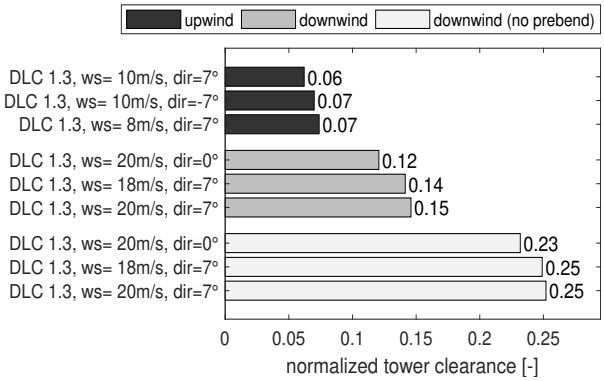

Figure 4.2: Normalized tower clearance compared between the upwind, the downwind and the downwind configuration without prebend from the load cases with the three lowest values. Design load case: DLC 1.3: power production in extreme turbulence.

experience a negative lift force due to the operation at high wind speeds and high pitch angles. Due to this change in characteristic situation, the lower blade deflection in the two downwind configurations can overcome the lower unloaded tower clearance.

4.3.2 Extreme loads

In the following subsection, the extreme load results are shown. The extreme loads are normalized with the highest load observed for the upwind configuration. For further explanation of the results, the 10-minute mean load is shown over wind speed for selected sensors.
Figure 4.3 shows the normalized extreme and the normalized 10-minute mean flapwise blade root bending moments for the upwind configuration, the downwind configuration and the downwind configuration without prebend. The figure shows on the left that the extreme flapwise blade root bending moment is lower in both downwind configurations compared to the upwind configuration. The extreme blade root bending moment reduces 10% when the upwind configuration is changed into a downwind configuration. The design driving load cases are determined by operation at extreme yaw error (DLC 2.2y) at high wind speeds. The analysis of the 10-minute mean flapwise bending moment shows on the right of Figure 4.3 that the mean flapwise blade root bending moment at the thrust peak

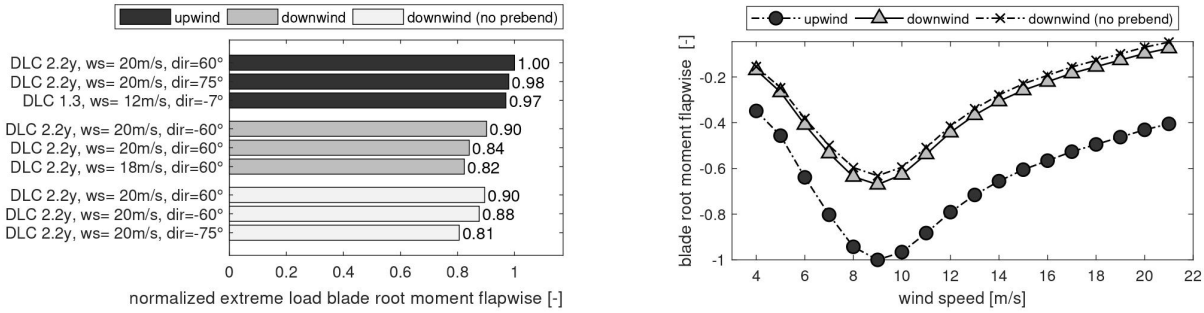

Figure 4.3: Comparison of flapwise blade root bending moments between the upwind, downwind and the downwind configuration without prebend. Left: comparison of the highest three normalized flapwise blade root bending moments. Right: comparison of the normalized 10-minute mean flapwise blade root bending moments over wind speed. Design load cases are: DLC 2.2y power production with abnormal yaw error and DLC 1.3 power production in extreme turbulence.

is 33% lower in the downwind configuration than in the upwind configuration. The downwind configuration without prebend shows a mean load reduction of 37% at the thrust peak compared to the upwind configuration for the flapwise blade root bending moment.

When the blades are loaded in the upwind configuration the blade tip deflection will increase the rotor area, counter acting the prebend and the cone angle. As the downwind configurations are coned in the same direction as the blade tip deflects under loading, any deflection further out of the rotor plane than the straight blade will decrease the rotor area and unload the rotor blades. The effect of the change of cone direction, when the upwind configuration is changed into the downwind configuration, can be seen from the mean flapwise bending moments to have the highest load reducing effect. The increased out of plane deflection from the downwind configuration without prebend has a small load decreasing effect on the mean flapwise bending moments compared to the effect of cone. The maximum flapwise blade root bending moments are in both downwind configurations the same. From the time series of the according simulations, it is observed that the blade deflection of the two downwind configurations is very similar, in cases of high yaw errors. Therefore, there is no unloading effect due to larger out of plane blade deflection in DLC 2.2y, when the prebend is removed from the downwind configuration.

Figure 4.4 shows the normalized extreme and 10-minute mean loads of the edge-

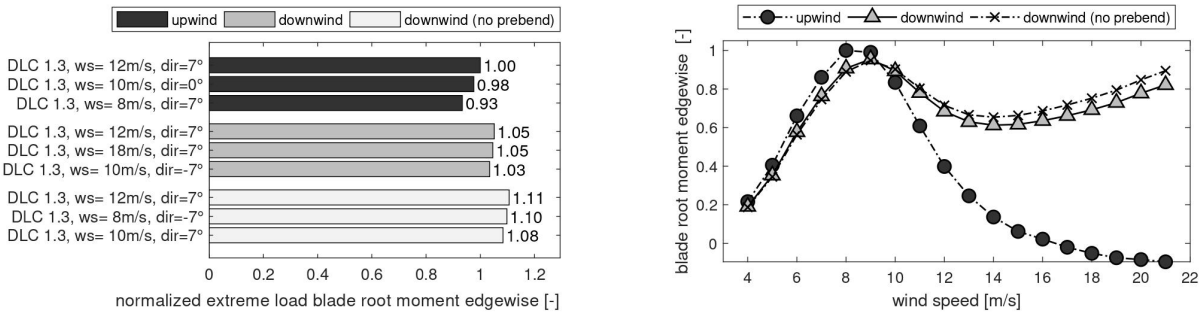

Figure 4.4: Comparison of edgewise blade root bending moments between the upwind, downwind and the downwind configuration without prebend. Left: comparison of the highest three normalized edgewise blade root bending moments. Right: comparison of the normalized 10-minute mean edgewise blade root bending moments over wind speed. Design load case is: DLC 1.3 power production in extreme turbulence.

wise blade root bending moments for the upwind configuration, the downwind configuration and the downwind configuration without prebend. The figure shows a 5% higher extreme edgewise blade root bending moment in the downwind configuration compared to the upwind configuration. The downwind configuration without prebend shows a 11% higher extreme edgewise blade root bending moment than the upwind configuration. Design driving is for all configurations the operation at extreme turbulence for wind speeds close to the thrust peak at yaw errors. For the downwind configuration a high edgewise blade root bending moment is also observed for high wind speeds. From the 10-minute mean of the edgewise bending moment, a change in the load distribution over wind speed is observed, when the upwind configuration is changed into a downwind configuration. In the upwind configuration the mean blade root edgewise bending moment increases with the wind speed, and decreases strictly after reaching a maximum at 8 m/s. In the downwind configurations the mean edgewise blade root bending moments increase with the wind speed until the thrust peak at 9m/s. However, after a decrease in the edgewise blade root bending moment for wind speeds up to 14 m/s, an increase in the mean edgewise blade root bending moment is observed for high wind speeds.

The difference in the mean edgewise blade root moment is mainly due to the projection of the centrifugal force. The combination of cone and pitch angle lead to a contribution of the centrifugal force to the mean edgewise bending moment (with $\sin(pitch)\sin(cone)$). For the operational point 17m/s the centrifugal force

contributes to the mean edgewise bending moment with -2.5% in the upwind configuration and with +2.5% to the downwind configuration. 2.5% of centrifugal load are equivalent to 32% of mean edgewise blade root bending moment of the upwind configuration at the thrust peak. The change of the sign from the contribution of the centrifugal load, is due to the inverted sign of the cone angle when the upwind configuration is changed into the downwind configuration. Thus, the difference observed in the edgewise blade root moment mean load is due to the projection of the centrifugal force to the edgewise bending moment. Further investigations of the aeroelastic modes with HAWCStab2 showed that the first edgewise forward whirling mode is significantly lower damped around rated power in the downwind configuration. Removing the prebend decreases the damping in the downwind configuration even further. For high wind speeds, close to cut-out wind speed, the damping increases for both downwind configurations. Due to this change in damping the load fluctuations around rated power are higher than for the upwind configuration. Therefore a significant increase in extreme loads can be observed for the edgewise blade root bending moment and the downwind configuration without prebend shows the highest extreme load level. Whether a lower damped first edgewise forward whirling mode is general for downwind configurations and which parameters are influencing it, needs to be investigated in future work.

Figure 4.5 shows the comparison of the the tower bottom bending moment in longitudinal direction for the upwind configuration, the downwind configuration and the downwind configuration without prebend. The normalized extreme load is displayed on the left and the normalized 10-minute mean load over wind speed on the right. It can be seen that the extreme load level for the longitudinal tower bottom moment is generally higher in the two downwind configurations than in the upwind configuration. The highest extremes of the longitudinal tower bottom moment are a result from the shut-down during extreme operational gust (DLC 4.2) and operation at extreme yaw errors (DLC 2.2y) for the upwind configuration. In the two downwind configurations, the highest extremes of the longitudinal tower bottom moment are determined by the shut-down at extreme operational gust and the start-up situation (DLC 3.1). From the 10-minute mean load, it is observed that the two downwind configurations are subject to higher longitudinal tower bottom bending moments. The mean longitudinal tower bottom bending moment at the thrust peak is 17% higher in the two downwind configurations than in the upwind configuration. There is no significant difference between the two downwind configurations.

Generally, start-up and shut-down situations can cause the longitudinal motion of the turbine, associated with high tower loads. The longitudinal tower bottom bending moment increases, due to the overhanging moment of gravity of the rotor-nacelle assembly in the two downwind configurations, compared to the up-

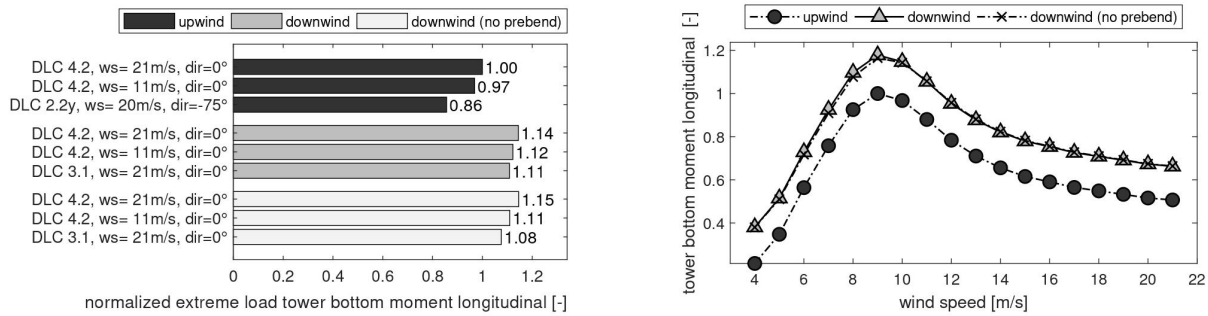

Figure 4.5: Comparison of longitudinal tower bottom bending moments between the upwind, downwind and the downwind configuration without prebend. Left: comparison of the highest three normalized longitudinal tower bottom bending moments. Right: comparison of the normalized 10-minute mean longitudinal tower bottom bending moments over wind speed. Design driving load cases are: DLC 4.2 shut down during extreme operational gust, DLC 2.2y operation at extreme yaw errors, DLC 3.1 start up.

wind configuration. While the overhanging moment is counteracting the moment from the thrust force in the upwind configuration, the overhanging moment and the thrust force moment are acting in the same direction in the two downwind configurations. The increase in tower bottom bending moment in the downwind configurations due to this geometrical alignment of the gravity force is 17% compared to the maximum 10-minute mean load from DLC 1.2 in the upwind configuration. The overhanging moment is seen to be determining the load increase in the tower bottom bending moment. The difference in the overhanging moment of the rotor-nacelle assembly between the two downwind configurations is very small, since the contribution of the mass at the blade tip is small compared to the mass of nacelle, shaft and the blade root part. Therefore, the downwind configuration without prebend shows no significant difference in the the extreme loads.
Table 4.1 shows a summary of the design driving loads and load cases for the tower, blades and main bearing.

With the change from the upwind to the downwind configurations, the design driving tower bending loads (longitudinal and lateral), as well as edgewise blade

Table 4.1: Difference in the highest normalized extreme value between the upwind and the downwind configuration, as well as the upwind and the downwind configuration without prebend, and the design driving load cases for all three configurations. Design driving load cases are: DLC 4.2 shut down during extreme operational gust, DLC 6.2 idling at abnormal yaw error, DLC 1.3 power production in extreme turbulence, DLC 2.2y operation at extreme yaw errors.

load sensor	**Δ normalized extreme load [-]**		**DLC**			
	downwind	downwind (no prebend)	upwind	downwind	downwind (no prebend)	
tower bottom flange longitudinal	+0.14	+0.15	DLC 4.2	DLC 4.2	DLC4.2	Figure 4.5
tower bottom flange lateral	+0.10	+0.08	DLC 6.2	DLC 6.2	DLC 6.2	
tower bottom flange torsional	-0.06	-0.09	DLC 1.3	DLC 1.3	DLC 1.3	
blade root flange flapwise	-0.10	-0.10	DLC 2.2y	DLC 2.2y	DLC 2.2y	Figure 4.3
blade root flange edgewise	+0.05	+0.08	DLC 1.3	DLC 1.3	DLC 1.3	
blade root flange torsional	+0.05	+0.03	DLC 6.2	DLC 6.2	DLC 6.2	
main bearing tilt	+0.02	+0.05	DLC 2.2y	DLC 1.3	DLC 1.3	
main bearing yaw	-0.07	-0.10	DLC 1.3	DLC 1.3	DLC 1.3	

bending and the torsional blade load are increasing. Also for the main bearing tilt load, a load increase is observed in the downwind configurations compared to the upwind configuration. The flapwise blade bending load, the tower torsional and the main bearing yaw load are lower in the downwind configurations than in the upwind configuration. The downwind configuration without prebend showed generally very similar load levels to the load level of the downwind configuration, differing maximum up to 3% from the downwind configuration. It can be seen that the design driving load cases are changing only in the main bearing tilt load with the change from an upwind to a downwind configuration. The design driving load cases are observed to be the same for both downwind configurations.
It should be mentioned that the absolute tower lateral bending moment of both downwind configurations is lower than the maximum tower longitudinal bending moment in the upwind configuration. Like the tower longitudinal bending moment, the main bearing tilt moment increases with the increased overhanging moment of the rotor-nacelle assembly in the downwind configurations compared to the upwind configuration. The tower torsional moment, as well as the bearing yaw moment, are related to the flapwise load of the blades and a load decrease in these sensors is observed, due to the coning in the direction of blade deflection in the downwind configurations.

4.3.3 Fatigue loads

In the following section, the changes in fatigue loads due to the change in turbine configuration are discussed. Figure 4.6 shows the normalized lifetime equivalent load for the flapwise blade root bending moment, over the different load cases of the fatigue load assessment. The load is normalized with the total lifetime equivalent load from the upwind configuration. More than 99% of the lifetime equivalent load in all three configurations is determined by the normal operation (DLC 1.2). The figure shows that the normalized lifetime equivalent load for blade root flapwise bending is in the downwind configuration 5% higher and in the downwind configuration without prebend 4% higher than in the upwind configuration.
To quantify the effect of the tower shadow on the fatigue load, DLC 1.2 has been simulated in the two downwind configurations with the potential flow model. The tower shadow model exchange decreased the flapwise fatigue load in the blade root by 5% in the downwind configuration and by 4% in the downwind configuration without prebend. Thus, the same blade root flapwise fatigue load level as in the upwind configuration is achieved and the tower shadow is seen to be the causation of the increase in flapwise blade root fatigue loads.

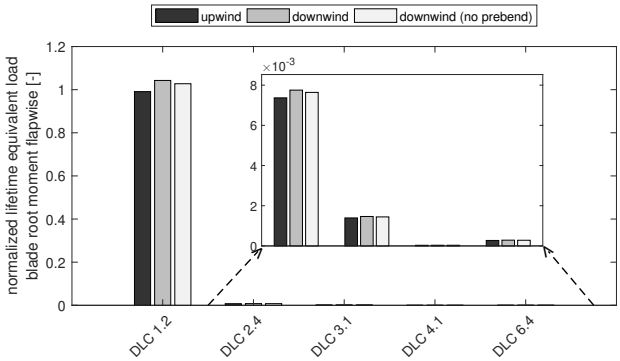

Figure 4.6: Comparison between the upwind configuration, the downwind configuration and the downwind configuration without prebend in normalized lifetime equivalent load for the flapwise blade root bending moment. Evaluated design load cases are: DLC 1.2 normal operation, DLC 2.4 power production with large yaw errors, DLC 3.1 Start-up in normal wind profile DLC 4.1 shut- down in normal wind profile, DLC 6.4 parked.

Table 4.2 shows the lifetime equivalent load of the investigated sensors for normal operation.

The table shows a general increase of the fatigue loads when the upwind configuration is changed into a downwind configuration. The only exceptions are fatigue loads of the longitudinal tower bottom bending moment and the main bearing yaw moment, which are decreasing in the downwind configurations, compared to the upwind configuration. The fatigue load of tower bottom flange torsion remains unchanged for the downwind configuration, and decreases slightly in the downwind configuration without prebend, compared to the upwind configuration. Removing the prebend in the downwind configuration changes the relative difference in fatigue load level compared to the upwind configuration for most sensors not more than 2%. Two exceptions for the downwind configuration without prebend are the blade root torsion which increases from 2% to 45% above the fatigue load level of the upwind configuration and the blade root edgewise fatigue load which increases from 7% to 11% higher fatigue load than in the upwind configuration.
With the exchange of the tower shadow model from the jet-flow deficit model

Table 4.2: Difference in the normalized lifetime equivalent load between the upwind configuration, the downwind configuration and the downwind configuration without prebend for DLC 1.2 (normal operation).

load sensor	**Δ normalized life time equivalent load [-]** downwind vs. upwind	downwind (no prebend) vs. vs. upwind	
tower bottom flange longitudinal	-0.02	-0.03	
tower bottom flange lateral	+0.03	+0.05	
tower bottom flange torsion	-0.00	-0.01	
blade root flange flapwise	+0.05	+0.04	Figure 4.6
blade root flange edgewise	+0.07	+0.11	
blade root flange torsion	+0.02	+0.45	
main bearing tilt	+0.06	+0.04	
main bearing yaw	-0.02	-0.04	

to the potential flow model for the downwind configuration, the fatigue load of the tower lateral bending and the blade root flapwise bending are seen to reach the same level as in the upwind configuration. For the downwind configuration with potential flow model the tower torsion and the main bearing tilt fatigue load decrease to a fatigue load level 2% below the level of the upwind configuration. For the downwind configuration with potential flow model the main bearing yaw fatigue load level is seen to decrease to a load level 3% below the load level of the upwind configuration. For the tower longitudinal bending the fatigue load level decreases to a fatigue load level 4% below the level of the upwind configuration.The blade torsion fatigue load of the downwind configuration decreases 14% below the level of the upwind configuration with the change to a potential flow model. In case of the edgewise blade root bending a fatigue load reduction of 2% is observed with the exchange of the tower shadow model from jet-flow deficit to potential flow for the downwind configuration. However, the fatigue load does not reduce to the level of the upwind configuration. For the tower lateral fatigue load no load reduction can be observed for the downwind configuration with the exchange of the tower shadow model to the potential flow model.
The tower shadow is seen to be the main reason for the increase in fatigue loads when the upwind configuration is changed into a downwind configuration. The reduction of the fatigue load level for the downwind configurations and the downwind configuration with potential flow to a level below the fatigue load of the upwind configuration can be explained with less variation of the inflow condition. In the downwind configuration, the tilt angle counter acts the inclination angle of the wind. In the upwind configuration on the other hand, the tilt and the inclination angle both lead to an increased flow variation over the rotor plane. The blade torsion fatigue load increases drastically when the prebend is removed from the downwind configuration due to the gravity loading when the blade deflects further out of the rotor plane. The lower damping of the first edgewise forward whirling mode explains the increase of fatigue loads for the edgewise blade root moment in the downwind configurations, which is not due to the tower shadow. The tower lateral bending is coupled to the edgewise motion of the blades and excited by the lower damped blade motion in the downwind configuration. The increase in the tower lateral fatigue load when changing an upwind into a downwind configuration is not due to the tower shadow.

4.3.4 Power output

In the following section, the power production of the three turbine configurations the annual energy production as well as the power fluctuations are discussed.

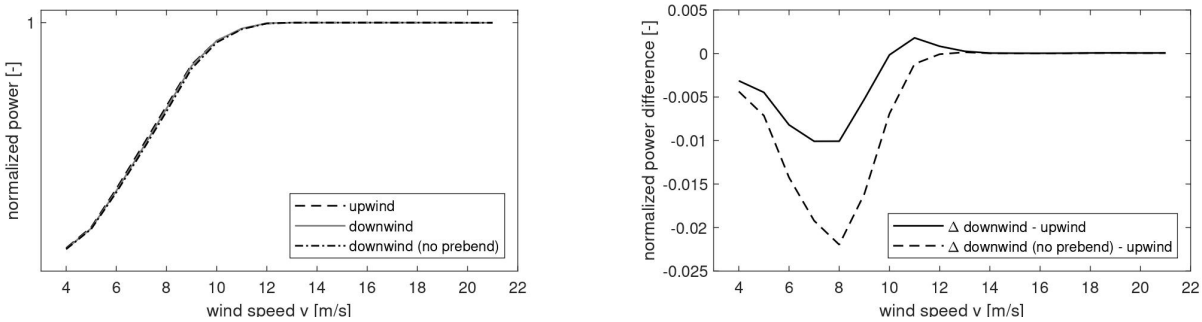

Figure 4.7: Comparison of the upwind configuration, the downwind configuration and the downwind configuration without prebend. On the Left: comparion of normalized power curve from DLC 1.2 without yaw misalignment, plotted with bin averages for 1m/s bins. On the right: comparison of the normalized difference in power power production between downwind configurations and upwind configuration.

Figure 4.7 shows the normalized power curves and the difference in power over wind speed. The figure shows on the left that the power production in all three configurations, upwind and downwind and downwind without prebend, is similar below rated power. It can be seen that the upwind configuration has a slightly higher power output than the two downwind configurations below rated power. The downwind configuration without prebend shows the lowest power production of the three configurations, below rated power. Above rated power no difference between the configurations is observed. The maximum difference is a 1% lower power production at 8 m/s in the downwind configuration than in the upwind configuration. For the downwind configuration without prebend it can be seen that the losses are significantly higher, up to 2.3% at 8m/s, compared to the upwind configuration. Overall, this leads to a 0.75% lower AEP in the downwind configuration and a 1.66% lower AEP in the downwind configuration without prebend, compared to the upwind configuration. With the exchange of the jet-flow deficit model to the the potential flow tower shadow model the downwind configuration showed an AEP gain of 0.77% compared to the upwind configuration. Exchanging the tower shadow model to the potential flow model for the downwind configuration without prebend gives an AEP loss of 0.1% compared to the upwind configuration. Simulating the power curves without inclination angle leads to a 1.97% lower AEP in the downwind configuration than in the upwind configuration. Without the inclination angle the downwind configuration without prebend shows 2.78% less AEP than the upwind configuration.

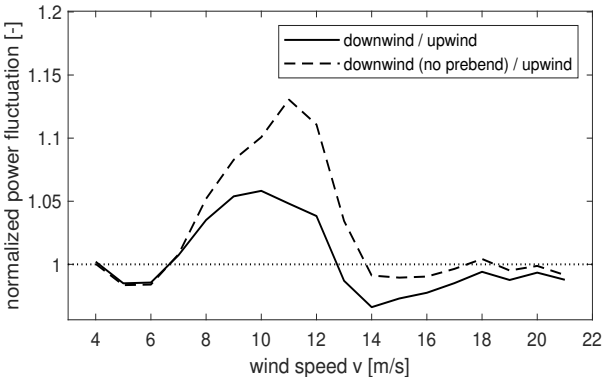

Figure 4.8: Normalized power fluctuation of the downwind and the downwind configuration without prebend from DLC 1.2 without yaw misalignment or inclination angle, plotted with bin averages for 1m/s bins normalized with the respective value of the upwind configuration.

Without the losses from the tower shadow jet-flow deficit model the downwind configuration would show a higher power production since the tilt angle aligns the rotor plane better with the inclination angle of the inflow. The alignment of inclination and tilt angle overcomes losses due to a decreased rotor area, as the cone is in the same direction as the blades deflect under loading for the downwind configurations (see Figure 4.1). Without the prebend in the downwind configuration, the decrease in the rotor area is too large and even with the potential flow tower shadow model the AEP production is lower than in the upwind configuration. Excluding the influence of the inclination angle therefore increases the difference in power production, as the decrease in rotor area decrease becomes the dominant effect.
Figure 4.8 shows the normalized power fluctuations over the wind speed for the simulations without yaw misalignment or inclination angle. The figure shows that the power fluctuations increase for wind speed bins around rated power up to 5% when the downwind configuration is compared to the upwind configuration for equal inflow conditions on the rotor. For the wind speed bins at 5m/s and 6m/s and wind speed bins above 13 m/s the fluctuations are decreased up to 3% below the level of the upwind configuration. For the downwind configuration without prebend the fluctuation is increased up to 13% for the wind speed bin of 11 m/s. The maximum decrease in fluctuations for the downwind configuration without prebend is up to 1% below the fluctuation level of the upwind configuration. Including the inclination angle decreases the fluctuation level of the downwind configurations. The maximum power fluctuation drops in the down-

wind configuration to 1% above the upwind fluctuation level. In all other wind bins the downwind configuration shows a lower fluctuation level than the upwind configuration. In the downwind configuration without prebend the maximum power fluctuation is 5% higher than the power fluctuation in the upwind configuration. Except for the two lowest wind speed bins the power fluctuation in the downwind configuration without prebend remains higher than in the upwind configuration. Exchanging the tower shadow model for the downwind configurations to the potential flow model decreases the power fluctuations for both downwind configurations. For nearly all wind speed bins a power fluctuation level of the upwind configuration or lower is achieved for the downwind configuration. The power fluctuation level of the downwind configuration without prebend remains higher than for the downwind configuration and also remains higher than for the upwind configuration level around rated power.
Without inclination angle the differences in power fluctuations between the downwind configurations and the upwind configuration are determined by the lower edgewise damping of the downwind configurations and the tower shadow effect. Due to the lower edgewise damping the downwind configuration shows a higher power fluctuation level than the upwind configuration. The downwind configuration without prebend shows generally a higher power fluctuation level than the downwind configuration as the edgewise damping is the lowest. If the inclination angle is included the inflow conditions, the downwind configurations are subject to a inflow on the rotor plane with less variation than the upwind configuration. As the inflow in the downwind configurations is closer to being perpendicular to the rotor plane, it compensates for some of the tower shadow effect and some of the effect of the lower edgewise damping.

4.4 Conclusions

The S111 2.1MW turbine in the upwind configuration has been compared to downwind configurations, with and without prebend. With the change into a downwind configuration an increase in tower clearance could be achieved. The initial unloaded tower clearance due to the prebend (62% of the unloaded tower clearance of the upwind configuration) could be compensated by a 44% lower blade deflection in the downwind configuration, resulting into a 6% higher tower clearance. With a configuration without blade prebend, the minimum tower clearance could be increased by additional 11%.
The downwind configurations are benefiting in the flapwise blade root moment from the fact that the coning direction is the same as the deflection direction of the blades in the critical situations. The flapwise extreme load is seen to be 10%

lower in the downwind configurations.
The tilt angle is beneficial for the downwind configurations, as an inclination angle of the wind field is simulated. With the tilt angle a better alignment of the rotor plane with the inflow is achieved for the downwind configurations. The lower inflow variations are beneficial for fatigue loads, and a decrease in the yaw related loads, such as tower torsion or main bearing yaw load, as well as the fatigue load for the tower longitudinal bending is observed.
The tower shadow effect is seen to increase the flapwise blade root fatigue loads by 5% for the downwind configuration and by 4% for the downwind configuration without prebend. The flapwise fatigue load increase agrees with predictions in literature by for example Zahle et al. (2009) or Glasgow et al. (1981).
A lower edgewise damping is observed when the upwind configuration is changed into a downwind configuration. With the reduced edgewise damping the edgewise extreme loads are increased by 5% for the downwind configuration and 8% of the downwind configuration without prebend. The lower edgewise damping also contirbutes to the edgewise blade root fatigue load increase and a total increase of 7% for the downwind configuration and 11% for the downwind configuration without prebend is observed.
As observed also by Ning and Petch (2016), the gravity moment of rotor-nacelle assembly increases the bending loads in the tower bottom flange. Due to the gravity moment of the rotor-nacelle assembly an increase in the extreme tower bottom bending moment of 14% for the downwind configuration and 15% for the downwind configuration without prebend is observed, compared to the upwind configuration.
The interaction of several effects result into a small AEP loss of 0.75% in the downwind configuration. As the blades deflect in the coning direction under loading the rotor area in the downwind configurations is smaller than in the upwind configuration. The tower shadow effect also contributes to the AEP loss. The tilt angle on the other hand compensates for some of the losses as the rotor is closer to be perpendicular aligned with the wind direction in the downwind configurations than in the upwind configuration. The AEP loss increases to 1.66% if the prebend of the blade is neglected. A general increase in AEP due to the alignment of tilt and inclination angle, as observed by Yoshida (2006), could not be confirmed, since the inclination angles are not as large as observed by Yoshida et al..
Power fluctuations are seen to be influenced by the interaction of the tilt, the tower shadow effect and the lower edgewise damping. While the tilt angle is beneficially reducing the inflow variations the tower shadow increases the inflow variation. The lower edgewise damping increases power fluctuations further and as as result the power fluctuations of the downwind configurations are higher than the fluctuations of the upwind configurations.

4.5 Discussion

In this study a downwind configuration is assembled from the S111 2.1MW turbine to see potential benefits in a configuration change from a load- and AEP-perspective. It has been seen that the downwind configuration in the current simulation set-up benefits from the tilt angle that counteracts the inclination angle. Since the IEC-standard is a guideline for the design of upwind configurations, the inclination angle is a conservative property of the inflow conditions. Thus, using the same inclination angle for the downwind configuration is not a fair comparison of the configurations. When comparing the concepts, the angle should either be inverted for the downwind configuration or both configurations should be subject to a flow field without inclination angle. The change in the inclination angle consequentially leads to a higher power difference between the configurations as well as an increase in fatigue loads in the downwind configuration and a decrease in fatigue loads in the upwind configuration.
The observed increase in blade fatigue loads for the downwind configurations means that the tower shadow model is crucial for the evaluation of the downwind configuration. The used model considers the deficit of the free wind speed behind the tower, but the increased turbulence is not modelled. More investigations need to be done to evaluate if this effect is relevant for the load fluctuations. A tower shadow validation will be needed to evaluate different tower shadow alleviation techniques, which would be required to reduce the loads to the level of the upwind configuration.
A significant increase in edgewise extreme and fatigue blade loads is observed due to a lower edgewise damping in the downwind configurations. It cannot yet be concluded if the lower edgewise damping is a general property of downwind configurations. Future work has to investigate the difference in the modal dynamics between upwind and downwind configurations, as this determines the dynamic stability of the turbine and is a relevant cause for differences in loads. A better understanding of the edgewise damping is needed to be able increase the damping if possible, to avoid high loads and instabilities.
The choice of the controller significantly influences the loads due to load cases where certain situations are handled. This means that loads could differ significantly with different handling routines of for example, turbine shut down or operation at high yaw errors. In this case extreme tower bending or flapwise blade root moment could be reduced in all three configurations with for example the proprietary controller. If this would change the difference between the upwind and the downwind configuration is unclear. Situation determined by normal operation including turbulence would not be improved. Thus, no improvements can be expected for the tower clearance or the edgewise loads. Also AEP losses

would not be compensated with the proprietary controller since they are related to operation below rated power.
Seen from the perspective of blade design, it could be possible to reduce blade material and blade cost for the chosen geometry assembly when changing the upwind into a downwind configuration. Firstly, because the tower clearance is increased, secondly because the extreme flapwise blade load is decreased significantly. These two advantages might overcome the increase in extreme edgewise blade loads.
However, from the full turbine perspective it is doubted that a pure material reduction of the blades is beneficial. To exploit the full potential of the downwind configuration, the LCOE should be considered. The LCOE can be expected to increase with the configuration change, since the tower is a major cost component and the load has significantly increased when the upwind configuration is changed into a downwind configuration. Further, the downwind configurations showed a lower AEP, increasing the LCOE compared to the upwind configuration. Consequentially, if a cost competitive downwind turbine should be designed, the blade moulds could not be kept. Instead a new rotor should be designed while the load envelope is kept the same as in the upwind configuration.
With this approach the rotor diameter could be increased to harvest more energy. The increase of rotor diameter would be limited by the flapwise blade root moment. If tower clearance becomes a design constraint for a larger rotor diameter, the cut-out wind speed could be reconsidered, since the the contribution to the AEP is relatively low. To avoid a significant increase in the tower cost the static loading the downwind configuration should be modified, such that the center of gravity of the rotor-nacelle assembly is located closer to the tower center. In that case, the gravity moment would decrease. Since the static moment of the downwind configurations can never have a contribution reducing the extreme tower bottom bending moment, as it does in the upwind configuration, the thrust level for the downwind configuration would have to be reduced significantly. In that case the tower cost could potentially reach a tower cost level of the upwind configuration. From a limited thrust level a further reduction in the extreme flapwise bending moment could be expected, potentially allowing further rotor diameter increase. In order to fairly evaluate if such drastic changes in design strategy are beneficial for a downwind configuration, the upwind configuration would also need to be redesigned. A limited thrust level would be expected to be also beneficial for an upwind configuration. Only in that case a fair comparison could be made and it could be evaluated if the LCOE of a downwind configuration is lower than the LCOE of an upwind configuration.
Overall it can be concluded that there is no clear benefit of changing an existing upwind configuration into a downwind configuration. To see the benefits a redesign of both configurations would be required to evaluate the benefit in

LCOE.

Funding Information

This Project is an industrial PhD project founded by the Innovation Fund Denmark (case number 5189-00180B) and Suzlons Blade Science Center.

Bibliography

Corrigan, R. and Viterna, L. (1982). free yaw performance of the mod-0 large horizontal axis 100kw wind turbine. *NASA-Report*, TM-83(19235):103–122.

Glasgow, J. and Corrigan, R. (1983). Results of free yaw test of the mod-0 100-kilowatt wind turbine. *NASA Report*, TM-83432:1–16.

Glasgow, J., Miller, D., and Corrigan, R. (1981). Comparison of upwind and downwind rotor operations of the doe/nasa l00-kw mod-0 wind turbine. *NASA Report*, TM-8744:225–234.

Hansen, M. (2004). Aeroelastic stability analysis of wind turbines using an eigenvalue approach. *Wind Energy*, 7:113–143. https://doi.org/10.1002/we.116.

Hansen, M. and Henriksen, L. (2013). Basic dtu wind energy controller. *DTU-Wind-Energy-Report*, E-0028.

Hansen, M., Thomsen, K., Natarajan, A., and Barlas, A. (2015). Design load basis for onshore turbines revision 00. *DTU Report; DTU Wind Energy*, E-0074.

IEC (2014). Iec 61400-1 ed.3 wind turbines- part1: Design requirements. Technical report, International Electronical Commission.

Kiyoki, S., Sakamoto, K., Inamura, S., Tobinaga, I., Saeki, M., and Yokoyama, K. (2016). Development of 5-mw downwind turbine and floating substation facility for offshore wind power. *Hitatichi Review*, 65(4):938–943. http://www.hitachi.com/rev/pdf/2016/r2016_04_all.pdf. Accessed: April 26, 2018.

Kress, C., Chokani, N., Abhari, R., Hashimoto, T., Watanabe, M., Sano, T., and Saeki, M. (2016). Impact of flow inclination on downwind turbine loads and power. *Journal of Physics: Conference Series 753: The Science of*

Making Troque from Wind (TORQUE2016). https://doi.org/10.1088/1742-6596/753/2/022011.

Larsen, T. and Hansen, A. (2014). How 2 hawc2, the user's manual. *Risø-Report:Risø-Report*, R1597(verion 4-5):1–147.

Madsen, H. A., Riziotis, V., Zahle, F., Hansen, M. O. L., Snel, H., Grasso, F., Larsen, T. J., Politis, E., and Rasmussen, F. (2011). Blade element momentum modelling of inflow with shear in comparison with advanced model results. *Wind Energy; Vol. 15; p. 63-81*. https://doi.org/10.1002/we.493.

Ning, A. and Petch, D. (2016). Integrated design of downwind land-based wind turbines using analytic gradients. *Wind Energy*, 19:2137–2152. https://doi.org/10.1002/we.1972.

Reiso, M. and Muskulus, M. (2013). The simultaneous effect of a fairing tower and increased blade flexibility on a downwind mounted rotor. *Journal of Renewable and Sustainable Energy*, 5(3):033106–1–1033106–11. https://doi.org/10.1063/1.4803749.

Yoshida, S. (2006). Performance of downwind turbines in complex terrains. *Wind Engineering*, 30(6):487–502.

Zahle, F., Madsen, H., and Sørensen, N. (2009). Evaluation of tower shadow effects on various wind turbine concepts. *Research in Aeroelasticity DTU Report EFP-2007-II*, 1698:1–147.

Chapter 5

Differences in damping of edgewise whirl modes; operating an upwind turbine in a downwind configuration

---

The following will present the manuscript submitted to "Wind Energy Science" for the investigations of difference in edgewise damping of a downwind configuration compared to the upwind configuration, formatted for the thesis format.

Wanke, G., Bergami, L., and Verelst, D. R.: **Differences in damping of edgewise whirl modes operating an upwind turbine in a downwind configuration**, Wind Energ. Sci. Discuss., https://doi.org/10.5194/wes-2019-88, in review, 2019
The manuscript is accessible for public review process under
https://www.wind-energ-sci-discuss.net/wes-2019-88/

Manuscript received: 02 Dec 2019

Differences in damping of edgewise whirl modes operating an upwind turbine in a downwind configuration

Gesine Wanke[1], L. Bergami[1], D. R. Verelst[2], D. R. Verelst[2]

[1] Blade Science Center Suzlon, Vejle Denmark
[2] DTU Wind Energy, Technical University of Denmark, Roskilde, Denmark

Correspondence: Gesine Wanke, Suzlon Blade Science Center, Havneparken 1, 7100 Vejle, Denmark. E-mail: gesine.wanke@suzlon.com

Abstract

The qualitative changes in damping of the first edgewise modes when an upwind wind turbine is converted into the respective downwind configuration are investigated. A model of a Suzlon S111 2.1MW turbine is used to show that the interaction of tower torsion and the rotor modes is the main reason for the change in edgewise damping. For the foreward whirl mode a maximum decrease in edgewise damping of 39% is observed and for the backward whirl mode a maximum increase of 18% in edgewise damping is observed when the upwind configuration is changed into the downwind configuration. The shaft length is shown to be influencing the interaction between tower torsion and rotor modes as out-of-plane displacements can be increased or decreased with increasing shaft length due to the phase difference between rotor and tower motion. Modifying the tower torsional stiffness is seen to give the opportunity in the downwind configuration to account for both, a favorable placements of the edgewise frequency relative to the second yaw frequency, as well as a favorable phasing in the mode shapes.

5.1 Introduction

Upwind wind turbines, where the rotor is placed in front of the tower relative to the wind, have been in the focus of research efforts for the recent years. As wind turbines increase in size, and cost of energy has to be reduced, rotor blades become longer and increase in flexibility. The blade tip to tower clearance is a

constraint for the design of such blades. Downwind rotors, where the rotor is placed behind the tower are not subject to such constraint during normal operation and re-experience therefore an increase in research effort.
The downwind concepts are known to show a higher fatigue load for the flapwise blade root moments compared to the upwind concepts due to the tower shadow effect. Glasgow et al. (1981) measured a significant fatigue load increase in the flapwise bending loads for a downwind configuration compared to an upwind configuration of a 100kW machine due to the velocity deficit of a truss tower. Zahle et al. (2009) simulated a reduction in normal force on the blade of 20%, due to the rapid fluctuation in the angle of attack as the blade passes through the tower wake. A fatigue load increase of around 20% for the damage equivalent flapwise blade root bending moment was found by Reiso and Muskulus (2013), when comparing the 5MW NREL reference turbine in a downwind configuration to the original upwind configuration.
A comparison of a full design load basis for a commercial Suzlon class IIIA 2.1MW wind turbine in an upwind configuration and a downwind configuration by Wanke et al. (2019) showed, that also the edgewise fatigue load increases significantly, when changing the upwind configuration into a downwind configuration. Only 30% of the fatigue load increase for the edgewise blade root sensor could be associated with the tower shadow effect. The remaining fatigue load increase could be associated with a lower edgewise damping in the foreward whirl mode of the downwind configuration.
In the 1990s first research efforts were made to characterize the damping of the edgewise blade modes since some stall regulated turbines showed stall induced vibrations. Petersen et al. (1998a) described how the local edgewise vibrations coupled to the substructure in global foreward (FW) and backward (BW) whirling modes. The whirling modes resulted into a force at the hub center, rotating either with the rotational direction of the shaft (FW) or against the rotational direction of the shaft (BW). Energy was seen to be exchanged between the blade and rotor modes if the frequencies were placed close together. Lower damping of the modes was shown to lead to a significant increase in both fatigue and extreme loads as vibration amplitudes are higher.
In the 'STALLVIB'-project Petersen et al. (1998b) aimed to predict margins of damping, identify important parameter influencing the edgewise damping and to establish design guidelines to prevent the occurrence of stall induced vibrations. It was seen that the aerodynamic damping determined if stall induced vibrations would occur. Out-of plane motion could generally be associated with higher aerodynamic damping. Airfoil characteristics such as the stall behaviour and the slope of the lift curve over the angle of attack were found to determine if the aerodynamic force created from the vibration velocity restored the steady state position.

Thomsen et al. (2000) used a rotating mass on the nacelle to excite the edgewise whirling modes for a 600kW upwind turbine. From the measured blade root moment the damping for the edgewise whirling modes was calculated. The results showed that the edgewise foreward whirling mode was significantly higher damped than the corresponding backward whirling mode.
Hansen (2003) build a linearized model with 15 degrees of freedom to determine the damping for the edgewise modes of the turbine, measured by Thomsen et al. (2000), using an eigenvalue approach. Hansen could confirm that the edgewise foreward whirl mode was significantly higher damped than the edgewise backward whirl mode. From the visualization of the modal amplitudes it could be shown that the edgewise foreward whirl mode had a significant higher out-of-plane component than the backward whirl mode, contributing positively to the damping. The work recommended that the over all edgewise damping could be significantly increased, if the turbine design was able to place the edgewise blade frequency between the 2nd yaw and tilt frequency of the turbine, as this increased the out-of plane contribution of the edgewise foreward whirl mode.
In the description of aeroelastic instabilities Hansen (2007) derived the aerodynamic damping coefficient of a single airfoil in dependency on the vibration direction. From the simplified analysis he was able to show how the aerodynamic damping relates to the inflow velocity, the airfoil coefficients and the airfoil coefficient slopes over the angle of attack for different quadrants of vibration direction.
This paper will focus on the difference in edgewise damping when the Suzlon S111 2.1MW wind turbine is changed from an upwind configuration into a downwind configuration. The damping of the edgewise whirl modes will be estimated from timeseries for the two turbine configurations and different sets of flexibility in the components. Finally, shaft length, cone angle and tower torsion are varied to show how the edgewise damping could be influenced by the turbine design.
The interaction of the rotor and the tower torsion will be shown to cause differences in the maximum damping between the two edgewise whirl modes and the two turbine configurations. The interaction of the edgewise foreward whirl mode and the tower torsion increases the edgewise damping in the upwind configuration and decreases the edgewise damping in the downwind configuration. In the foreward whirl mode the edgewise damping decreases by 39% when the S111 Suzlon turbine is changed from the upwind configuration into a downwind turbine. In the backward whirl mode the damping increases 18% when the S111 Suzlon turbine is changed from an upwind configuration into a downwind configuration. Differences in out-of-plane displacements cause the main difference in damping between the two turbine configurations and the two modes. As the eigenfrequency of the edgewise foreward whirl mode is closer to the second yaw frequency the foreward whirl mode will show a higher difference in damping between the configurations. The difference in damping of the foreward whirl mode

dominates therefore the over all change in damping when the upwind configuration is changed into the downwind configuration, as well as the difference in extreme and fatigue loads.

5.2 Methods

In this study two different attempts are used to investigate the difference in edgewise damping between an upwind configuration and a downwind configuration. Firstly, the edgewise damping of the full turbine is calculated from HAWC2 timeseries for upwind and downwind configuration with the full turbine flexibility, called the fully flexible (FF) configurations. Further the edgewise damping is estimated for turbine configurations with reduced flexibility. The flexibility is reduced by increasing the stiffness of certain turbine components significantly. The turbine flexibility is reduced to the rotor flexibility and tower torsional flexibility, as this configuration resembles the difference in edgewise damping with the minimum degrees of freedom. The configurations with reduced flexibility are called the upwind RTT (rotor and tower torsion) and the downwind RTT configuration. Secondly, the influence of shaft length, cone angle and tower torsional stiffness on the edgewise damping of the upwind RTT and downwind RTT configuration are studied by parametric variation. the influence of the shaft length is investigated in a range of -30% and +100%, the cone angle, coning away from the tower from 0° to 7.5°, and the tower torsional stiffness in a range of ± 80%. Table 5.1 shows a summary of all the configurations used in the study and the investigated parameter variation.

The study is based on a Suzlon S111 2.1MW, class IIIA turbine with a rotor diameter of 112m and 90m tubular tower height. The turbine is pitch regulated and operating at variable rotor speed below rated power. The operational range is from 4ms^{-1} to 21ms^{-1} and rated wind speed is 9.5ms^{-1}. Blade prebend and shaft tilt are neglected in the study to reduce coupling terms between in-plane and out-of plane modes. The cone angle is neglected other than for the parameter study for the same reason. The turbine is assembled as a downwind configuration by shifting the rotor behind the tower and yawing the shaft by 180°.

5.2.1 Damping estimation from timeseries

The damping of the turbine edgewise modes is estimated from HAWC2 (Madsen et al. (2019) (Version 12.7)) timeseries. Alternatively, HAWCStab2 (Hansen

Table 5.1: Configurations and parameter variations

configuration/ parameter variation	properties
edgewise damping estimation	
all configurations	no tilt, no cone, no prebend simplified controller, no gravity, uniform inflow (no turbulence, no sheer, no veer, no inclination angle)
upwind FF	upwind, all degrees of freedom (fully flexible)
downwind FF	downwind, all degrees of freedom (fully flexible)
upwind RTT	upwind, rotor flexibility, tower torsion flexibility
downwind RTT	downwind, rotor flexibility tower torsion flexibility
parameter variation	
shaft length	up- and downwind RTT configuration shaft length variation: -30% to +100%
cone angle	up- and downwind RTT configuration cone angle variation: 0° to 7.5° (away from tower)
tower torsional stiffness	up- and downwind RTT configuration torsional stiffness factor variation ± 80%

(2004)) could be used to solve a linearised stability model around the non-linear deflected steady state. In doing so, the eigenfrequencies, damping and mode-shapes can be obtained directly by solving an eigenvalue problem of the linearised system. However, due to unresolved issues with respect to modelling downwind turbines in HAWCStab2 (which has only been used and tested in the traditional upwind context) it was considered outside the scope of this investigation to address those challenges. The turbine configurations from Tab. 5.1 are subject to a uniform wind field without turbulence, wind shear or tower shadow, to reduce the noise in the timeseries. The gravity is set to zero to avoid excitation with the rotational frequency on the edgewise signal. The controller is exchanged by a simple setting of pitch angle and rotational speed according to the wind speed at hub height to allow for a slow wind speed increase to avoid other modal frequencies than the excited frequencies in the timeseries. A long run-in time is used to assure that the steady state positions of the turbine are reached and the noise from the run-in does not disturb the vibration signal. The foreward and

backward edgewise whirl mode are excited with a harmonic force at the blade at around r/R=75% radius with the blade edgewise frequency. A time shift of 1/3 of the vibration period between the excitation forces on the three blades assures that either the foreward whirl mode or the backward whirl mode are excited. The foreward whirl mode is exited with the blade order 3-2-1, as the blades are named in the tower passing order seen from the front. The backward whirl mode is excited with the blade excitation order 1-2-3. After the excitation has stopped, 10 seconds of the timeseries signal are neglected and 50 seconds are used for estimation of damping of the edgewise modes. It has been tested with the aeroelastic modal analysis tool HAWCStab2 (Hansen (2004)) that the trends over wind speed as well as trends for the difference of damping between the configurations are captured correctly for investigations of qualitative differences.
For a primary damping estimation the damping coefficient for a single airfoil as described by Hansen (2007) is calculated. The damping coefficient is calculated from simulated steady state values of the airfoil coefficients and angle of attack at 9m/s, -3° pitch angle and r/R=75% rotor radius.
From the timeseries the logarithmic damping decrement of the edgewise modes is extracted. For the estimation of damping the decaying displacement signal of the 3 blades at r/R=75% radius is used. The logarithmic damping decrement δ is calculated via

$$\delta = \frac{1}{N} ln \frac{x\left(t\right)}{x\left(t+NT\right)} \tag{5.1}$$

where N is the number of positive successive peaks, $x(t)$ is the edgewise displacement amplitude of the first peak and $x\left(t+NT\right)$ is the amplitude of the Nth peak at N vibration periods T after the first peak. The logarithmic damping decrement is converted to the damping ratio ζ

$$\zeta = \frac{1}{\sqrt{1+\left(\frac{2\pi}{\delta}\right)^2}} \tag{5.2}$$

The damping ratio is estimated from simulations for the backward and foreward whirling mode of the fully flexible (FF) configurations as well as the upwind RTT and the downwind RTT configuration over the range of operational wind speeds.

5.2.2 Coleman transformed timeseries

By transforming the velocities and displacements to multiblade- or coleman-coordinates (Bir (2008)) the difference in damping for the timeseries at $9\mathrm{ms}^{-1}$ can be further investigated. For the r/R=75% airfoil section of the upwind RTT and

downwind RTT configuration the velocities and displacements are transformed to coleman-coordinates such that the components due to the blade self-motion as well as the motion of the substructure can be considered. The later is the motion of the non-deflected blade due to the tower torsion.
The modal displacement and modal velocities of the r/R=75% rotor position in the coleman coordinates have been calculated via fft-analysis in Matlab. In order to keep a global reference phase for all signals between the different fft-calculations the fft-analysis is once done on the original signal and once on the signal where the azimuth position with a factor of 1/1000 is added. From the comparison of the phase of the original signal and the phase of the signal including the azimuth position all signals can be referenced to the phase of the global azimuth position. This guaranties, that the phasing between the substructure and the rotor modes are consistent between several fft-calculations.

5.3 Results

The result section presents the estimated edgewise damping as a function of wind speed for the fully flexible up-and downwind FF configuration as well as the up- and downwind RTT configuration. Further the out-of-plane displacement of the edgewise modes is shown to be the reason for the difference in damping. Finally the damping for the parameter variation for shaft length, cone angle and tower torsional stiffness is presented.

5.3.1 Edgewise damping over wind speed estimated from timeseries

Figure 5.1 shows the estimated normalized damping ratio as a function of wind speed for the backward (Fig. 5.1 (a)) and foreward whirl mode (Fig. 5.1 (b)) for the fully flexible up- and downwind FF configuration, as well as the upwind RTT and downwind RTT configuration. The figure further shows the difference in damping between the upwind configuration RTT and the other configurations (Fig. 5.1 (c) and (d)).

The figure shows that both edgewise modes in both configurations are positively damped. The damping ratio increases from cut-in wind speed to a local maximum at rated wind speed. After decreasing for wind speeds between rated wind speed and wind speeds around 14ms^{-1}, a damping increase for wind speeds higher than

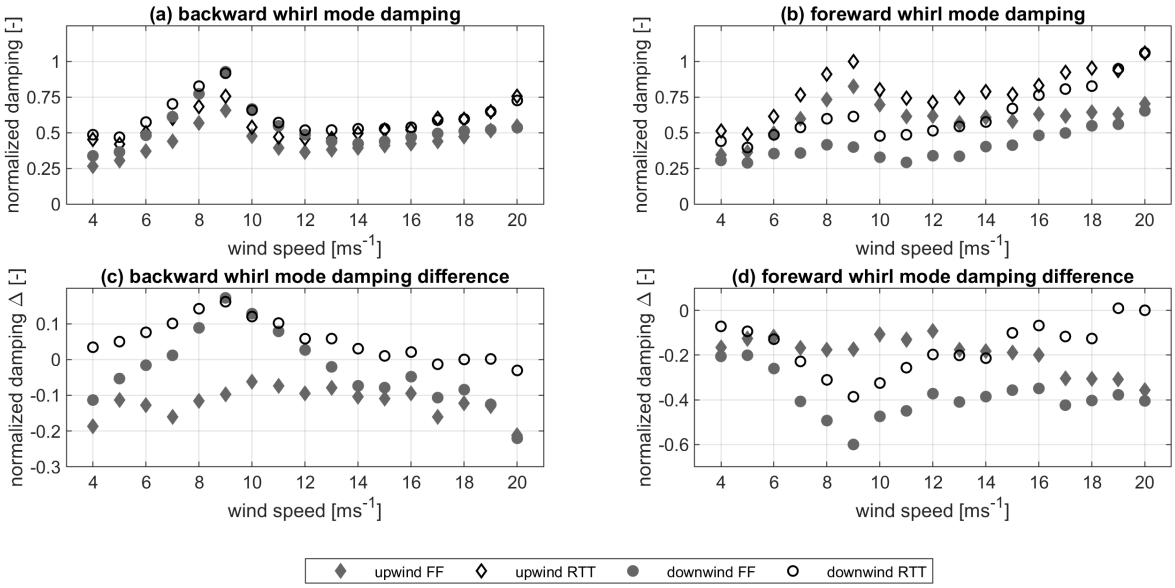

Figure 5.1: Normalized damping ratio as function of wind speed for the back whirl mode (a) and the foreward whirl mode (b) for the upwind RTT and the downwind RTT configuration and the fully flexible FF configurations, as well as the difference in damping to the damping to the upwind RTT configuration in the backward whirl mode (c) and the foreward whirl mode (d). The damping as well as the damping difference are normalized with the damping of the upwind RTT configuration at 9 ms^{-1} of the foreward whirl mode.

$14ms^{-1}$ is observed. In the backward whirl mode (Fig. 5.1 (a)) the downwind configurations are subject to higher edgewise damping than the respective upwind configurations. The difference is approximately 18% for the RTT configurations (see Fig. 5.1 (c)). In the foreward whirling mode (Fig. 5.1 (b)) the two downwind configurations are subject to significantly lower edgewise damping than the respective upwind configurations over the investigated wind speed range. The difference in edgewise damping is largest around rated wind speed, where the damping is approximately 39% lower in the downwind RTT configuration than the upwind RTT configuration (Fig. 5.1 (d)).
For the upwind configurations the foreward whirl mode (Fig. 5.1 (b)) is significantly higher damped than the backward whirl mode (Fig. 5.1 (a)), as also

shown by Hansen (2003), since the foreward whirl mode has a higher out-of-plane component of the mode shape than the backward whirl mode. When the tower flexibility is removed from the model or when the aerodynamic forces are not present, the damping of both foreward and backward modes are identical. This indicates that the difference in damping is driven by the interaction of the aerodynamic forces on the rotor with the tower torsional motion.

5.3.2 Modal displacement effects on edgewise damping

The observed difference in normalized edgewise damping between the upwind and the downwind configuration presented in Fig. 5.1 can not be explained with the analytical airfoil in-plane damping coefficient derived by Hansen (2007). There is no difference in the coefficient, since the steady state values of the airfoil coefficients and the according slopes are the same. Further no difference in the in-plane velocities could be found. Thus, the difference in edgewise damping has to be explained by the out-of-plane displacements in the modes for the different turbine configurations. The out-of-plane components can be either due to the flap component in the edgewise modes, or due to the tower torsion that rotates the blades out of the reference plane. This section shows

- higher out-of-plane displacement gives higher edgewise damping
- difference in forcing due to configuration gives difference in modal phases
- difference in modal phases gives difference in damping

Figure 5.2 shows the out-of-plane displacements of the sine and cosine components of the rotor, as well as the sine displacement component due to the substructure, e.g. the tower torsion, for the backward whirl mode (Fig. 5.2 (a) and (c)) and the foreward whirl mode (Fig. 5.2 (b) and (d)) of the upwind RTT and the downwind RTT configuration.

The figure shows that there generally is a phase shift between the sine component of the out-of plane displacement between the substructure and the rotor. Adding the two signals leads to the total sine component of the out-of plane displacement with the same frequency, but a different amplitude and phase. Only in the foreward whirl mode of the downwind RTT configuration, which is also the mode with the over all lowest damping, the total out-of-plane displacement is reduced

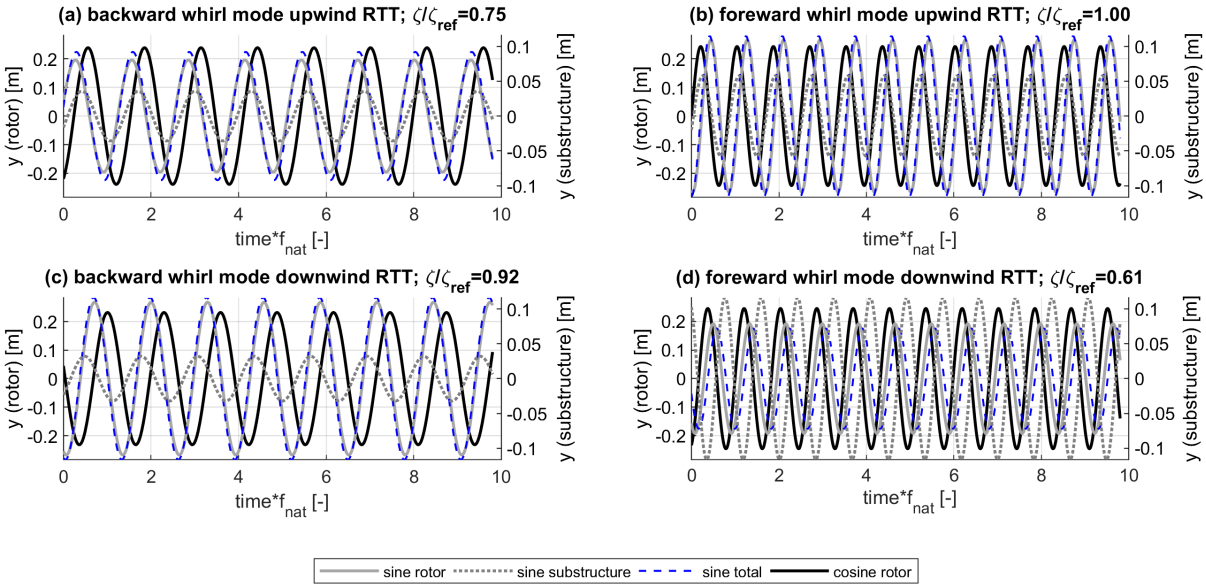

Figure 5.2: Modal out-of-plane displacements at 9ms^{-1} for the backward whirl mode ((a), (c)) and foreward whirl mode ((b), (d)) of the upwind RTT ((a), (b)) and downwind RTT configuration ((c), (d)). The time axis is normalized with the blade edgewise natural frequency.

due to the tower torsional displacement (Fig. 5.2 (d)). Generally, the main contribution to the out-of-plane displacement is due to the rotor self-motion. The foreward whirl mode (Fig. 5.2 (b) and (d)) shows generally higher out-of-plane displacements of to the substructure than the respective backward whirl mode (Fig. 5.2 (a) and (c)), as the natural frequency of the foreward whirl mode is closer to the natural frequency of the second yaw mode. The natural frequencies of the modes are the same for the upwind and the downwind configuration.
The interaction of the rotor and the tower causing a higher sine out-of-plane displacement of the rotor leading to higher damping in the foreward whirl mode of the upwind RTT configuration (5.2 (b)) and the backward whirl mode in the downwind RTT configuration (5.2 (c)) than respective modes with lower sine out-of-plane displacements. The foreward whirl mode of the upwind RTT configuration (5.2 (b)) further shows a 5% higher out-of-plane cosine component of rotor displacement than the downwind RTT configuration in the backward whirl mode (5.2 (c)), which explains the remaining difference in damping between the

two turbine configurations.
The higher sine component of the rotor out-of-plane displacement can not be associated with the frequency of the second yaw mode, as this does not hold true for the backward whirl mode of the downwind configuration (Fig. 5.2 (c)). The higher out-of-plane rotor displacement in the sine component is observed to come with a sine component of the substructure out-of-plane displacement that is lagging the respective rotor displacement (Fig. 5.2 (b) and (c)). If the sine component of the of the out-of-plane displacement of the substructure is leading the respective rotor displacement the sine component of the out-of-plane rotor displacement is lower (Fig. 5.2 (a) and (d)).
Also the in-plane motion of the rotor (not shown here) is subject to a sine component lagging the cosine component in the backward whirl mode and a sine component leading the cosine component in the foreward whirl mode. The modal velocities cause aerodynamic forces. Inherently to the whirl modes the aerodynamic in-plane forces at the hub sum up to a non-zero total in-plane force. With the arm of the shaft length this force causes a yaw loading. Depending on the placement of the rotor relative to the yaw center a positive in-plane cosine force at the hub causes a positive yaw loading (upwind configuration) or a negative yaw loading (downwind configuration). The response of the tower, e.g. the out-of-plane substructure sine component of displacement is therefore either lagging the the out-of-plane sine component of the rotor displacement, as in the foreward whirl mode of the upwind RTT configuration (5.2 (b)) and the backward whirl mode of the downwind RTT configuration (5.2 (c)) or the sine component of the substructure out-of-plane displacement is leading the rotor sine out-of-plane displacement (upwind RTT configuration, backward whirl mode, Fig. 5.2 (a) and downwind RTT configuration, foreward whirl mode, Fig. 5.2 (d)).
Form this analysis it can be seen that the difference in edgewise damping is due to a difference in out-of-plane motion. The main contributor is the higher rotor out-of-plane motion associated with a favorable phasing between the out-of-plane motion of the substructure and the out-of-plane sine component of the rotor motion. It will therefore be expected from the analysis described in the previous paragraphs, that the edgewise damping can be increased by an increase of the yaw loading, if the substructure displacement is lagging the sine out-of-plane displacement of the rotor. The damping is on the other hand expected to decrease with an increased yaw loading if the substructure displacement is leading the sine out-of-plane displacement of the rotor. Increasing the shaft length is expected to increase the damping of the edgewise foreward whirl mode in the upwind configuration as well as in the backward whirl mode of the downwind configuration. In the backward whirl mode of the upwind configuration and the foreward whirl mode of the downwind configuration an increase in shaft length is expected to decrease the edgewise damping.

5.3.3 Parameter variation: shaft length

Figure 5.3 shows the normalized edgewise damping values of the backward whirl mode (Fig. 5.3 (a) and (c)) and foreward whirl mode (Fig. 5.3 (b) and (d)) for the upwind RTT configuration (Fig. 5.3 (a) and (b)) and the downwind RTT configuration (Fig. 5.3 (c) and (d)) as a function of wind speed and shaft length factor.

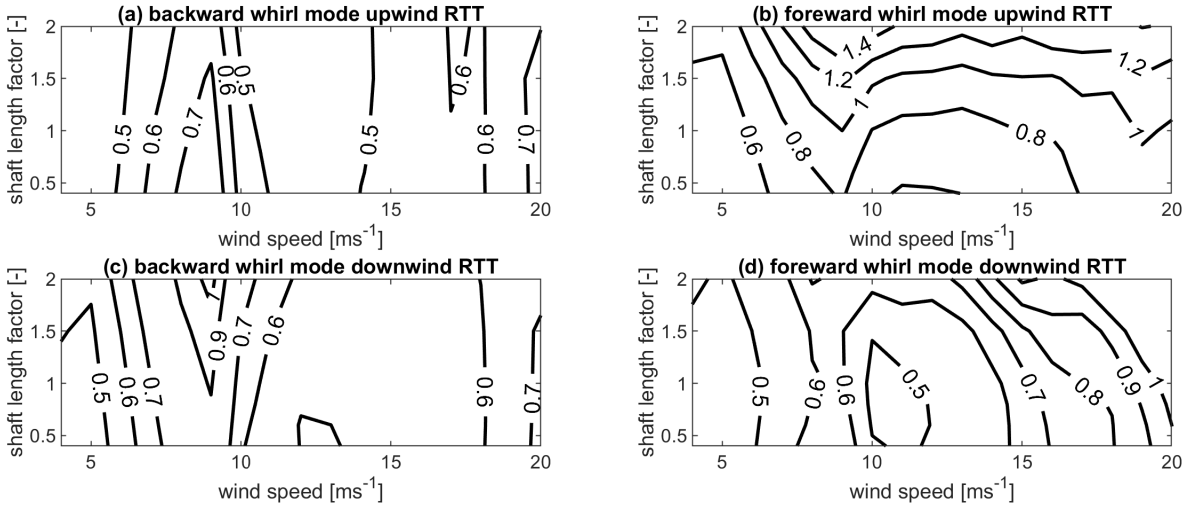

Figure 5.3: Normalized edgewise damping ratio as a function of wind speeds and shaft length factor for the backward whirl mode ((a) and (c)) and the foreward whirl mode ((b) and (d)), for the upwind RTT configuration ((a) and (b)) and the downwind RTT configuration ((c) and (d)). The edgewise damping is normalized with the damping value of foreward whirl mode in the upwind RTT configuration at a shaft length factor of 1 at 9ms^{-1}.

The figure shows that the normalized edgewise damping of the backward whirling mode in the upwind RTT configuration decreases with the increasing shaft length (Fig. 5.3 (a)). In the downwind RTT configuration on the other hand the normalized edgewise damping increases with the increasing shaft length in the backward whirl mode (Fig. 5.3 (c)). The effect is strongest pronounced around rated wind speed. In the foreward whirl mode of the upwind RTT configuration the normalized edgewise damping increases with the increasing shaft length (Fig. 5.3 (b)).

The normalized edgewise damping of the downwind RTT configuration on the other hand hardly changes with the increasing shaft length for wind speeds close to rated wind speed (Fig. 5.3 (d)).
For a shaft length factor of 2 and at 9ms^{-1} the out-of-plane displacements (see appendix Fig. 5.6) have been compared to the displacements for a shaft length factor of 1 at 9ms^{-1} (Fig. 5.2). Both turbine configurations in the backward whirl mode and also the upwind RTT configuration in the foreward whirl mode show the expected dependency on the shaft length according to Sect. 5.3.2 around rated wind speed: the normalized edgewise damping of the backward whirl mode of the downwind RTT configuration and the normalized edgewise damping of the foreward whirl mode in the upwind RTT configuration are increasing due to higher out-of-plane displacements in the rotor sine components. In the backward whirl mode of the upwind RTT configuration a decrease of the sine component of the out-of-plane rotor displacements can be observed. Also for the downwind RTT configuration in the foreward whirl mode the expected decrease of out-of-plane sine component of rotor displacement can be observed. However, an increase of the cosine out-of-plane displacements of the rotor can also be seen. The combination of the out-of-plane displacements leads to the effect that hardly any difference in edgewise damping can be observed at around rated wind speed for the foreward whirl mode of the downwind RTT configuration.

5.3.4 Parameter variation: cone angle

Figure 5.4 shows the normalized edgewise damping for the backward whirl mode (Fig. 5.4 (a) and (c)) and the foreward whirl mode (Fig. 5.4 (b) and (d)) in the upwind RTT (Fig. 5.4 (a) and (b)) and the downwind RTT configuration (Fig. 5.4 (c) and (d)) as a function of cone angle and wind speed.

The figure shows that the edgewise damping of both modes increases with increasing cone angle in the upwind RTT configuration (Fig. 5.4 (a) and (b)). In the downwind RTT configuration the edgewise damping decreases with increasing cone angle for wind speeds around rated wind speed (Fig. 5.4 (c) and (d)).
Introducing the cone angle has several effects. On the one hand, the cone angle changes the steady state values of the airfoil coefficients and therefore the estimated analytical damping coefficient by Hansen (2007): The blades deflect against the coning direction in the upwind RTT configuration, while the blades deflect in the same direction as the cone direction in the downwind RTT configuration. The analytical damping coefficient of the r/R=75% airfoil at 9ms^{-1} has decreased by 33% in the upwind RTT configuration when a cone angle of 7.5° is

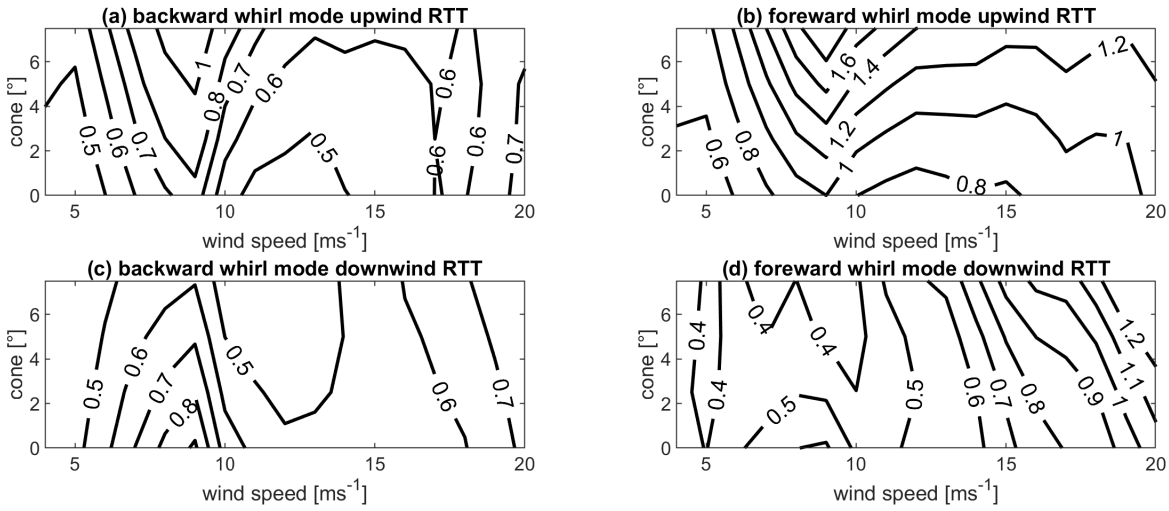

Figure 5.4: Normalized edgewise damping as a function wind speeds and cone angle for the backward whirl mode ((a) and (c)) and the foreward whirl mode ((b) and (d)), for the upwind RTT configuration ((a) and (b)) and the downwind RTT configuration ((c) and (d)). The damping is normalized with the damping value of foreward whirl mode in the upwind configuration at 0° at 9 ms^{-1}.

introduced. The analytical damping coefficient of the r/R=75% airfoil at 9ms^{-1} has increased by 38% in the downwind RTT configuration when a cone angle of 7.5° is introduced. On the other hand, the cone angle also changes the coupling between the in-plane loading and the tower torsion as the distance between the yaw axis and the outboard airfoils is increased. Comparing the displacements at 9ms^{-1} at a cone angle of 7.5° (Fig. 5.7) with the out-of-plane displacements at 9ms^{-1} without cone angle (Fig. 5.2) shows only very little changes in the rotor sine components of the out-of-plane displacements. However, the downwind RTT configuration shows a significant decrease in the cosine component of the out-of-plane rotor displacements, while the upwind RTT configuration shows a significant increase in the cosine out-of-plane rotor displacements when the cone angle of 7.5° is introduced. The changes in the cosine out-of-plane rotor displacement dominate the change in normalized edgewise damping.

5.3.5 Parameter variation: tower torsion

Figure 5.5 shows the normalized edgewise damping for the backward whirl mode (Fig. 5.5 (a) and (d)) and foreward whirl mode (Fig. 5.5 (b) and (c)) of the upwind RTT (Fig. 5.5 (a) and (b)) and downwind RTT configuration (Fig. 5.5 (c) and (d)) as a function wind speed and tower torsion stiffness factor.

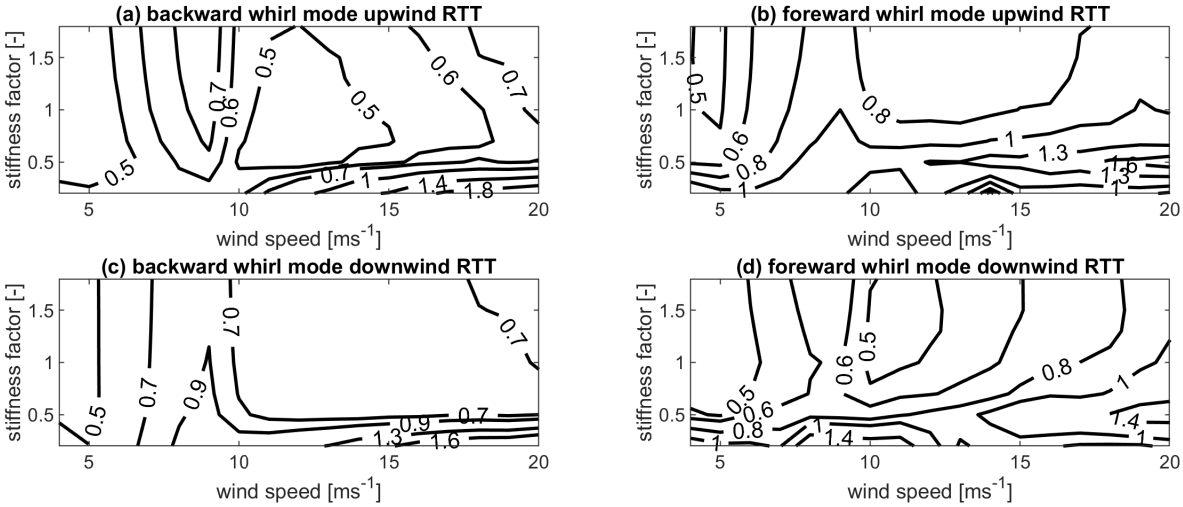

Figure 5.5: Normalized edgewise damping as a function of wind speeds and tower torsion stiffness factor for the backward whirl mode ((a) and (c)) and the foreward whirl mode ((b) and (d)), for the upwind RTT configuration ((a) and (b)) and the downwind RTT configuration ((c) and (d)). The damping is normalized with the damping value of foreward whirl mode in the upwind RTT configuration at a tower torsion stiffness factor of 1 at 9 ms^{-1}.

While the normalized edgewise damping is increasing in the backward whirl mode of the upwind RTT configuration with the increasing tower torsional stiffness (Fig. 5.5 (a)), the normalized edgewise damping of the backward whirl mode of the downwind RTT configuration (Fig. 5.5 (c)) is decreasing with increasing tower torsional stiffness at around rated wind speed. For high wind speeds and a stiffness factors lower than 0.5 the edgewise damping of the backward whirl mode increases drastically with the decreasing tower torsional stiffness for both configurations. In the foreward whirl mode the normalized edgewise damping generally

decreases in both configurations with an increasing tower torsional stiffness (Fig. 5.5 (b) and (d)). Both configurations in the foreward whirl mode show an area at around cut-out wind speeds at a stiffness factor at around 0.5, where a local maximum of normalized edgewise damping is reached.
Comparing Fig. 5.8 with Fig.5.2 shows that a decrease of tower torsional stiffness to a factor of 0.2 at 9 ms^{-1} increases generally the out-of-plane displacements associated with the substructure. Further, phasing between the substructure and rotor out-of-plane displacement as well as the rotor associated out-of-plane displacement is changing. Over all, only the upwind RTT configuration in the backward whirl mode does not benefit from the decrease in the tower torsional stiffness in the out-of-plane displacements at 9 ms^{-1}. At high wind speeds the effect of the frequency placement can be observed. As the tower torsional stiffness decreases below a factor of around 0.5 the second yaw frequency crosses the edgewise foreward whirl mode frequency and moves closer to the edgewise backward whirl mode frequency. Thus, the highest damping at high wind speeds is observed at at stiffness factor of around 0.5 for high wind speeds.

5.4 Summary

In this article the change in edgewise damping when an upwind wind turbine is converted into a downwind configuration has been investigated on the example of a simplified version of the commercial Suzlon S111 2.1MW wind turbine. The edgewise foreward whirl mode has been shown to decrease in damping as the upwind configuration is changed into the downwind configuration. The edgewise backward whirl mode on the other hand has been seen to increase in damping when the upwind configuration is changed into a downwind configuration. The interaction with the aerodynamic forces, the rotor and tower torsional motion have been shown to create a difference in out-of-plane displacement. The out-of-plane displacement was seen to cause the observed differences in edgewise damping.
The difference in the out-of plane displacements and therefore damping was shown to increase with an increased shaft length, as the yaw loading from the in-plane cosine shear forces could be increased. An increase in cone has been shown to increase cosine component of the out-of-plane rotor displacements and therefore damping for the upwind configuration, while the increase in cone causes a decrease in cosine component of the out-of-plane displacements and damping in the downwind configuration. A decrease in tower torsional stiffness has been seen to increase the damping from a favourable placement of natural frequencies relative to each other, as long as the rotor and substructure out-of-plane displacement do not counteract each other due to phase differences.

5.5 Conclusion and future work

As a decrease in damping increases extreme as well as fatigue loads, the edgewise damping should be included in the design considerations. For the shaft length there would be a trade-off between edgewise damping of the two modes, but also the rotor overhanging moment that has to be carried by the support structure. The consideration of edgewise damping would suggest a higher cone angle for upwind configurations than for downwind configurations. Again, other considerations like tower clearance, flapwise blade root loads and power production compete in the design decision. From an edgewise damping point of view downwind configurations could benefit from towers with lower torsional stiffness. Replacing a tubular tower or the bottom segments of the tubular tower by a lattice structure could significantly increase the overall edgewise damping.
The damping of the first two edgewise whirl modes has been estimated from timeseries where the foreward or backward whirl mode are excited. Using the same model as used for load simulations has the advantage of estimating directly the differences in damping without linearization effects. However, this method will only be able to estimate the damping, if clearly only one mode is excited and only one frequency dominates the spectrum. Further the damping has to be so low, that the peak to peak counting and amplitude detection can be reliably performed. In this study normalized edgewise damping above a normalized damping of 1.8 could not be estimated. This limited effectively the investigated range of the investigated parameter. The edgewise modes are well suited for this method as they are significantly lower damped than other modes. Estimating the damping from an eigenvalue solution would eliminate these limitations.
Future work should investigate further the reason for the different out-of-plane displacement in the mode shapes, especially the differences observed in the cosine components of the out-of-plane displacement. Further the degrees of freedom of the turbine model should be extended to the full flexibility, as additional degrees of freedom are expected to affect the mode shapes, especially the turbine tilting flexibility (tower fore-aft and shaft bending flexibility), or shaft bending and torsional flexibility could influence the edgewise damping.

Data availability. The data is not publicly accessible, since the research is based on a commercial turbine and the data is not available for disclosure by Suzlon.

5.6 Appendix

Out-of-plane displacements for parameter variations

The following figures show the out-of-plane displacements of the two edgewise damping modes in the two RTT configurations at 9ms^{-1} for a shaft length factor of 2 (Fig. 5.6), a cone angle of 7.5° (Fig. 5.7) and a tower torsional stiffness factor of 0.2 (Fig. 5.8).

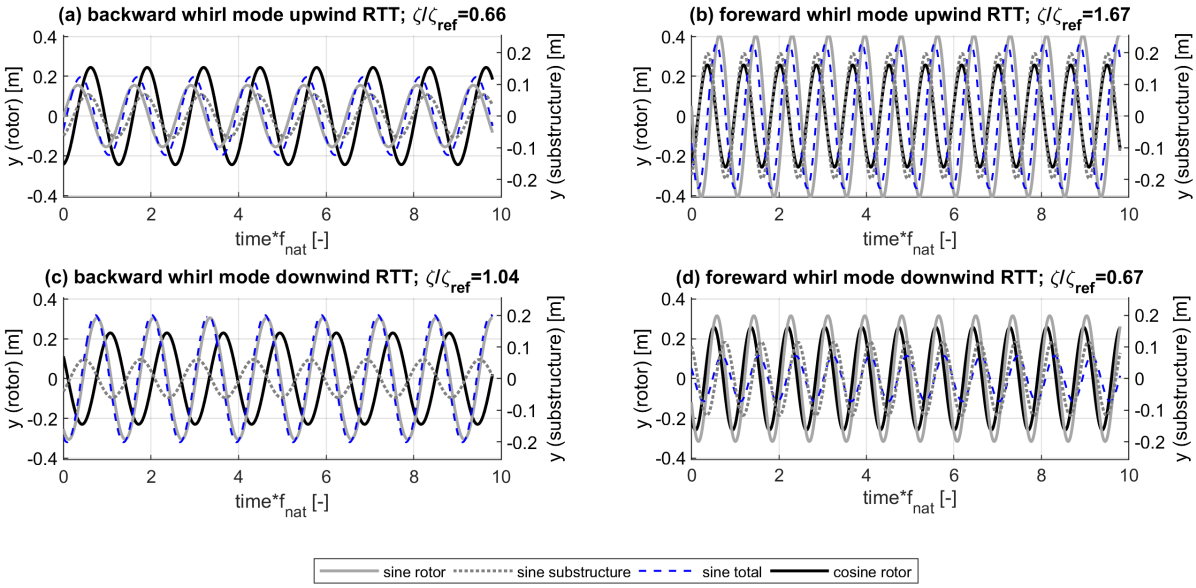

Figure 5.6: Modal out-of-plane displacements at 9ms^{-1} and a shaft length factor of 2 for the backward whirl mode and foreward whirl mode of the upwind RTT and downwind RTT configuration. The time axis is normalized with the blade edgewise natural frequency.

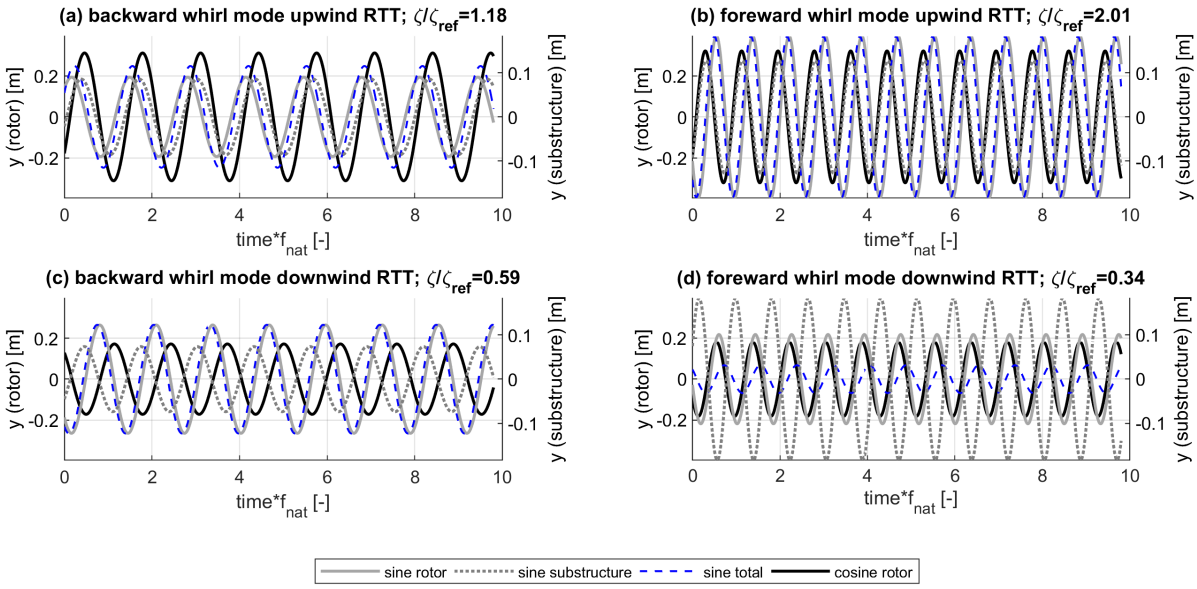

Figure 5.7: Modal out-of-plane displacements at 9ms^{-1} and a cone angle of 7.5° for the backward whirl mode and foreward whirl mode of the upwind RTT and downwind RTT configuration. The time axis is normalized with the blade edgewise natural frequency.

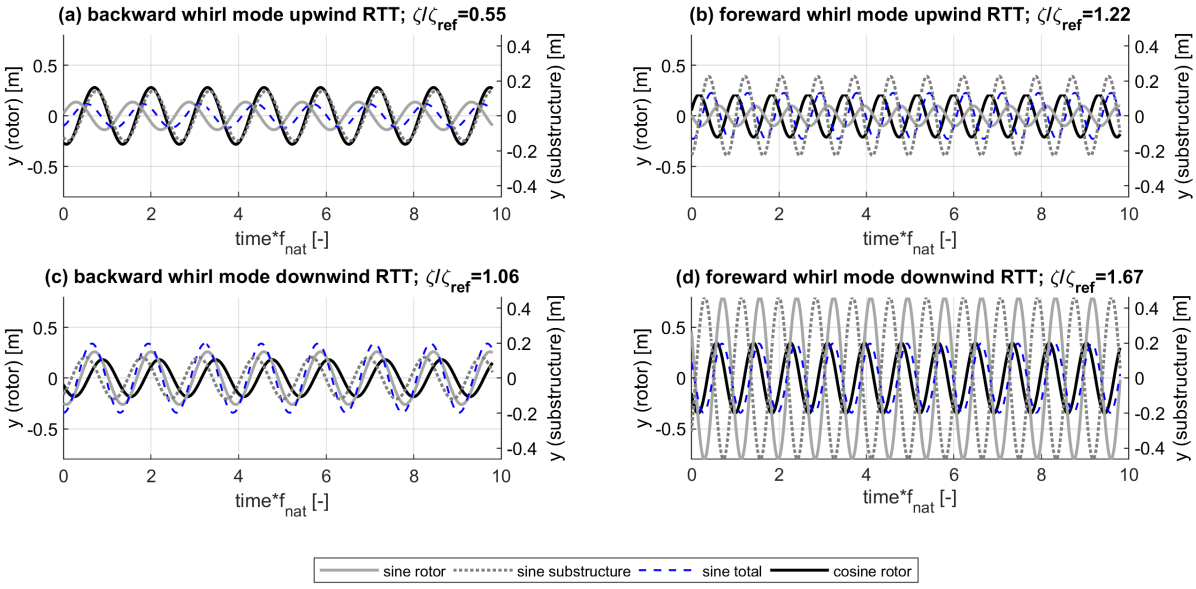

Figure 5.8: Modal out-of-plane displacements at 9ms^{-1} and a tower torsional stiffness factor of 0.2 for the backward whirl mode and foreward whirl mode of the upwind RTT and downwind RTT configuration. The time axis is normalized with the blade edgewise natural frequency.

Author Contributions. GW and LB set-up the models. GW carried out the calculations. All authors have interpreted the obtained data. GW prepared the paper with revisions of all co-authors.

Competing interests This project is an industrial PhD project funded by the Innovation Fund Denmark and Suzlons Blade Science Center. Gesine Wanke is employed at Suzlons Blade Science Center.

Bibliography

Bir, G. (2008). Multiblade coordinate transformation and its application to wind turbine analysis. *Report NREL/CP-500-42553*.

Glasgow, J., Miller, D., and Corrigan, R. (1981). Comparison of upwind and downwind rotor operations of the doe/nasa l00-kw mod-0 wind turbine. *NASA Report*, TM-8744:225–234.

Hansen, M. (2004). Aeroelastic stability analysis of wind turbines using an eigenvalue approach. *Wind Energy*, 7:113–143. https://doi.org/10.1002/we.116.

Hansen, M. H. (2003). Improved modal dynamics of wind turbines to avoid stall-induced vibrations. *Wind Energy; Vol. 6; p. 179-195.* https://doi.org/10.1002/we.79.

Hansen, M. H. (2007). Aeroelastic instability problems for wind turbines. *Wind Energy; Vol. 10; Nr. 6; p. 551-577.* https://doi.org/10.1002/we.242.

Madsen, H. A., Larsen, T. J., Pirrung, G. R., and Zahle, F. (2019). Implementation of the blade element momentum model on a polar grid and its aeroelastic load impact. *Wind Energy Science Discussion.* https://doi.org/10.5194/wes-2019-53, in review.

Petersen, J. T., Madsen, H. A., Bjoerck, H. A., Enevoldsen, P., Øye, S., Ganander, H., and Winkelaar, D. (1998a). Prediction of dynamic loads and induced vibrations in stall. *Risø-Report (Risø-R-1045(EN)).*

Petersen, J. T., Thomsen, K., and Madsen, H. A. (1998b). Local blade whirl and global rotor whirl interaction. *Risø-Report (Risø-R-1067(EN)).*

Reiso, M. and Muskulus, M. (2013). The simultaneous effect of a fairing tower and increased blade flexibility on a downwind mounted rotor.

Journal of Renewable and Sustainable Energy, 5(3):033106–1–1033106–11. https://doi.org/10.1063/1.4803749.

Thomsen, K., Petersen, J. T., Nim, E., Øye, S., and Petersen, B. (2000). A method for determination of damping for edgewise blade vibrations. *Wind Energy*. https://doi.org/10.1002/we.42.

Wanke, G., Bergami, L., Larsen, T. J., and Hansen, M. H. (2019). Changes in design driving load cases: Opterating an upwind turbine with a downwind rotor configuration. *Wind Energy*, 22:1500–1511. https://doi.org/10.1002/we.2384.

Zahle, F., Madsen, H., and Sørensen, N. (2009). Evaluation of tower shadow effects on various wind turbine concepts. *Research in Aeroelasticity DTU Report EFP-2007-II*, 1698:1–147.

Chapter 6

Review of tower shadow effect and the implications on loads and noise

The major drawback of downwind configurations is known to be the tower shadow effect. This chapter introduces the tower shadow effect on the turbine loads and noise and gives an overview of the research in the tower shadow effect of downwind turbines during the years.

6.1 Introduction

As the rotor blades pass through the tower wake they are subject to high pressure fluctuations causing high fatigue loads on the blade structure as well as an increase in low-frequency noise. Figure 6.1 shows the velocity deficit due to the tower shadow model implemented in HAWC2, for different distances to the tower wall. The potential flow model used for aeroelastic simulations of upwind configurations is shown on the left. The jet-flow model used for simulations of downwind configurations is shown on the right. It can be seen, that the potential flow model has a considerable blockage effect if the rotor is placed close to the tower in an upwind configuration. The jet-flow model for the downwind configurations, on the other hand, has a larger and more narrow velocity deficit, also at

reasonable distances to the tower wall. The implemented tower shadow model for the downwind configuration does not account for an increased turbulence level behind the tower.
Figure 6.2 shows the normalized thrust over azimuth position for the upwind and the downwind configuration of the Suzlon S111 used in this study. It can be observed that the fluctuations of the loading are much higher in the downwind configuration than in the upwind configuration leading to the higher fatigue loads of the blades observed in chapter 4 (Wanke et al. (2019)).
The tower shadow is further associated with high low-frequency noise as well as a "thumping sound" or "impulse noise" due to the pressure amplitude modulation. Figure 6.3 shows the low-frequency noise level for a 5MW turbine in an upwind configuration (left) and a downwind configuration (right) from a study by Madsen (2011). Madsen shows in a numerical study that the downwind rotor configuration has a significantly higher low-frequency noise level than the upwind rotor configuration. He further shows that an increased distance to the tower could decrease the low-frequency noise emitted. However, this effect is more pronounced for upwind configurations than for downwind configurations.

6.2 Literature review

This section reviews the research done regarding the tower shadow effect of downwind rotor configurations.
In the early 1980s, NASA and associated partners analyzed the tower shadow effect of downwind wind turbine configurations. Greene and Hubbard (1980) tried to estimate the radiated noise for the DOE/NASA MOD-1 2000kW experimental wind turbine, a 2 bladed turbine with a pipe-truss tower. They identified the flow deficit behind the tower as a major noise source and suggested to minimize interference of the blades with the tower wake to reduce turbine noise.
In a following study, Greene (1981) measured the emitted noise of turbine models with different tower porosity and rotor configurations in an anechoic wind tunnel. They showed that a flat and wide tower wake would be preferable, compared to a deep sharp wake, to reduce noise. Lattice towers were shown to produce the highest noise among the tested tower models. Upwind rotor configurations were observed to have a significantly lower noise level than any downwind configuration. Overall the tower shadow effect was found to be highly dynamic and highly under predicted by any standard calculation methods of that time, which were based on wake averages.
As high noise levels were reported from residence close to the DOE/NASA MOD-1 2000kW experimental wind turbine a psycho-acoustic study was carried out by

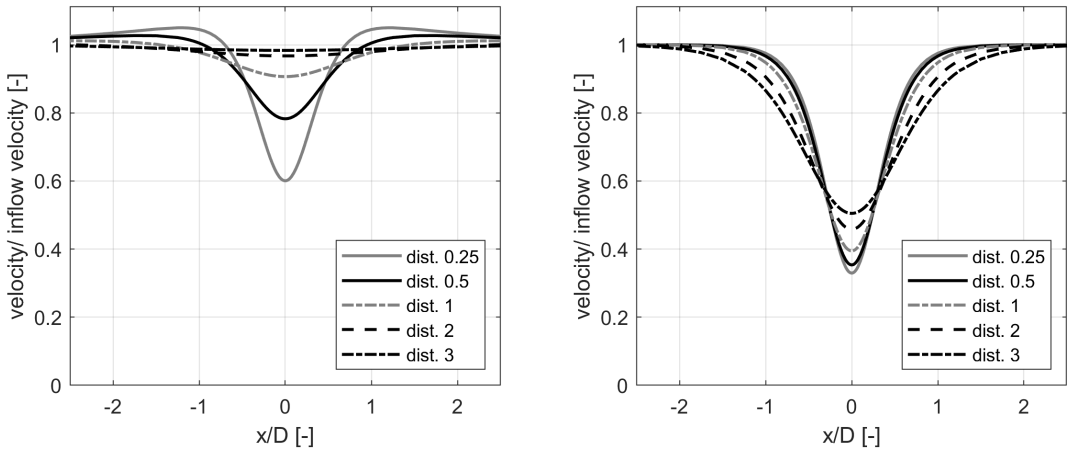

Figure 6.1: Velocity profiles of HAWC2 for the upwind and the downwind configuration at different distances behind the tower wall. The distances are normalized with the tower base diameter, the velocity is normalized with the inflow velocity.

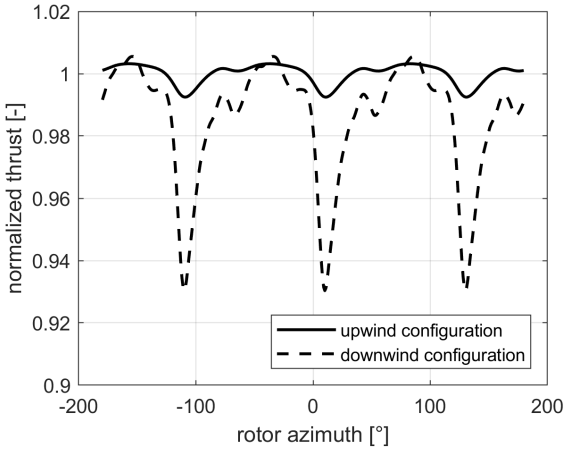

Figure 6.2: Thrust relative to mean thrust value of the upwind configuration over rotor azimuth for the upwind and the downwind configuration of the Suzlon S111.

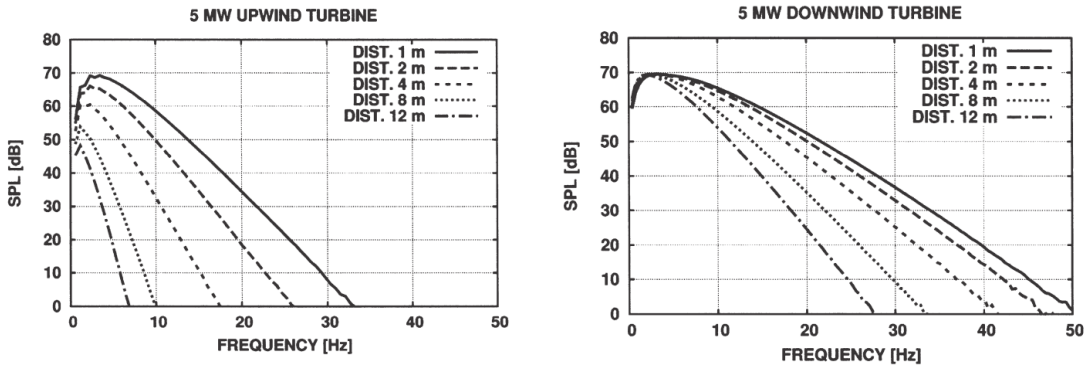

Figure 6.3: Comparison of SPL (sound pressure level) for an upwind and a downwind rotor, respectively, for different distances between the tower wall and rotor plane. Wind speed is 10 m/s and the listener position is 400m downstream the turbine. Madsen (2011)

Metzger and Klatte (1981). The "thumping"- sound, reported as annoying by the residence, was measured indoors and outdoors. Especially the unsteadiness of the noise in the low-frequency range was found to be a nuisance. The study concluded on a low-frequency noise level restriction and recommended to reduce the rotational speed of the rotor in case of noise reported by residents for already existing wind turbines.
Glasgow et al. (1981) compared the blade root moments of the DOE/NASA 100-kw MOD-0 turbine on the truss tower in an upwind and a downwind rotor configuration. They could show, that the deficit behind the truss tower causes significantly higher cyclic flapwise bending loads in the downwind configuration than in the upwind configuration. Neither in the flapwise mean bending moment nor in the edgewise bending moment a difference in loads could be shown.
Powles (1983) measured the velocity wake behind an octagonal tower segment in a wind tunnel at different distances to the tower. The work showed a significant velocity deficit expanding several diameters behind the tower, but also an area of increased turbulence up to five diameters behind the tower.
In a following study Wilmshurst et al. (1985) tried to reduce the tower shadow effect by a streamlined fairing. In experiments and simulation of a 2 bladed free yawing downwind turbine, the group quantified the emitted noise and flapwise bending loads due to the tower passage. With the fairing, the measured and simulated tower wake was significantly flatter and narrower. They reported that the "thumping" sound could be eliminated from the audible spectrum and the amplitude of the flapwise bending loads reduced to 1/3 by the use of a fairing.

However, the group also reported fairing hit incidents of the blades under operation.
As upwind rotors could generally be associated with lower noise levels they became the dominant turbine configuration in industrial applications and research focus. More than 10 years after the experiments of Powles, the "Unsteady Aerodynamics Experiment" was conducted at the National Renewable Energy Laboratory to characterize the impact of three-dimensionality, unsteadiness and flow separation effects for stall regulated upwind and downwind rotor configurations (Robinson et al. (1999)). The dataset of this measurement campaign became a widely used benchmark case for tower shadow modeling in CFD (computational fluid dynamics) and aeroelastic simulations. In these experiments two blade planforms were compared, differing only in the twist distribution. A significant variation in performance was observed in near and post-stall conditions. Here the tower shadow was observed to have a greater effect than expected: On the one hand, the inflow fluctuations produced the expected dynamic stall events. On the other and the flow characteristics within the tower shadow region was observed to change from attached to separated flow.
Research efforts regarding the tower shadow effect for downwind turbines were started at the University of Glasgow in the late 1990s. Wang et al. (1998) tried two different approaches to model the tower shadow effect on the aerodynamic blade response and compared the results to experimental data. The prescription of the wake deficit of the inflow field was found to be prohibitive on the computational power as it requires the resolution of the rotor azimuth position. A near wake formulation to effectively include the tower shadow model for lifting line theory required significantly less computational effort. Both methods were shown to agree reasonably well with the measurement data.
In a further study Wang and Coton (2001) enhanced the near wake tower shadow model with vortex shedding to handle unsteady airfoil aerodynamics. The model accounted for the effect of the shed vortices on the blade loading in the region close to the tower shadow by an iterative loop. Discrepancies to the measurements were observed when the blade operated at high angles of attack and the predictions were shown to overestimate the impulsive blade response at the exit of the tower shadow region.
Munduate et al. (2004) measured the surface pressure on an airfoil and the airfoil coefficients in a wind tunnel experiment in the presence of an artificial tower placed in front of a three bladed rotor. The experiments showed that the tower shadow is not a symmetric phenomena and only with an unsteady tower shadow model the data amplitudes and shape of the coefficients could be predicted as a function of azimuthal position.
As high fidelity investigations became more feasible the tower shadow effect was studied with CFD. Also, the downwind configuration was used at the Technical

University of Denmark to validate tower shadow models used in aeroelastic simulations.
Madsen et al. (2007) simulated the tower shadow of a 2 bladed 5MW downwind turbine in CFD to compute the wake characteristics behind the tower. The wake data was fed into the aeroelastic tool HAWC2 to extract time series for airfoil coefficient data for the noise prediction. They confirmed that the unsteadiness of the wake is needed to predict the sound pressure level correctly. The unsteadiness of the wake, mainly vortex shedding, increased the sound pressure level by 5-20db and additionally 0 to 10db when the blade passed through a discrete shed vortex. Thus, a blade passing frequency close to the strouhal number of the tower leads to a considerable noise increase. They showed that a large steady wake leads to lower noise emissions than a smaller unsteady wake.
Different tower geometries (tubular, lattice and airfoil shaped) were simulated by Zahle et al. (2009a) in 2D-CFD to develop tower shadow models for the aeroelastic tool HAWC2 for upwind and downwind configurations. It was shown that streamlined tower geometries significantly reduce the wake depth by 50% compared to a tubular tower and unsteady blade response to the vortex shedding could be eliminated. The 4-legged truss tower showed a wider wake with less deficit but the blade response was found to be highly unsteady due to the response to four separate legs.
In 2009 Zahle et al. (2009b) used an incompressible overset grid method to analyze the rotor-tower interaction of the 2 bladed teetered stall regulated downwind NREL Phase VI turbine. While a good agreement with measurement in attached flow conditions could be achieved, the agreement of the results for separated flow was not satisfying. Blade wake interaction was shown to cause high fluctuations of the normal force of up to 40% compared to the free-stream level. In the simulations the group observed a vortex shedding lock-in effect: if the rotor passing frequency or a multiple of the rotor passing frequency was close to the vortex shedding frequency of the tower the vortex shedding frequency could be shifted to the rotor frequency, shedding stable vortices. The effect could not be confirmed in the measurements, but if it should occur, high noise levels could be expected.
As rotor size was growing and the levelized cost of energy became a strong concern in turbine design and turbine research, the downwind configurations came into focus again. Since the tower clearance constraint had become a constraint in blade design downwind configurations were seen as an option to allow for more flexible, lighter and cost efficient blades. The tower shadow effect was therefore re-investigated for example at NTNU in Norway.
A calibration method for downwind wake models was developed by Reiso et al. (2013) to account for the increased vorticity behind monopoile, lattice and lattice towers under a yaw angle of 22.5°. The lattice geometry is resolved including the

k- and x-braces connecting the main tower legs. An increased turbulence level in the tower wake region was fitted to results from CFD-simulations and fed into aeroelastic simulations. The study shows that the effect on blade root fatigue load is dominated by the mean velocity deficit and the increased turbulence, with only small contributions from the unsteady effect due to vortex shedding. The increased turbulence level behind the tower increases the fatigue blade root load by 20% compared to simulations with the mean deficit model. The study confirmed that turbines with monopile tower show lower blade root fatigue load level than turbines with lattice towers, in case of the yaw misalignment.
Reiso and Muskulus (2013) investigated the effect of tower fairings in combination with increased blade flexibility. The study showed that a fairing can be used to reduce fatigue loads of rotor blades and tower. Covering parts of the tower affecting the outer blade radius could already be sufficient. Covering also the upper tower part affecting the inner blade radius required a longer shaft length to assure sufficient clearance between fairing and tower. In this case, an increase in the tower mean bending moment can be expected. Higher blade flexibility was shown to be beneficial in terms of fatigue load.
Noyes et al. (2018) analyzed a previously not published data subset of the "Unsteady aerodynamics Experiment". The measurement investigated the differences in load in an upwind configuration, a downwind configuration, a downwind configuration with fairing and a downwind configuration with fairing under yaw misalignment. The investigation showed that the alignment of the fairing is crucial for load mitigation. For a fairing misalignment of 20° no more load reduction effect could be observed.
Research efforts at Kyushu University in Japan regarded the effect of the downwind placement of the rotor on the tower. The group developed a blade element momentum (BEM)-theory to express the load variation on the tower (Yoshida (2018)). They could confirm with measurements that the thrust of the rotor reduced the drag force on the tower. The tower drag was shown to reduce proportionally to the rotor thrust. The reduction is larger if the rotor is placed close to the tower (Yoshida et al. (2019)).

6.3 Conclusion

From the literature review, a significant increase in the low-frequency noise level could be expected when the Suzlon S111 2.1MW turbine is changed from an upwind configuration into a downwind configuration. Noise reducing measures would need to be applied in order to meet standards of turbine noise levels close to residential areas.

While fairings seem to be attractive as the noise level could be significantly reduced for downwind configurations, it is doubtful whether fairings are a cost efficient solution. Firstly, a passive or active yaw system for the fairing would have to reliably assure the alignment with the wind direction. Such a system adds complexity and maintenance costs. Secondly, fairings decrease the tower clearance and might eliminate the design advantage of the downwind configurations. A larger rotor overhang is not considered to be a solution as the mean tower bottom bending loads are already significantly higher than in a comparable upwind turbine configuration (see chapter 4).
Passive systems like helix-wires or vortex generators on the tower surface could be a cheaper and more reliable solution to break up coherent vortex structures. However, the impact on noise as well as tower loads would need to be investigated in more detail.
Lattice towers might have an advantage as their lower torsional stiffness increased the blade edgewise damping (see chapter 5) and as they can be associated with lower material cost. However, from a tower shadow point of view, the tower geometry should be circular. Hybrid-lattice towers with a tubular tower in the rotor area and a lattice support structure for the lower parts of the tower might be a considerable trade-off between tower cost, blade root fatigue loads, edgewise damping and noise considerations.
Independent of the alleviation technique chosen, the review of the literature shows, that the interaction of the rotor with the turbulence structures in the wake is important. An increase in turbulence level behind the tower is currently not implemented in the tower shadow model for downwind turbines used in the aeroelastic simulations within this study. The study by Reiso et al. (2013) showed that the impact on the loads due to the vortex structure can be significant. Consequently, it should be expected that the extreme flapwise and tilt related load fluctuations, as well as the related fatigue loads, are under-predicted in the present study. The effect of the neglected turbulence should be investigated in future work to quantify the impact on the loads as well as the noise level. Computational fluid dynamics simulations could be used as suggested by Reiso et al. (2013) to simulate the wake behind towers with and without tower shadow alleviation techniques and the effect should be added to aeroelastic simulations.
The vortex shedding might not be a major contributor to the blade root fatigue loads, but as Zahle et al. (2009b) also showed significant load fluctuation an impact on the extreme loads could be expected. Further investigations as suggested above should, therefore, include investigations of the tower shadow effects on extreme loads.
Further, the impact of alleviation devices on the tower loads, for example, due to an increased drag coefficient should be investigated to give a full overview of the impact of the tower shadow effect and alleviation techniques on turbine loads

and noise.

Bibliography

Glasgow, J., Miller, D., and Corrigan, R. (1981). Comparison of upwind and downwind rotor operations of the doe/nasa l00-kw mod-0 wind turbine. *NASA Report*, TM-8744:225–234.

Greene, G. and Hubbard, H. (1980). Some calculated effects of non-uniform inflow on the radiated noise of a large wind turbine. *NASA Report*, TM-81813.

Greene, G. C. (1981). Measured and calculated characteristics of wind turbine noise. *NASA Report*, CP-2185.

Madsen, H., Johansen, J., Sørensen, N., Larsen, G., and Hansen, M. (2007). Simulation of low frequency noise from a downwind wind turbine rotor. *45th AIAA Aerospace Sciences Meeting and Exhibit*, 623.

Madsen, H. A. (2011). Low frequency noise from wind turbines mechanisms of generation and its modelling. *Journal of low frequency noise, vibration and active control; Vol. 29; p. 239-251.*

Metzger, F. and Klatte, R. (1981). Status report on downwind horizontal axis wind turbine noise prediction. *NASA Report*, N82-23684 14-44:425–430.

Munduate, X., Coton, F., and Galbraith, R. (2004). An investigation of the aerodynamic response of a wind turbine blade to tower shadow. *Proceedings of the 4th Asme/jsme Joint Fluids Engineering Conference*, pages 2585–2592.

Noyes, C., Quin, C., Loth, E., and Schreck, S. (2018). Measurements and predictions of wind turbine tower shadow and fairing effects. *Journal of Wind Engineering and Industrial Aerodynamics*, 179:297–307. https://doi.org/10.1016/j.jweia.2018.06.012.

Powles, S. (1983). The effects of tower shadow on the dynamics of a horizontal-axis wind turbine. *Wind Engineering*, 7(1):26–42.

Reiso, M., Hagen, T., and Muskulus, M. (2013). A calibration method for downwind wake models accounting for the unsteady behaviour of the wind turbine tower shadow behind monopile and truss towers. *Journal of Wind Engineering and Industrial Aerodynamics*, 121:29–38. https://doi.org/10.1016/j.jweia.2013.07.016.

Reiso, M. and Muskulus, M. (2013). The simultaneous effect of a fairing tower and increased blade flexibility on a downwind mounted rotor. *Journal of Renewable and Sustainable Energy*, 5(3):033106–1–1033106–11. https://doi.org/10.1063/1.4803749.

Robinson, M., Hand, M., Simms, D., and Schreck, S. (1999). Horizontal axis wind turbine aerodynamics: Three-dimensional, unsteady and separated flow influences. *Proceedings of 3rd Asme/jsme Joint Fluids Engineering Conference*.

Wang, T. and Coton, F. (2001). A high resolution tower shadow model for downwind wind turbines. *Journal of Wind Engineering and Industrial Aerodynamics*, 89:873–892.

Wang, T., Coton, F., and Galbraith, R. (1998). An examination of tower shadow modelling strategies for downwind turbines. *Asme Wind Energy Symposium*, pages 20–30.

Wanke, G., Bergami, L., Larsen, T. J., and Hansen, M. H. (2019). Changes in design driving load cases: Opterating an upwind turbine with a downwind rotor configuration. *Wind Energy*, 22:1500–1511. https://doi.org/10.1002/we.2384.

Wilmshurst, S., Powles, S., and Wilson, D. (1985). The problem of tower shadow. *Proceedings of the Bwea Wind Energy Conference (british Wind Energy Association)*, pages 95–102.

Yoshida, S. (2018). Combined blade-element momentum—lifting line model for variable loads on downwind turbine towers. *Energies*, 11(2521). https://doi.org/10.3390/en11102521.

Yoshida, S., Fujii, K., MHamasaki, and Takada, A. (2019). Effect of rotor thrust on the average tower drag of downwind turbines. *Energies*, 12(227). https://doi.org/doi:10.3390/en12020227.

Zahle, F., Madsen, H., and Sørensen, N. (2009a). Evaluation of tower shadow effects on various wind turbine concepts. *Research in Aeroelasticity DTU Report EFP-2007-II*, 1698:1–147.

Zahle, F., Sørensen, N., and Johansen, J. (2009b). Wind turbine rotor-tower interaction using an incompressible overset grid method. *Journal of Wind Energy*, 12:594–619. https://doi.org/10.1002/we.327.

Chapter 7

Qualitative yaw stability analysis of free-yawing downwind turbines

The following will present the article written for the investigations of a free yawing downwind turbine, in the revised and finally accepted manuscript version, formatted for the thesis format.

Wanke, G., Hansen, M. H., and Larsen, T. J.: **Qualitative yaw stability analysis of free-yawing downwind turbines**, *Wind Energ. Sci.*, 4, 233-250, https://doi.org /10.5194 /wes-4-233-2019, 2019

Manuscript received: 19 Oct 2018
Manuscript revised: 15 Feb 2019
Manuscript accepted: 25 Apr 2019

Qualitative yaw stability analysis of free-yawing downwind turbines

Gesine Wanke[1], Morten H. Hansen[3], Torben J. Larsen[2]

[1] Blade Science Center Suzlon, Vejle Denmark
[2] Mads Clausen Institute, University of Southern Denmark, Sønderborg, Denmark
[3] DTU Wind Energy, Technical University of Denmark, Roskilde, Denmark

Correspondence: Gesine Wanke, Suzlon Blade Science Center, Havneparken 1, 7100 Vejle, Denmark. E-mail: gesine.wanke@suzlon.com

Abstract

This article shows qualitatively the yaw stability of a free yawing downwind turbine and the ability of the turbine to align passively with the wind direction, using a two degree of freedom model. An existing model of a Suzlon S111 upwind 2.1 MW turbine is converted into a downwind configuration with a 5° tilt and a 3.5° downwind cone angle. The analysis shows that the static tilt angle causes a wind speed dependent yaw misalignment of up to -19° due to the projection of the torque onto the yaw bearing and the skewed aerodynamic forces caused by wind speed projection. With increased cone angles, the yaw stiffness can be increased for better yaw alignment and the stabilization of the free yaw motion. The shaft length influences the yaw alignment only for high wind speeds and cannot significantly contribute to the damping of the free yaw mode within the investigated range. Asymmetric flapwise blade flexibility is seen to significantly decrease the damping of the free yaw mode, leading to instability at wind speeds higher than 19 ms^{-1}. It is shown that this additional degree of freedom is needed to predict the qualitative yaw behaviour of a free yawing downwind wind turbine.

7.1 Introduction

With the increase in wind turbine rotor size and the increase in rotor blade flexibility, downwind concepts where the rotor is placed behind the tower re-experience an increase in research effort. The downwind concept potentially

comes with the option of a passive yaw alignment. A passive yaw concept could save costs on the yaw system, decrease the maintenance and reduce the complexity of the yaw system. In situations where one side of a rotor under yawed inflow is loaded higher than the other, the resulting forces on the blades create a restorative yaw moment and could potentially align the rotor with the wind direction.

These passive yaw systems have been investigated already in the 1980s and the early 1990s. Corrigan and Viterna (1982) studied the free yaw performance of the two bladed, stall controlled MOD-0 100 kW turbine with different blade sets. They observed that the turbine aligns with the wind direction at yaw errors between -45° and -55°. The yaw motion was positively damped for short term wind variations at these positions. The power production was significantly lower compared to the forced yaw alignment. An improvement of the alignment with the wind direction could be achieved by the elimination of the tilt of the shaft. Wind shear on the other hand was observed to have a negative influence on the yaw alignment.

In further tests on the MOD-0 100 kW turbine, Glasgow and Corrigan (1983) investigated the influence of bend-twist coupling and the airfoil at the tip section for a tip-controlled configuration. Their study showed, a strong dependency of the yaw alignment on the wind speed. For the bend-twist coupled rotor the minimum yaw error was observed to be -25°. The comparison between two different tip airfoils showed that the alignment could be significantly improved with an airfoil with favourable characteristics.

Olorunsola (1986) investigated the yaw torque for different yaw inflow angles. He emphasized the risk of stall induces vibrations and increased fatigue loads in cases where the aerodynamically provided yaw torque cannot overcome the frictional torque of the yaw bearing, leading potentially to an operation with high yaw misalignment.

Simple equations of motion for the aerodynamic yaw moment were used by Eggleston and Stoddard (1987) to explain observed yaw stability behaviour of up- and downwind turbines. They identified a yaw tracking error due to gravity and wind shear, resulting into a constant misalignment of the rotor with the wind speed. Wind shear and turbulence were shown to add a variable yaw error to the rotor alignment. They further showed that two restorative moments were present due to the wind speed projection with the yaw angle itself and a projection with a yaw angle combined with a steady cone angle for cantilevered rotors. The later was identified to be most efficient to reduce the yaw error.

In 1986, the University of Utah and the Solar Energy Research Institute in the US started to develop and validate a model for the prediction and understanding of yaw behaviour. In a time domain modelling approach, they coupled the flapwise blade motion to the yaw motion. In several studies (e.g Hansen and

Cui (1989), Hansen et al. (1990) and Hansen (1992)), the resulting YawDyn tool was used to reproduce the results of measurement campaigns and to identify the most influential parameter on the free yaw behaviour. The researchers emphasized the importance to include dynamic stall effects and skewed inflow model in the prediction of yaw behaviour. They could further show the influence of blade mass imbalances, tower shadow, rotor tilt and horizontal and vertical wind shear as the contribution to asymmetry of the rotor loading from flapwise blade root bending moments. While the study showed that the yaw behaviour could be simulated qualitatively, the tool was not able to capture the quantitative yaw dynamics correctly in all test cases.

Other modelling approaches were chosen for example by Madsen and McNerney (1991) who developed a frequency domain model to study the statistics of yaw response and power production of a 100 kW turbine in dependency of a turbulent wind regime. They confirmed that the horizontal wind shear is a major source for yaw errors and the related power loss.

Pesmajoglou and Graham (2000) on the other hand predicted the yaw moment coefficient for different sized turbine models with a free vortex lattice model. They showed a good agreement of the mean yaw moment with wind tunnel experiments in cases where airfoil stall does not show a large contribution to the yaw moments. In these cases, their model could successfully predict the variation of the yaw moment coefficient in a turbulent wind field.

Verelst and Larsen (2010) investigated the restoring yaw moment due to yawed inflow on a stall regulated 140 kW machine with stiff rotor blades and different cone configurations. They showed an increase of the restorative effect on the yaw moment from higher cone angles, because the cone angle increases the imbalance of the rotor forces and therefore the restorative yaw moment. However, for negative yaw errors they showed that the midspan part of the blades contributes to a decrease in the restorative yaw moment, related to the stall effect at rated wind speed. This effect could be reduced, but not eliminated with the highest tested cone angles.

Picot et al. (2011) studied the effect of swept blades on a coned rotor on a 100 kW stall regulated turbine. They investigated the restorative yaw moment in a fixed yaw configuration, as well as, the yaw alignment in a free yaw configuration. In their study, they observed yaw oscillations around rated wind speed. The azimuth variation of inflow condition due to wind shear increased the yaw oscillation. They confirmed that the inner part of the blade being in deep stall, contributes to the reduction of the restorative yaw moment. With backward swept blades, the destabilizing effect of the stall was reduced, but occurred over a larger wind range. Since the blade was passively unloaded at higher wind speeds and the inflow condition due to the position of the blade segments differed along the blade due to deformation, the different blade segments were subject to stall

at different wind speeds.
Kress et al. (2015) used a scaled model of a commercial 2 MW downwind turbine to compare the restorative yaw moment in a water tunnel in a downwind and upwind configuration. They compared the influence of different cone angles, different yaw angles and different tip speed ratios close to optimum tip speed ratio. They observed a restorative yaw moment for all downwind configurations. In the upwind configuration only configurations with high cone angles showed a restorative yaw moment, which was seen to be significantly smaller than in the downwind configuration.
Verelst et al. (2016) showed measurements of a 280 W downwind turbine in a open jet wind tunnel. They released the rotor yaw from large yaw errors ($\pm 35°$) and measured the angle where the rotor would passively align with the wind direction, as well as the dynamic yaw response. They tested the angle of alignment for a rotor with stiff/flexible blades and swept/non swept blades. They observed that the equilibrium yaw angle was not exactly zero and they assumed that the yaw moment is too small to overcome the bearing friction and the rotor inertia. They further showed that the steady state yaw angle found from initially negative yaw errors was higher than for positively yaw errors. They stated that the reason could be an asymmetry in the inflow due to the tower shadow or a non zero steady state yaw angle for a zero yaw moment. They further found a different yaw stiffness for positive and negative yaw errors, leading to different system responses with an under-damped response only for positive yaw errors.
In this article the equilibrium yaw position of a free yawing, pitch regulated 2.1 MW downwind turbine is investigated. The influence of geometrical parameter such as cone, tilt and shaft length on the equilibrium yaw position are considered. Further, a simple two degree of freedom model with free yaw and tower side-side motion is developed to calculate the damping of the free yaw mode. The influence of cone, shaft length, and the center of gravity position of the nacelle on the damping of the free yaw mode are regarded. It is shown that a full alignment with the wind direction is only achievable without tilt angle of the turbine and inclination angle of the wind field. It is shown that large cone angles increase the alignment with the wind direction and the damping of the free yaw mode. Finally, it is shown that flapwise blade flexibility needs to be added to the two degree of freedom model, as the flapwise flexibility will significantly reduce the damping and the yaw equilibrium could become unstable.

7.1.1 Yaw moment, aerodynamic yaw stiffness and damping mechanisms

The total moment on the yaw bearing is determined by different mechanisms creating the yaw loading around the tower longitudinal axis. The following estimation sketches the main contributors to the total yaw moment M_{yaw} as a scalar quantity.

$$M_{yaw} \approx M_{Q,\delta} + M_{W,\delta} + M_a + M_{W,\theta} + M_{W,\gamma_c,\theta}$$

where the torque projection $M_{Q,\delta}$ and the moment due to wind speed projection from tilt angle $M_{W,\delta}$ are dependent on the tilt angle δ. The moment due to induction variation from the skewed yaw inflow is M_a, the moment due to projection of the wind speed with the yaw angle is $M_{W,\theta}$ and the moment due to wind speed projections with a combined cone and yaw angle is $M_{W,\gamma_c,\theta}$.
There are two yaw moment contributions due to the tilt angle. The first one is a projection of the main shaft torque $M_{Q,\delta}$ onto the yaw axis with the sine of the tilt angle (structural effect of tilt). As power production changes with wind speed W, the yaw moment due to torque changes with wind speed. In case of a yaw misalignment, the torque is reduced and influences the yaw moment accordingly. The second moment caused by the tilt angle $M_{W,\delta}$ is due to the wind speed projection, illustrated in Fig. 7.1 (aerodynamic effect of tilt, see Fig. 7.4 for angle definition). Figure 7.1 (a) shows that the projection of the incoming wind speed is added to the relative velocity due to rotation ΩR when the blade moves up (azimuth range $\psi = 0°$ to $\psi = 180°$, azimuth position of $\psi = 90°$ shown in Fig. 7.1) and subtracted from the rotational speed when the blade moves down (azimuth range $\psi = 180°$ to $\psi = 360°$, azimuth position of $\psi = 270°$ shown in Fig. 7.1). The difference in projected wind speed due to the tilt angle creates a variation of angle of attack α over the azimuth position. Figure 7.1 (b) shows the variation of the yaw moment over azimuth position for different wind speeds due to the force at 75% of the rotor radius. It can be seen that the sum of the loading from three blades is not zero. In the attempt to isolate the effect of wind speed projection from a tilt angle the interaction with other effects, e.g. a combination of several angle projection (tilt, cone and yaw) or the skewed inflow model for tilted inflow are not included in the figure. The two tilt dependent moments, $M_{Q,\delta}$ and $M_{W,\delta}$ will cause a yaw misalignment for any free yawing turbine with a structural tilt angle. An inclination angle of the wind field would also cause a moment from projections as $M_{W,\delta}$.
The moment due to induction variation over the rotor plane M_a, the moment due do wind speed projections from the a yaw angle $M_{W,\theta}$ and the moment due to wind speed projections from a combination of yaw and cone angle $M_{W,\gamma_c,\theta}$ are restorative moments. The restorative moments are creating an aerodynamic yaw

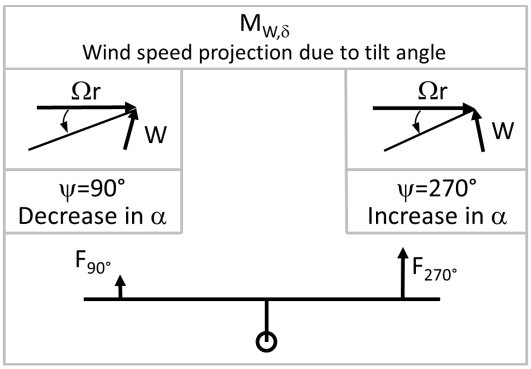

(a) Yaw moment sketch due to wind speed projection with tilt angle.

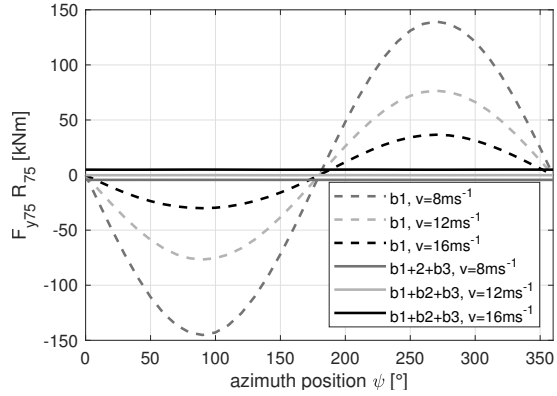

(b) Yaw moment estimate from F_y at $r/R = 75\%$ and δ=5°.

Figure 7.1: Aerodynamic yaw moment for the tilt angle of a downwind rotor sketched in (a) and the roughly estimated respective variation of yaw moment of the force at 75% rotor radius with 5° tilt in (b).

stiffness as shown in Fig. 7.2. A yaw displacement will introduce a variation of induction over the rotor plane, due to the skewed inflow model, as one half of the rotor is positioned deeper in the wake than the other half. The upstream pointing blade is therefore higher loaded and a restoring yaw moment is created (Fig. 7.2 (a)). It can be seen in Fig. 7.2 (b) that relatively high yaw angles are required to create a significant restorative yaw moment from the variation of induction over the rotor plane compared to other stiffness mechanisms. An induction variation due to a skewed inflow is also created by the tilt angle. For a simple sketch of the main mechanisms this effect is neglected in this sketch.
The positive yaw displacement as sketched in Fig. 7.2, creates a projection of the incoming wind speed. When the blade is pointing down ($\psi = 0°$), the projected wind speed component is subtracted from the rotational speed, while it is added to the rotational speed, when the blade is pointing up. The resulting variation of angle of attack is the reason for an in-plane force at the hub center that creates a moment with the arm of the shaft length (Fig. 7.2 (c)). This effect creates the smallest yaw moment of the discussed effects. However, with higher pitch angles, the contribution becomes larger at higher wind speeds, due to the flapwise force component that is projected to the in-plane forces.
In the case of coning, there is a difference in the projected wind speed between the left and the right side of the rotor when the rotor is yaw misaligned, resulting in a difference in angle of attack. From the difference in loading, a restoring yaw

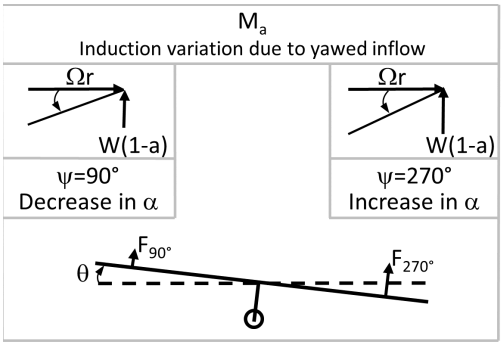

(a) Stiffness mechanism: induction variation.

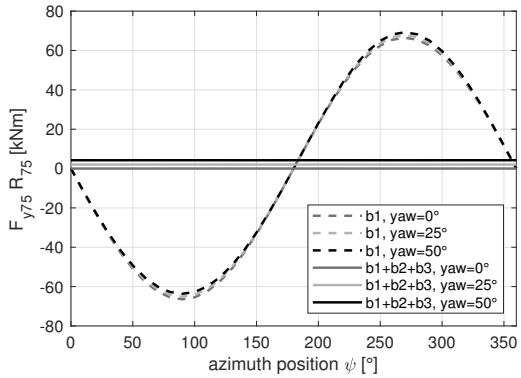

(b) Yaw moment estimate from F_y at $r/R = 75\%$.

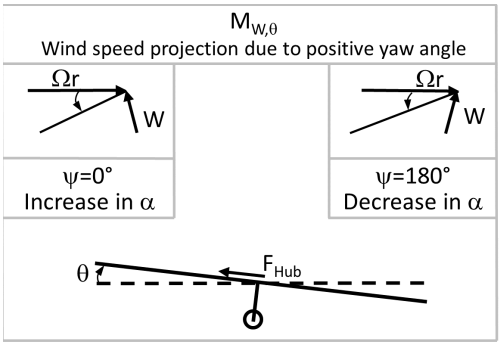

(c) Stiffness mechanism: yaw projection.

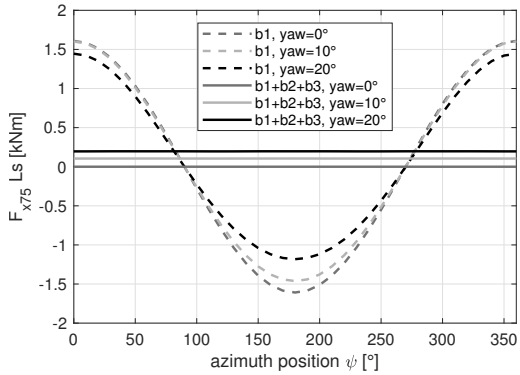

(d) Yaw moment estimate from F_x at $r/R = 75\%$.

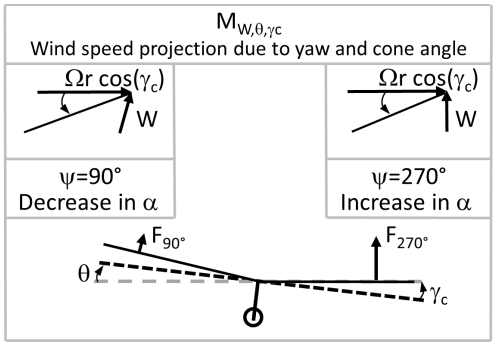

(e) Stiffness mechanism: yaw and cone projection.

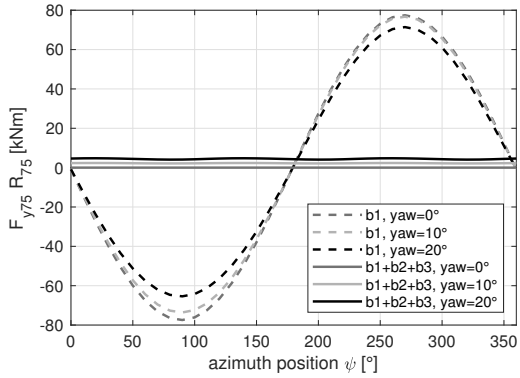

(f) Yaw moment estimate from F_y at $r/R = 75\%$ and $\gamma_c = 3.5°$.

Figure 7.2: Aerodynamic mechanisms for yaw stiffness of a downwind rotor on the left and the roughly estimated respective variation of yaw moment of the force at 75% rotor radius for wind speeds of 12 ms^{-1} over azimuth position on the right.

moment is created (Fig. 7.2 (e)). It can be seen in Fig. 7.2 (f) that relatively large yaw moments can be created for small yaw angles compared to the other two stiffness mechanisms, which makes the cone angle the most effective design parameter to influence the yaw stiffness.
Compared to the mechanical stiffness of a spring, the aerodynamic stiffness term does not necessarily create a restorative yaw moment. Negative force coefficient slopes over the angle of attack can create a negative stiffness term. In this case, any disturbance from the equilibrium point would increase the force moving the system away from the equilibrium point. An example would be the operation of the turbine during stall.
The damping mechanism for the free yaw motion is shown in Fig. 7.3. The aero-

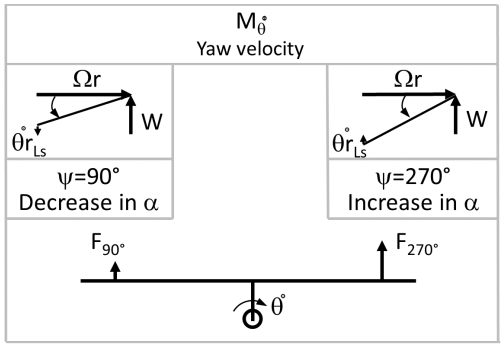

Figure 7.3: Aerodynamic mechanism for yaw damping for a downwind rotor.

dynamic damping of the yaw motion is created by the rotational velocity due to the yawing motion. The rotational yaw velocity is added to the wind speed on one side of the rotor and subtracted on the other side of the rotor which leads to the change in angle of attack creating an imbalance in the loading that counteracts the yaw motion. Again, the created moment is only counteracting the yaw motion if the the slope of the airfoil coefficient over angle of attack is positive, i. e. operating in attached flow.
The stability of the equilibrium position of the yaw mode can be determined from the eigenvalue analysis of the system matrices. If the resulting real part of the eigenvalue λ is less than zero and the calculated eigenfrequency ω is non-zero, there is a positively damped yaw oscillation. If the real part of the eigenvalue and the eigenfrequency are larger than zero, the yaw equilibrium is unstable and the yaw motion is negatively damped (flutter, not to be confused with classical flutter). If the linear stiffness matrix for small yaw angles away from the equilibrium is negative definite, the system is driven away from the equilibrium without

oscillations (divergence).

$$\text{Flutter instability: } \Re(\lambda) > 0 \text{ and } |\omega| > 0$$
$$\text{Divergence instability: } \Re(\lambda) > 0 \text{ and } \omega = 0$$

7.2 Methods

The study is regarding two aspects. Firstly, the equilibrium yaw angle of a free yawing turbine model, which can align passively with the wind direction, and secondly the dynamic stability of the free yaw mode. The study uses a simplified model of the Suzlon 2.1 MW turbine S111 (wind class IIIA). The original turbine has a 3-bladed upwind rotor with a diameter of 112 m and a tower of 90 m height. The rotor is tilted 5° and coned 3.5°. The turbine is operating at variable speed below rated power and is pitch regulated above the rated wind speed of 9.5 ms^{-1} with a constant power approach. The operational range is between 4 ms^{-1} and 21 ms^{-1}. In the investigation, the rotor configuration is changed to a downwind configuration. Thus, the rotor is shifted behind the tower, while nacelle and shaft are yawed by 180°. For the study further simplifications are made. The blade geometry is modified: the prebend is neglected and quarter chord point of each airfoil is aligned on the pitch axis. The shaft intersects with the yaw axis. Figure 7.4 shows the simplified turbine model with the geometrical parameter shaft length (L_s) and distance to the center of gravity (L_{cg}), tilt angle (δ) and cone angle (γ_c). These geometrical parameter will be used for a sensitivity study regarding the equilibrium yaw angle and the dynamic stability of the free yaw mode. All angles are sketched as positively defined for figures in this paper. The model is set up with two degrees of freedom (DOF) representing the free yaw motion $\theta(t)$ and the tower side-side motion $u_x(t)$ illustrated in Fig. 7.4. The ground fixed frame originates in the tower top center. The distance between the origin and the center of gravity of the nacelle assembly is L_{cg} and L_s represents the distance from the origin to the hub center (shaft length). The hub length is r_h and $z_{b,k}$ represents the position along the blade number k. The cone angle is denoted γ_c and δ is the tilt angle. The azimuth position of each blade is $\psi(k,t) = \Omega t + \frac{2\pi}{3}(k-1)$, where Ω is the constant rotational speed of the shaft. The stiffness of the tower is represented by a linear spring with the stiffness k_x. To the right of Fig. 7.4, a cross section of the blade is displayed, with the inflow velocity U and the respective U_x and U_y component, the flow angle ϕ_k and the pitch angle β_p which includes the global blade pitch as well as the local twist. A steady wind field is assumed without shear, veer, inclination, turbulence or tower shadow.

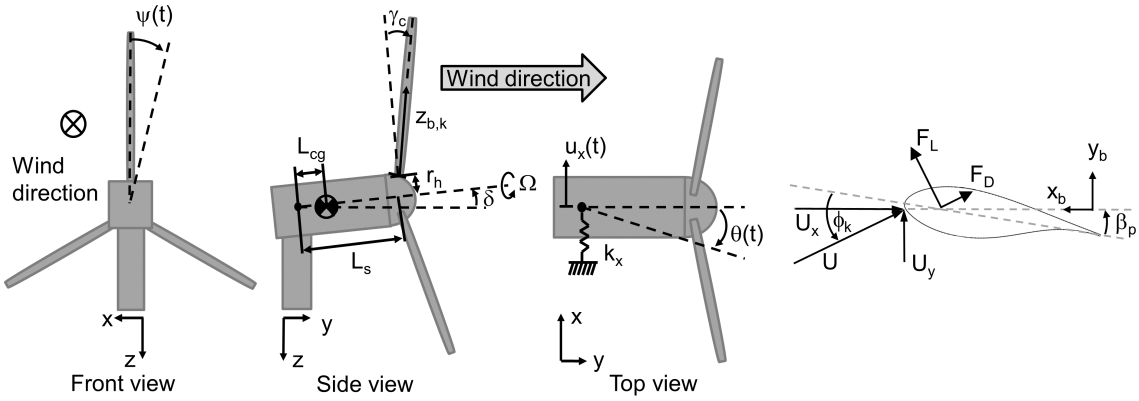

Figure 7.4: Schematics of turbine model and the according coordinate systems, front view, side view and top view (from left) and the sketch of the inflow and forces on the airfoil with the coordinate system.

7.2.1 Equilibrium yaw angle

The equilibrium yaw angle, where the aerodynamic forces are in balance, is calculated with MATLAB (Version 2018a). From a Blade Element Momentum (BEM)-code with yaw and tilt model, the forces on the rotor are calculated and the yaw angle associated with the 0-mean yaw moment on the yaw bearing is interpolated between the loading for different yaw angles, assuming that the effect of inertial terms is negligible. The BEM-code is based on the aerodynamic module of the aeroelastic code HAWC2 (Larsen and Hansen (2014)). The basic principle of the induction varying over the rotor plane is briefly described in Madsen et al. (2011). Figure 7.5 shows the flow chart of the implemented BEM-method. As in HAWC2, a polar grid is set up to define the calculation points for the induction. The free wind speed W is projected via a matrix rotation to the grid points, and the induction a is initialized. Within a converging loop the induced velocity W_{ind} and the actual velocity at each grid point W_{grid} are calculated. From the velocity the inflow angle ϕ and the angle of attack α are calculated. The lift and drag coefficients C_L and C_D are interpolated within a look-up table. From this the normal force coefficient C_n and the thrust coefficient C_T is calculated and the tip loss correction is applied. From the corrected thrust coefficient the new induction is calculated. The values are saved for each grid point and the average induction over all grid points is calculated. From the average induction a reduction factor is calculated. This factor is applied to each grid point to reduce the average induction according to the reduced thrust from

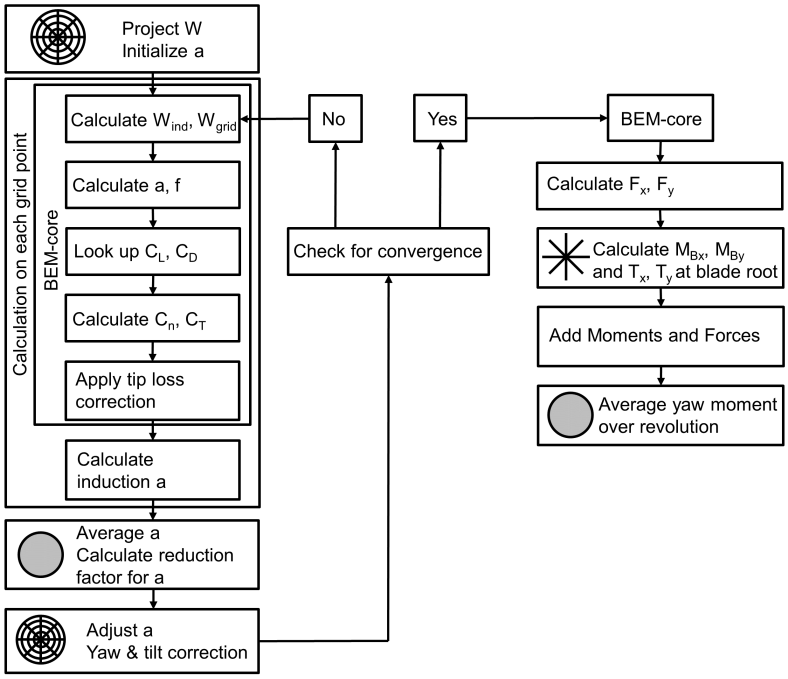

Figure 7.5: Flow chart for the implemented BEM-code to compute the equilibrium yaw angle.

the skewed inflow. Further, the local induction on each grid point is corrected according to the azimuth position of the blade by a yaw and a tilt factor. If the induction is then converged for all grid points within the requested tolerance, one more BEM-core operation is performed to calculate the force coefficients. From the force coefficients, the actual forces F_x and F_y are computed at the grid points. Those forces are integrated along the radial lines of the grid to blade root bending moments M_{Bx} and M_{By}, as well as to shear forces at the blade root T_x and T_y. The total yaw moment is calculated at the hub for a full revolution, extracting values from the calculation on the grid. The total moment contribution from the out-of-plane bending moments at the hub $M_{Bx,\psi,\ hub,\ total}$ is

$$M_{Bx,\psi,\ hub,\ total} = \sum_{k=1}^{3} M_{Bx,k} \sin(\psi_k) \tag{7.1}$$

where ψ_k is the azimuth position of the three individual blades, with ψ =0° pointing downwards. It should be noted that there is a contribution to the yaw

moment from the blade root bending moments, as well as from the shear forces, which have the shaft length as a distance to the center of yaw rotation (see Fig. 7.2 (c)). The total yaw moment is averaged over the rotor revolution. Finally, via interpolation the equilibrium position is found. The equilibrium yaw position is the yaw angle where the average yaw moment is zero.
For the original turbine configuration, this method is validated with a HAWC2 simulation with a free-yawing turbine model without bearing friction. Thus, the rotor can align freely with the wind field. The wind field is steady, without shear, veer, inclination angle or tower shadow model. The dynamic stall effects are neglected. The validated BEM-code is then used for a parameter study, investigating the influence of tilt and cone angle, as well as the shaft length onto the equilibrium yaw angle of the turbine over wind speed. The operational conditions of the turbine are purely based on the free wind speed, neglecting any loss in power production due to skewed inflow.

7.2.2 Dynamic stability of the free yaw mode

To evaluate the dynamic stability of the free yaw mode, a simple 2DOF model is set up in Maple (MapleSoft, Version 2016.2). The 2DOF model based on an existing 15DOF model without cone angle, described by Hansen (2003) and Hansen (2016). The two degrees of freedom are the tower side-side motion ($u_x(t)$) and the free yaw motion ($\theta(t)$). A 2DOF model is chosen, in the attempt to keep the model as simple and fast as possible. The advantage would be, that such model could in principle be used to make basic design choices very fast. The tower side-side is chosen as the second degree of freedom, as it couples directly to the yaw motion via the shaft length and the rotor mass. The model does not include structural damping or bearing friction. The tilt angle is assumed to be 0°, to align the rotor with the wind direction.
The governing equations of motion are set up from the Lagrange-equation without structural damping:

$$\frac{d}{dt}\left(\frac{\partial L}{\partial \dot{x}_i}\right) - \frac{\partial L}{\partial x_i} = Q_i \text{ for } i = 1, 2 \tag{7.2}$$

where the Lagrangian $L = T - V$ is the difference between the kinetic energy T and the potential energy V and Q_i are the aerodynamic forces. The total kinetic energy can be written as:

$$T = \frac{1}{2} m_{Na} \vec{r}^{\,2}_{cg,Na} + \frac{1}{2} I_z \dot{\theta}^2 + \frac{1}{2} \sum_{k=1}^{3} m_h \, \vec{r}_{h,k} \cdot \vec{r}_{h,k} + \frac{1}{2} \sum_{k=1}^{3} \int_0^R m_b \, \vec{r}_{cg,k} \cdot \vec{r}_{cg,k} \, dz \tag{7.3}$$

Where m_{Na} represents the total mass of the nacelle and shaft, I_z is the total rotational inertia of the nacelle and shaft around the yaw axis, m_h is the total mass of the hub, represented as a point mass and m_b is the distributed blade mass. The vectors $\vec{r}_{cg,Na}$, $\vec{r}_{h,k}$ and $\vec{r}_{cg,k}$ represent the position of the nacelle mass, the hub mass and the blade center of gravity along the blade axis of the k-th blade with the total length R and $\dot{(\,)}$ denotes their respective time derivative. These position vectors can be represented as

$$\vec{r}_{cg,Na} = \begin{bmatrix} u_x - \sin(\theta)\, L_{cg} \\ \cos(\theta)\, L_{cg} \\ 0 \end{bmatrix} \tag{7.4}$$

,

$$\vec{r}_{h,k} = \begin{bmatrix} u_x \\ 0 \\ 0 \end{bmatrix} + \mathbf{T}_\theta \left(\begin{bmatrix} 0 \\ L_s \\ 0 \end{bmatrix} + \mathbf{T}_{\psi,k} \begin{bmatrix} 0 \\ 0 \\ r_h \end{bmatrix} \right) \tag{7.5}$$

and

$$\vec{r}_{cg,k} = \begin{bmatrix} u_x \\ 0 \\ 0 \end{bmatrix} + \mathbf{T}_\theta \left(\begin{bmatrix} 0 \\ L_s \\ 0 \end{bmatrix} + \mathbf{T}_{\psi,k} \left(\begin{bmatrix} 0 \\ 0 \\ r_h \end{bmatrix} + \mathbf{T}_{\gamma_c} \begin{bmatrix} 0 \\ 0 \\ z \end{bmatrix} \right) \right) \tag{7.6}$$

It should be noted, that the center of gravity of the blade sections is assumed to be is aligned on a straight line for simplicity. The rotation matrices for yaw $\mathbf{T}_\theta$, rotor rotation $\mathbf{T}_{\psi_k}$ and the cone angle $\mathbf{T}_{\gamma_c}$ are defined, according to the right hand rule, as

$$\begin{aligned} \mathbf{T}_\theta = \begin{bmatrix} \cos(\theta) & -\sin(\theta) & 0 \\ \sin(\theta) & \cos(\theta) & 0 \\ 0 & 0 & 1 \end{bmatrix}, \; \mathbf{T}_{\psi_k} = \begin{bmatrix} \cos(\psi_k) & 0 & \sin(\psi_k) \\ 0 & 1 & 0 \\ -\sin(\psi_k) & 0 & \cos(\psi_k) \end{bmatrix} \\ \mathbf{T}_{\gamma_c} = \begin{bmatrix} 1 & 0 & 0 \\ 0 & \cos(\gamma_c) & \sin(\gamma_c) \\ 0 & -\sin(\gamma_c) & \cos(\gamma_c) \end{bmatrix} \end{aligned} \tag{7.7}$$

where the cone angle is a negative rotation for a positive cone angle.
The potential energy V is formulated in the general manner, including a yaw stiffness as

$$V = \frac{1}{2} k_x u_x^2 + \frac{1}{2} G_z \theta^2 \tag{7.8}$$

where G_z is the yaw stiffness, which will be set to G_z =0 Nm^{-1} for the analysis of the free yawing turbine. Inserting the Lagrangian L into Eq. (7.2) and linearization about the equilibrium position at the steady state ($\vec{x} = \dot{\vec{x}} = 0$) gives the structural part of the linear equation of motion. The linearization around a

steady state of $\vec{x} = 0$ assumes that there exists an equilibrium position where the rotor is fully aligned with the wind direction, as the tilt angle is 0°. From the linearized model the stability due to small angle variations around the equilibrium can be investigated. It can be seen from Fig. 7.4 on the right that the relative inflow velocity at the blade $\vec{U}_k$, the inflow angle ϕ_k and the angle of attack α_k are

$$U_k = \sqrt{U_{x,k}^2 + U_{y,k}^2}, \quad \phi_k = \arctan\left(\frac{U_{y,k}}{U_{x,k}}\right), \quad \alpha_k = \phi_k - \beta_p \tag{7.9}$$

where β_p includes the pitch angle and the local twist. For simplicity, it is assumed that the aerodynamic center $\vec{r}_{ac,k}$ is coinciding with the center of gravity on a straight line, the z_b axis. The vector of the relative velocity is defined as

$$\vec{U} = (\mathbf{T}_\theta \mathbf{T}_{\psi_k} \mathbf{T}_{\gamma_c})^{-1} \left(\dot{\vec{r}}_{ac,k} - \begin{bmatrix} 0 \\ W \\ 0 \end{bmatrix} \right) \tag{7.10}$$

where W is the incoming undisturbed wind to the rotor plane.
The resulting forces in the global coordinate frame can be read as

$$\vec{F}_k(z, \vec{x}, \dot{\vec{x}}) = \mathbf{T}_\theta \mathbf{T}_{\psi_k} \mathbf{T}_{\gamma_c} \begin{bmatrix} f_x(z, \vec{x}, \dot{\vec{x}}) \\ f_y(z, \vec{x}, \dot{\vec{x}}) \\ 0 \end{bmatrix} \tag{7.11}$$

where the aerodynamic force components f_x and f_y are combined from the lift and drag coefficients as

$$\begin{aligned} f_x &= \frac{1}{2}\rho c U_k^2(z, \vec{x}, \dot{\vec{x}}) \\ &\Big(C_L(\alpha_k(z, \vec{x}, \dot{\vec{x}}))\sin\ \phi_k(z, \vec{x}, \dot{\vec{x}}) - C_D(\alpha_k(z, \vec{x}, \dot{\vec{x}}))\cos\ \phi_k(z, \vec{x}, \dot{\vec{x}})\Big) \\ f_y &= \frac{1}{2}\rho c U_k^2(z, \vec{x}, \dot{\vec{x}}) \\ &\Big(C_L(\alpha_k(z, \vec{x}, \dot{\vec{x}}))\cos\ \phi_k(z, \vec{x}, \dot{\vec{x}}) + C_D(\alpha_k(z, \vec{x}, \dot{\vec{x}}))\sin\ \phi_k(z, \vec{x}, \dot{\vec{x}})\Big) \end{aligned} \tag{7.12}$$

where ρ is the air density and C_L and C_D are the lift and drag coefficients respectively.
Inserting the time derivative of Eq. (7.6) representative for $\dot{\vec{r}}_{ac,k}$ and Eq. (7.11) and Eq. (7.9) to Eq. (7.10) and Eq. (7.12) and linearization around the steady state gives the linear aerodynamic matrices in the form of

$$\vec{Q} = -\mathbf{C}_{aero}\ \dot{\vec{x}} - \mathbf{K}_{aero}\ \vec{x} \tag{7.13}$$

where the aerodynamic forces $\vec{Q}$ have no constant component and result into the aerodynamic damping matrix $\mathbf{C}_{aero}$ and the aerodynamic stiffness matrix $\mathbf{K}_{aero}$. Here, the velocity triangle in the steady state is inserted with the components of U_0, as shown in Fig. 7.4 on the right

$$U_{0x} = \Omega\,(r_h + z)\cos(\gamma_c), \quad U_{0y} = W\cos(\gamma_c) \tag{7.14}$$

For simplicity in the derivation of the governing model, the induction is neglected in the upper equation. All resulting matrices can be found in Appendix 7.4.
From the upper equations (Eq. (7.2), Eq. (7.3) Eq. (7.8), Eq. (7.13)) a system matrix A can be defined as

$$\mathbf{A} = \begin{bmatrix} \mathbf{0} & \mathbf{I} \\ \mathbf{M}^{-1}\,(\mathbf{K}_{struc} + \mathbf{K}_{aero}) & \mathbf{M}^{-1}\,(\mathbf{C}_{aero}) \end{bmatrix} \tag{7.15}$$

Where $\mathbf{M}$ is the mass matrix, $\mathbf{K}_{struc}$ and $\mathbf{K}_{aero}$ are the structural and aerodynamic stiffness matrix, $\mathbf{C}_{aero}$ is the aerodynamic damping matrix and $\mathbf{I}$ is the identity matrix. The real parts of the eigenvalues of the upper system matrix (Eq. (7.15)) determine the damping of the system.
A steady simple BEM-code (referred to as the "simple BEM-code") is used in Matlab (R2018a), to determine the force coefficients along the blade span and to include the induction in the inflow velocity on the airfoil. The simple BEM-code does not include skewed inflow models due to yaw or tilt. The induction is calculated along the rotor radius only, since there is no dependency of the induction on the azimuth position. The structural stiffness of the tower is tuned to account for the neglected mass distribution of the tower. Eigenanalysis of the system matrix is performed in Matlab over a range of wind speeds, and the real parts of the eigenvalue of the yaw mode are evaluated.
For the turbine configuration with the original cone, length and mass distribution, the 2DOF model is imitated in the aeroelastic modal analysis tool HAWCStab2, described by Hansen (2004). Stiff turbine components are modelled, except the tower side-side bending and the yaw bearing is free to rotate. The real parts of the eigenvalues are compared to validate the results from the 2DOF model.
The validated model is used for a parameter study to investigate the influence of geometrical turbine parameter on the real part of the yaw mode eigenvalue. The varied parameter are the cone angle, the shaft length and the position of the center of gravity of the nacelle along the shaft.
Finally, HAWCStab2 is used to investigate if the stability limit of the yaw mode would occur within the normal operational wind speed range of the turbine and which further degree of freedom, additional to the tower side-side and yaw, would be needed to predict instability.

7.3 Results

The following section shows the results for the equilibrium yaw angle and the stability of the yaw mode are discussed.

7.3.1 Equilibrium yaw angle

Figure 7.6 shows the comparison of the equilibrium yaw angle found by HAWC2 and the equilibrium yaw angle found from the BEM-code (Fig.7.5), over the wind speed for the original turbine configuration with 5° tilt and 3.5° cone. The

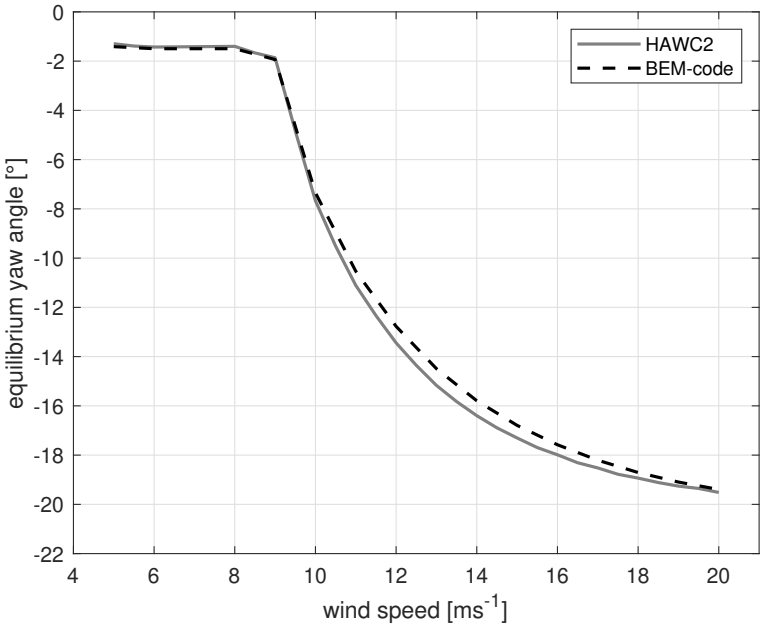

Figure 7.6: Comparison of the equilibrium yaw angle over wind speed from HAWC2 and the BEM-code for the original turbine configuration with 5° tilt and 3.5° cone.

figure shows that the equilibrium angle is not zero. The equilibrium yaw angle is constant at -1.4° from cut-in wind speed up to 8 ms^{-1}. Between 8 ms^{-1} and below rated wind speed (9 ms^{-1}) the equilibrium yaw angle decreases slightly

to -1.8°. For wind speeds higher than the rated wind speed (9.5 ms^{-1}), the equilibrium yaw angle decreases strongly. The slope of the equilibrium yaw angle over wind speed changes so that the equilibrium yaw angle shows a tendency to asymptotically reach a minimum. The lowest observed equilibrium yaw angle of -19.4° is reached at 20 ms^{-1}. The equilibrium yaw angle calculated by HAWC2 and with the BEM-code differ with a maximum of 0.6° at around 13 ms^{-1}.
The analysis shows that there will be a yaw moment even with a perfect alignment of the rotor with the wind direction, which drives the rotor to the non-zero equilibrium angle. This yaw moment is due to the tilt angle. Including a tilt angle has two effects: aerodynamically, the projection of the global wind speed leads to a yaw moment as illustrated in Fig. 7.1. Structurally, the tilt leads to a yaw moment as the torque axis is not perpendicular to the yaw axis and the torque M_Q is projected to the yaw axis with $\sin(\delta)M_Q$. While the structural effect follows the torque curve, the aerodynamic effect is influenced by the rotor speed and increases with the wind speed. When the rotor is free to align with the wind direction, the moment due to tilt pushes the rotor to a non zero yaw position. At a non zero yaw position a restorative yaw moment is present due to yaw stiffness (see Fig. 7.2). The rotor finds a new equilibrium yaw angle. As the equilibrium yaw angle between HAWC2 and the BEM-code agree well; the BEM-code is therefore used for the parameter study.
Figure 7.7 shows the equilibrium yaw angle (a) and the relative power production (b) in dependency on the tilt angle and wind speed. A zero tilt angle will give a zero equilibrium yaw angle, which means a full alignment of the rotor with the wind direction. Negative tilt angles show a positive equilibrium yaw angle and positive tilt angles show a negative equilibrium yaw angle. The dependency of the equilibrium yaw angle on the tilt angle is stronger for higher wind speeds. The relative power difference shows the highest losses for extreme tilt angles and high wind speeds. There is zero relative power difference at zero tilt angle.
There is no yaw moment for yaw alignment of the rotor plane with the wind direction if there is a zero tilt angle. As a yaw moment due to a tilt angle is dependent on the sine of the tilt angle, the equilibrium yaw angle is anti-symmetric around the line of full alignment (0°). With larger tilt angles, a larger yaw moment is created aerodynamically and structurally. The larger yaw moment drives the rotor to larger equilibrium yaw angles, where a counter acting yaw moment is created from imbalance of forces by the induction variation and wind speed projections from yaw and cone angle. The power production shows the expected behaviour for a non perpendicular inflow to the rotor plane. The higher the equilibrium yaw angle, the lower the wind speed component perpendicular to the rotor plane, the lower the power production, and the higher the difference to the reference power curve.
Figure 7.8 shows the equilibrium yaw angle (a) and the relative difference in power

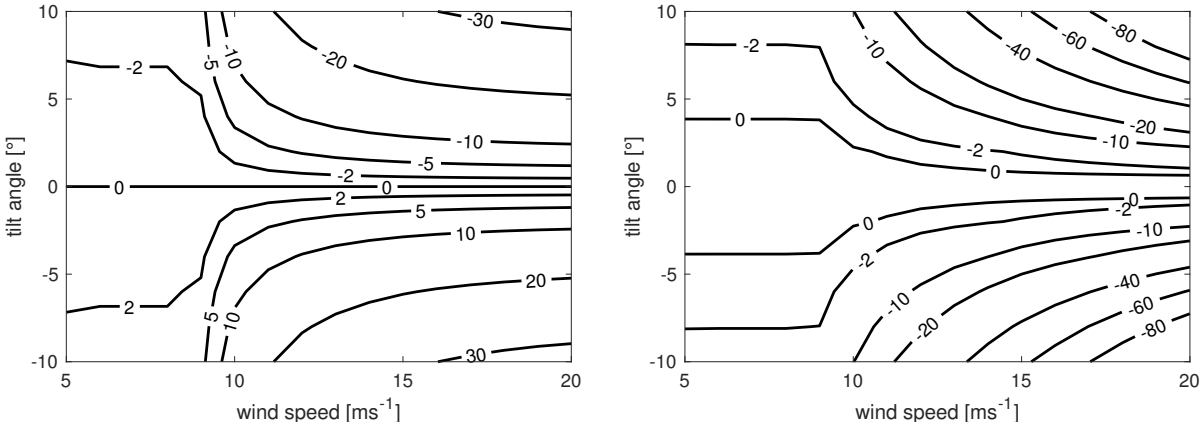

(a) Equilibrium yaw angle [°] (b) Power difference [%]

Figure 7.7: Equilibrium yaw angle (a) and the relative difference in power production (b) in dependency of tilt angle and wind speed variation for a turbine configuration with 3.5° cone. The relative, difference in power is compared at each calculation point relative to the power production of the original turbine, with a forced yaw alignment.

production (b) for the variation of cone and wind speed. The figure is stitched together at the grey line, as the calculated data showed an inconsistency. Here the angles tend to increase to very large positive and negative angles, rather than decrease to zero as a continuous figure would suggest. Figure 7.8 (a) shows that cone angles higher than 0° give a negative equilibrium yaw angle, while cone angles lower than -2.5° give a positive equilibrium yaw angle. It can also be seen that highly positive, as well as highly negative cone angles give equilibrium yaw angles closer to zero and a smaller variation of the equilibrium yaw angle over wind speed. The higher the wind speed and the closer the wind speed to the stitching line, the larger positive or negative are the calculated equilibrium yaw angles. Figure 7.8 (b) shows that the extreme equilibrium yaw angles come with an extreme power loss. The negative cone angles combined with the positive equilibrium yaw angles at low wind speed are associated with a higher power loss, than the combination of negative equilibrium yaw angles and positive cone angles.

Varying the cone angle for the tilted turbine configuration has an effect on the torque. A larger cone angle reduces the torque, which leads to a reduced projected yaw moment due to the tilt $M_{Q,\delta}$. The aerodynamic moment $M_{W,\delta}$ due to tilt

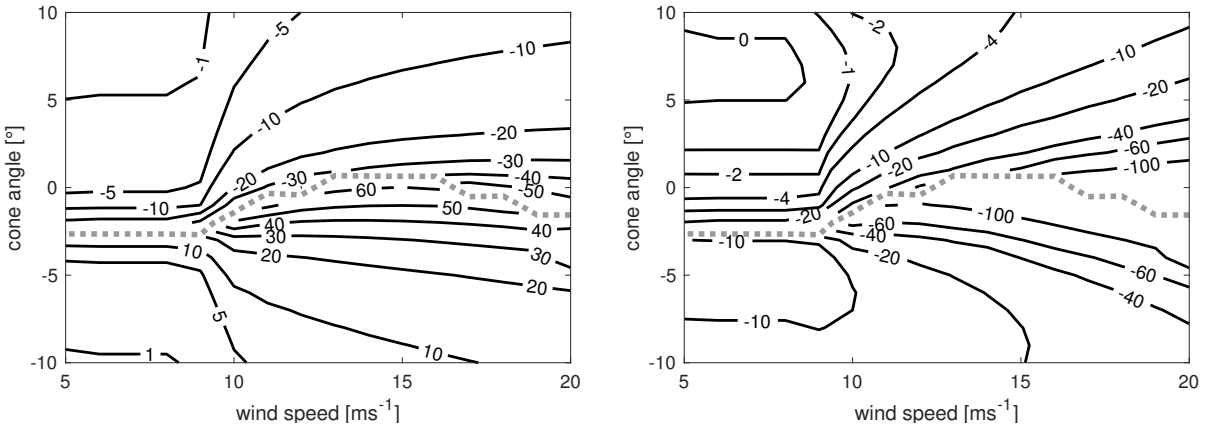

(a) Equilibrium yaw angle [°] (b) Power difference [%]

Figure 7.8: Equilibrium yaw angle (a) and the relative difference in power production (b) in dependency of cone angle and wind speed variation for a turbine configuration with 5° tilt. The figure is stitched together from two sub-figures at the grey line.

on the other hand is hardly influenced. Further, larger cone angles increase the yaw moment due to yawed inflow on the coned rotor M_{W,θ,γ_c} (see Fig. 7.2 (e)). Thus, for larger positive cone angles a smaller equilibrium angle is found, not just due to the increased stiffness from cone but also due to a smaller moment from the tilt angle $M_{Q,\delta}$. For larger negative cone angles, the moment due to coned and yawed inflow is only counteracting the moments due to tilt, if the rotor is aligned with a yaw error of the opposite sign. Otherwise the stiffness from yawed and coned inflow would be negative and the force would not be restorative (see Fig. 7.2 (e)). As the stiffness for yawed and coned inflow is becoming very small for small cone angles, the yaw moment due to tilt has to be balanced by the moment due to induction variation M_a (see Fig. 7.2 (a)) and due to yawed inflow $M_{W,\theta}$ (see Fig. 7.2 (c)). As the two moments M_a and $M_{W,\theta}$ need larger yaw angles to create a significant yaw moment, the equilibrium yaw angle becomes large for small cone angles (compare Fig. 7.2 (b,d,f)). Due to three dimensional effects of the wind speed projection the aerodynamic yaw moment due to tilt $M_{W,\delta}$ is not symmetric for cone angles around zero. Compared to the estimated yaw moment of the airfoil at $R = 0.75\%$ for 16 ms^{-1} and 5° tilt in Fig. 7.1, the difference between a positive and a negative cone angle ($\pm 0.5°$) is around 12%. As a sum the total yaw moment due to tilt is slightly different for negative and

positive cone angles, the asymmetry in Fig. 7.8 is observed. Since the equilibrium yaw moment is not symmetric around zero, the negative cone angles combine with higher positive equilibrium yaw angles, so there is a higher power loss for negative cone angles than for positive cone angles.
Figure 7.9 shows the equilibrium yaw angle (a) and the relative power difference (b) over wind speed and the shaft length factor. This factor is directly multiplied with the shaft length to in- or decrease the absolute shaft length. Figure 7.9 (a)

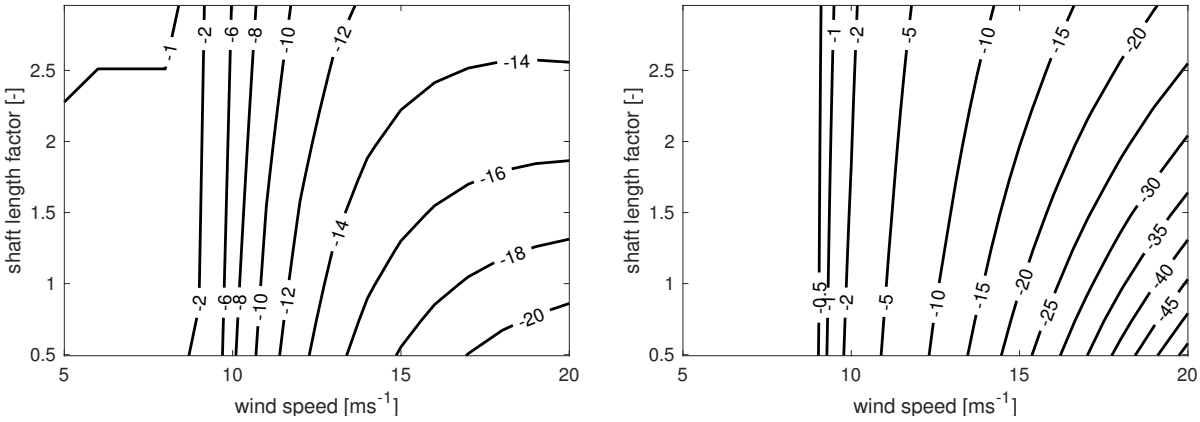

(a) Equilibrium yaw angle [°] (b) Power difference [%]

Figure 7.9: Equilibrium yaw angle (a) and the relative difference in power production (b) in dependency of shaft length and wind speed variation for a turbine configuration with 5° tilt and 3.5° cone. The relative, difference in power is compared at each calculation point relative to the power production of the original turbine, with a forced yaw alignment.

shows that the shaft length factor has nearly no influence on the equilibrium yaw position for low wind speeds. Only for high wind speeds above rated power, the equilibrium yaw angle is higher for smaller shaft length factors than for small shaft length factors. As shown on the right, the relative difference in power is hardly influenced by the shaft length factor. Only for high wind speeds less power loss is observed for higher shaft length factors than for lower shaft length factors. As discussed previously the shaft length acts as the moment arm for the summed in-plane shear forces on the hub. For the in-plane shear forces to be significantly large a large yaw angle and high wind speeds are required to create an imbalance on the angle of attack between the upper and the lower rotor half (see Fig. 7.2

(c)). Only in this case the moment created from the force at the hub and the shaft length as the moment arm is large enough to counter act partly the moment created by the tilt angle. However, within the range of investigated wind speeds, the yaw misalignment with the wind direction is still so large, that hardly any power difference can be recovered by the investigated increase in shaft length.

7.3.2 Dynamic stability of the free yaw mode

The following section discusses the stability of the free yaw mode of the turbine for a tilt angle of 0° and 3.5° cone. The free yaw motion is stable around the equilibrium point, if it is positively damped, which means that the real part of the two eigenvalues for the yaw mode are negative. Figure 7.10 shows the comparison of the real parts of the eigenvalue of the yaw mode of the analytic 2DOF-model and the imitation in HAWCStab2. It can be seen at the top of the figure that

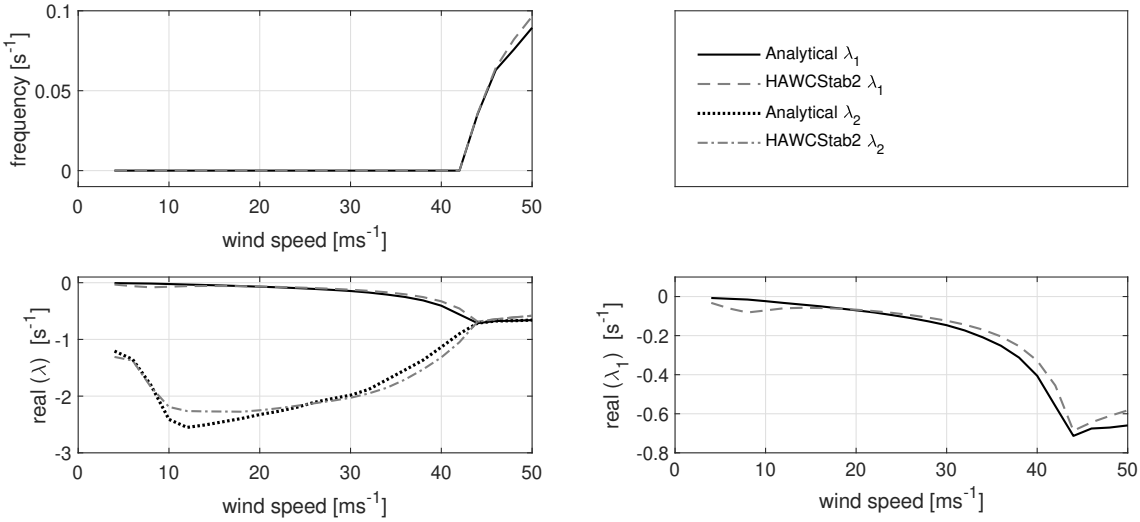

Figure 7.10: Comparison of the frequency (top left), the real part of the two eigenvalues (bottom left) and a zoom into the first eigenvalue (bottom right) of the yaw mode for the 2DOF model from the analytic solution, and the imitation in HAWCStab2.

there is a yaw frequency of zero up to a wind speed of 42 ms^{-1}. For higher wind

speeds, the frequency is increasing up to 0.9 s^{-1} at 50 ms^{-1} for the solution from HAWCStab2. The results of the analytic 2DOF model and the imitation in HAWCStab2 differ maximum 0.01 s^{-1} in the computation of the frequency of the free yaw mode. At the bottom of the figure, the real parts of the complex pair of eigenvalues is displayed on the left, and a zoom for the real part of the first eigenvalue is displayed on the bottom right. The real part of the first and second eigenvalue are equal only for non-zero frequencies. The first eigenvalue is generally closer to zero than the second eigenvalue for wind speeds below 44 ms^{-1}. The first eigenvalue decreases for wind speeds up to 8 ms^{-1}. The slope of the eigenvalue over wind speed changes for wind speeds above rated power. The second eigenvalue decreases to a minimum at 10 ms^{-1} (HAWCStab2) and at 12 ms^{-1} (Analytical 2DOF model). For higher wind speeds the second eigenvalue increases. The total eigenvalue increases for wind speeds of 44 ms^{-1} and higher. For any negative real part of the eigenvalue and zero frequency (wind speeds below 44 ms^{-1}), a small displacement will initiate the motion back to the equilibrium point without oscillation (convergence). For wind speeds of 44 ms^{-1} and higher, there will be an oscillatory motion that will decrease in amplitude until the rotor aligns with at the equilibrium position. The difference between the solution of HAWCStab2 and from the analytical model is up to 0.08 s^{-1} for the first eigenvalue and up to 0.5 s^{-1} for the second eigenvalue. The analytical 2DOF model and the imitation in HAWCStab2 cannot be expected to give the same results, since the HAWCStab2 model includes the rolling motion of the nacelle and the motion of the distributed tower mass instead of a lumped point mass. However, the real parts of the first eigenvalues of the two models are close so that the analytical model can be used for the parameter study. The results of the parameter study will be sufficient to identify the parameters that stabilize or destabilize the free yawing motion of the turbine.

Including the aerodynamic forces to the mechanical system has two effects. Firstly, there is an aerodynamic stiffness, due to the mechanisms of wind speed projection as shown in Fig. 7.2. The effect of induction variation is negligible for small yaw angles. Secondly, the yaw motion creates a flow velocity that is added to the wind speed on one side of the rotor and subtracted from the wind speed on the other side of the rotor (Fig. 7.3), which again changes the angle of attack and therefore the aerodynamic forces create a moment, which dampens the yaw motion.

The main influence can be observed from the slope of the lift coefficients, if the outputs from the simple BEM-code are manually manipulated for the eigenanalysis. As the yaw moment for moderate pitch angles is dominated by the flapwise forces, the drag and the slope of the drag coefficient are of minor influence. As the projection of the forces changes with the pitch angle, a clear dependency on the wind speed can be observed and also the change in the slope of the real part of

the eigenvalue can be observed at the rated wind speed. Further, the operational point changes so the force coefficients and their slopes are expected to change the eigenvalues over wind speed.
Figure 7.11 shows the real parts of the first (a) and of the second (b) eigenvalue over the variation of cone angle and wind speed. The figure shows that the real

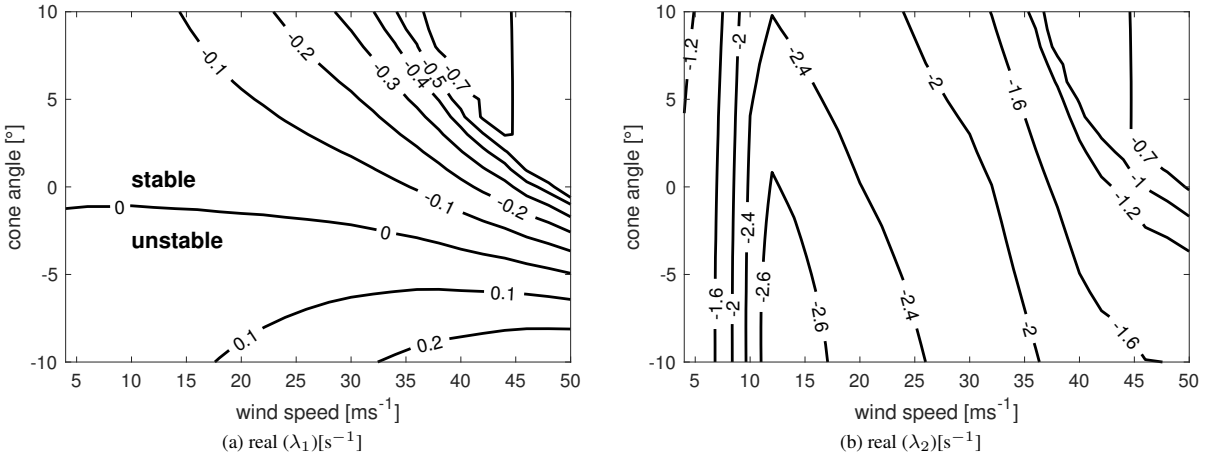

Figure 7.11: Real part of the first (a) and second (b) eigenvalue of the yaw mode for a variation of cone angle and wind speed from the 2DOF model.

part of the first eigenvalue changes the sign and becomes positive for cone angles of -1° at 4 ms^{-1} and -5° at 50 ms^{-1}. Thus, the zero equilibrium position becomes unstable for these negative cone angles. It can also be seen that large positive cone angles decrease the real part of the first eigenvalue and therefore increase the damping. The larger the wind speed, the larger the effect of variation of the cone angle on the real part of the first eigenvalue. The real part of the second eigenvalue is influenced less than the real part of the first eigenvalue and varies mainly with wind speed. For very high cone angles, the minimum real part is slightly increased by 0.2 s^{-1} at around 14 ms^{-1}. Extremely high wind speeds, larger than 40 ms^{-1} show an increase of the real part of the second eigenvalue for very high cone angles. The imaginary part in the unstable region is zero, indicating a divergence instability. In the stable region, the imaginary part of the eigenvalues is the same for high wind speeds (higher 42 ms^{-1}) and high cone angles which means that there is a positively damped oscillatory yaw motion (flutter).

The cone angle affects mainly the aerodynamic stiffness, as shown in Fig. 7.2. The damping is hardly effected. However, as discussed previously, the negative cone angles can create a negative stiffness driving the system away from the equilibrium position. A positive damping coefficient in the damping matrix cannot restore the equilibrium position in this case and the real part of the eigenvalue becomes positive. As high velocities create a positive stiffness component from the in-plane forces and due to the shaft length, the instability occurs not at zero cone angle and can tolerate slightly more negative cone angles at high wind speeds.
Figure 7.12 shows the real part of the first (a) and second (b) eigenvalue over a variation of wind speed and shaft length. It can be seen that the real parts

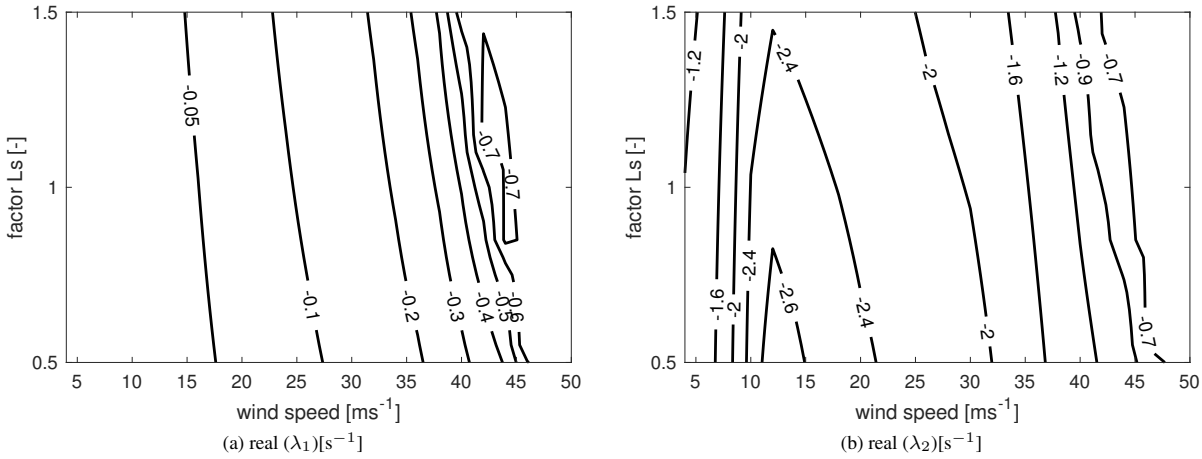

Figure 7.12: Real part of the first (a) and second (b) eigenvalue of the yaw mode for a variation of shaft length and wind speed from the 2DOF model.

of the eigenvalues hardly change with the variation of the shaft length. A lower shaft length slightly increases the real part of the eigenvalue. High shaft length slightly decrease the minimum of the second eigenvalue at around 14 ms^{-1}.
Large shaft length can increase the projected wind speed for the damping term, as the center of rotation is far away from the rotor plane. However, as realistic values of the shaft length are always much lower than the blade length, the influence on the damping is very low. Also the influence on the stiffness can hardly be observed, as the effect of in plane forces is very small for small yaw angles (linearization point of 0° yaw). Overall, this leads to the fact that the eigenvalue of the yaw mode is hardly influenced by the shaft length within the investigated

range.
A figure for the real parts of the eigenvalue changing with the position of the center of gravity is not shown. The distance of the center of gravity only effects the rotational inertia for the yaw motion. As the stiffness and damping are not effected, the real part of the eigenvalues are hardly changing from eigenanalysis of the system matrix.
Figure 7.13 shows the frequency at the top and at the bottom the real part of the first eigenvalue of the free yaw mode from HAWCStab2 over wind speeds. In the figure the 2DOF imitation, the extension of the 2DOF imitation with flapwise blade flexibility, the extended 2DOF model with updated steady state (deformed blade including prebend) and the full turbine model are compared. The figure shows, that the frequency is zero for all models within the investigated wind range. The figure shows at the bottom the characteristic behaviour of the real part of the eigenvalue of the 2DOF model imitation with HAWCStab2, already compared in Fig. 7.10. It can be seen that including the flapwise flexibility increases the real part of the eigenvalue significantly, especially for high wind speeds. The real part does not become positive for the investigated wind speed range due to the flapwise flexibility, as long as the steady state is not updated. The figure shows further that the real part of the eigenvalue of the yaw mode becomes positive for the 2DOF model imitation including flapwise flexibility for wind speeds of 19 $ms^{-1}$and higher, if the linearization is performed around the deformed steady state, including prebend (updated steady state). The real part of the eigenvalue of the free yaw mode calculated from the full turbine model differs maximum 0.005 s^{-1} from the real part of the eigenvalue calculated from the extended 2DOF imitation with updated steady state.
Flapwise flexibility introduces the flapwise motion of the blades. The asymmetric flapwise motion of the foreward and backward whirling mode could be stabilizing or destabilizing the yaw equilibrium, depending on the phase difference between the yaw motion and the asymmetric flapwise motion. The phase difference between the flapwise modes an the free yaw mode is observed to be around 180°. As the flapwise motion is counter acting the yaw motion, it will decrease the damping term. Flapwise flexibility further changes the effective static cone of the system (updated steady state). Prebend and bending of the blades towards the tower due to negative lift at high pitch angles, decrease the effective cone of the rotor. As the effective cone due to blade deflection becomes negative, a divergence instability of the zero yaw equilibrium is observed. Simulations of time series with HAWC2 show that the turbine finds a new yaw equilibrium angle at at yaw error of around 60°. Including the flapwise flexibility and the linearization around the deformed steady state would be sufficient to investigate the dynamics of the free yawing downwind turbine, as the difference in the real part between the full turbine model is negligible.

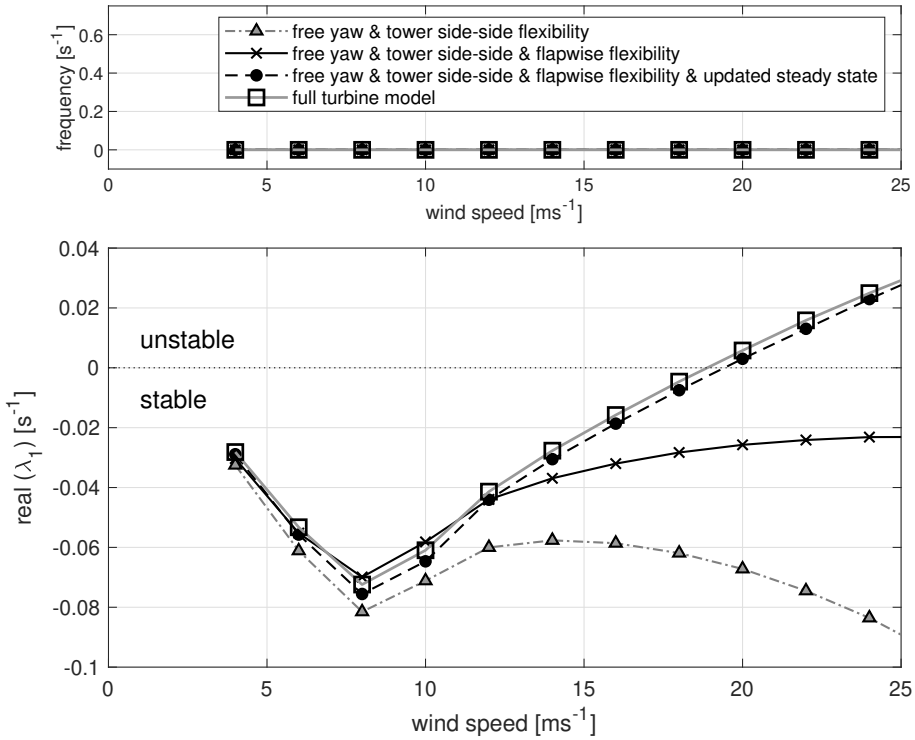

Figure 7.13: Comparison of the frequency (top) and real part of the first eigenvalue (bottom) of the yaw mode, for the imitation of the 2DOF model, the model containing additionally the blade flapwise flexibility, the model with the additional blade flapwise flexibility and the linearization around the deformed steady state and the full turbine model with a linearization around the deformed steady state and updated operational data from HAWCStab2.

7.4 Conclusions

The free yawing behaviour of the Suzlon S111 2.1 MW turbine in a downwind configuration has been investigated. A BEM-code has been used to show the equilibrium yaw angle and the parameters creating a yaw loading on the rotor. A small analytical model with only two degrees of freedom has been developed. It has been used for a fast overview and understanding the of parameters influencing the stability of the passive yaw equilibrium position, exemplified on the Suzlon turbine.

It has been seen that the original tilt angle of 5° introduces a yaw misalignment of up to -19.4° coming with a power loss of more than 20%. The tilt angle was seen to introduce a structural yaw moment from the torque projection and an aerodynamic yaw moment from the wind speed projection, as also observed by Eggleston and Stoddard (1987), Corrigan and Viterna (1982) and Hansen (1992). Only with a tilt angle of 0° this could be fully eliminated. However, the analysis did not include any inclination angle of the wind field or wind shear, which would also introduce an aerodynamic yaw moment from wind speed projection. A yaw angle due to inclination or shear will introduce a dependency of the yaw alignment on the varying environmental conditions.

The yaw misalignment introduces a restoring yaw moment from the flapwise blade moments due to induction variation over the rotor plane. This restoring yaw moment can be increased with an increasing cone angle, as the combination of cone and yaw angle creates a favorable wind speed projection and therefore increases the yaw stiffness as predicted by Eggleston and Stoddard (1987). This result confirms the observations of the measurements from for example Verelst and Larsen (2010) and Kress et al. (2015).

With a significantly large yaw angle, the wind speed projection leads to a in-plane force imbalance that increases the restoring yaw moment. In conclusion, an in-plane force due to load imbalance will also be created from the tower shadow and wind shear. In contrast to the previous effect, this force imbalance will also exist when the rotor is fully aligned with the wind direction and it will vary with varying wind conditions. Such a negative effect from vertical wind shear and tower shadow has already been observed for example by Hansen (1992).

The eigenanalysis of a 2DOF model of the turbine without tilt angle has been conducted. It has been observed that the cone angle can significantly increase the real part of the eigenvalue of the yaw mode and therefore stabilize the yaw equilibrium as it increases a positive stiffness term. It has further been observed that a too small cone angles can give a negative stiffness term and therefore leads to a positive real part of the eigenvalue and an instability in the yaw mode.

Modelling the free yawing motion with 2DOF has been seen to be not sufficient,

as flapwise blade motion changes the stiffness and the damping of the free yaw mode. The comparison with HAWCStab2 showed that flapwise blade flexibility significantly increases the real part of the eigenvalue and destabilized the yaw equilibrium. The phase difference between yaw and asymmetric flapwise blade mode decreases significantly the damping of the free yaw mode. The stiffness is mainly influenced by flapwise blade deformation as the steady state blade deflection decreases the effective cone angle.
Over all, this analysis showed clearly that the S111 turbine in downwind configuration will not align with the wind direction and the power loss is significant. Further, changing wind conditions such as inclination angle or wind shear will lead to a yaw misalignment that will change with the environmental conditions. As the free yaw mode further becomes unstable for high wind speeds, it will not be possible to run the S111 in a free yawing downwind configuration. Stabilizing the free yaw mode and increasing the alignment with high cone angles might be possible. Yaw bearings could potentially be designed for a lower yaw load. Yaw drives will always be needed as a cable unwinding mechanism. Since there will be a power loss associated with either a yaw misalignment or a larger cone angle it is highly doubtful that the passively free yawing downwind turbine can be a more cost efficient solution than a yaw controlled downwind turbine in terms of levelized cost of energy.

Bibliography

Corrigan, R. and Viterna, L. (1982). free yaw performance of the mod-0 large horizontal axis 100kw wind turbine. *NASA-Report*, TM-83(19235):103–122.

Eggleston, D. M. and Stoddard, F. S. (1987). Yaw stability, in: Wind turbine engineering design. *Van Nostrand Reinhold Company Inc., New York, USA, 205-211.*

Glasgow, J. and Corrigan, R. (1983). Results of free yaw test of the mod-0 100-kilowatt wind turbine. *NASA Report*, TM-83432:1–16.

Hansen, A. C. (1992). Yaw dynamics of horizontal axis wind turbines. *NREL-Report; No. TP-442-4822.*

Hansen, A. C., Butterfield, C. P., and Cui, X. (1990). Yaw loads and motion of a horizontal axis wind turbine. *Journal of Solar Energy Engineering; Vol. 112; p. 310-314.*

Hansen, A. C. and Cui, X. (1989). Analysis and observation of wind turbine yaw dynamics. *Journal of Solar Energy Engeneering; Vol. 111; p. 367-371.*

Hansen, M. (2004). Aeroelastic stability analysis of wind turbines using an eigenvalue approach. *Wind Energy*, 7:113–143. https://doi.org/10.1002/we.116.

Hansen, M. H. (2003). Improved modal dynamics of wind turbines to avoid stall-induced vibrations. *Wind Energy; Vol. 6; p. 179-195.* https://doi.org/10.1002/we.79.

Hansen, M. H. (2016). Modal dynamics of structures with bladed isotropic rotors and its complexity for two-bladed rotors. *Wind Energy Science; Vol. 2; p. 271-296.* https://doi.org/10.5194/wes-1-271-2016.

Kress, C., Chokani, N., and Abhari, R. (2015). Downwind wind turbine yaw stability and performance. *Renewable Energy; Vol. 83; p. 1157-1165.* https://doi.org/10.1016/j.renene.2015.05.040.

Larsen, T. and Hansen, A. (2014). How 2 hawc2, the user's manual. *Risø-Report:Risø-Report*, R1597(verion 4-5):1–147.

Madsen, H. A., Riziotis, V., Zahle, F., Hansen, M. O. L., Snel, H., Grasso, F., Larsen, T. J., Politis, E., and Rasmussen, F. (2011). Blade element momentum modelling of inflow with shear in comparison with advanced model results. *Wind Energy; Vol. 15; p. 63-81.* https://doi.org/10.1002/we.493.

Madsen, P. H. and McNerney, G. M. (1991). Frequency domain modelling of free yaw response of wind turbines and turbulence. *Journal of Solar Energy Engineering; Vol. 113; p. 102-103.*

Olorunsola, O. (1986). On the free yaw behaviour of horizontal axis wind turbines. *Energy Research; Vol. 10; p. 343-355.*

Pesmajoglou, S. D. and Graham, J. M. R. (2000). Prediction of aerodynamic forces on horizontal and axis wind turbines in free yaw and turbulence. *Journal of Wind Engineering and Industrial Aerodynamics; Vol. 86; p. 1-14.*

Picot, N., Verelst, D. R., and Larsen, T. J. (2011). Free yawing stall-controlled downwind wind turbine with swept blades and coned rotor. *In Proceedings; European Wind Energy Association.*

Verelst, D., Larsen, T. J., and van Wingerden, J. W. (2016). Open access wind tunnel measurements of a downwind free yawing wind turbine. *Journal of Physics: Conference Series 753; p.1-12.* https://doi.org/10.1088/1742-6596/753/7/072013.

Verelst, D. R. and Larsen, T. J. (2010). Yaw stability of a free-yawing 3-bladed and downwind wind turbine. *EAWE PhD Seminar.*

Appendix A: List of Symbols

Table 7.1: List of Symbols

Symbol		Symbol		Symbol	
α	angle of attack	c	chord length	M_B	bending moment
β_p	pitch angle	C_L,C_D,	force coefficients	m_{Na},m_b,m_h	mass (nacelle, blade, hub)
γ_c	cone angle	C_n,C_T		Q_i	external forces
δ	tilt angle	F, f	force, force components	R	total rotor radius
θ	yaw angle	I	rotational inertia	r	local radius
λ	eigenvalue	$\mathbf{K}$	stiffness matrix	T	kinetic energy
ρ	air density	k_x	tower side-side stiffness	t	time
ϕ	inflow angle	L	Lagrangian	T_x,T_y	shear forces
ψ	azimuth position	L_{cg},L_s	distances from yaw axis	U	inflow velocity
Ω	rotational speed		(center of gravity, shaft)	u_x	tower displacement
ω	eigenfrequency	$\mathbf{M}$	mass matrix	V	potential energy
$\mathbf{A}$	system matrix	M_a,$M_{Q,\delta}$,	yaw moment contributions	W	wind speed
a	induction	$M_{W,\delta}$,$M_{W,\gamma_c,\theta}$,		W_{ind},W_{grid}	velocity (induced, at grid point)
$\mathbf{C}$	damping matrix	$M_{W,\theta}$		$\mathbf{x}$	displacement

Appendix B: Matrices for the 2DOF model

The mass matrix results into

$$\mathbf{M} = \begin{bmatrix} 3\left(\int_0^R m_b(z)dz\right) + 3m_h + m_{Na} & M_{12} \\ M_{21} & M_{22} \end{bmatrix} \tag{7.16}$$

where the coupling term between the tower side-side motion and the nacelle yaw are

$$M_{12} = M_{21} = -3\left(\int_0^R m_b(z)(L_s + \sin(\gamma_c)z)dz\right) - 3m_h L_s - m_{Na}L_{cg} \tag{7.17}$$

and the mass element for the yaw motion is

$$\begin{aligned} M_{22} = \frac{3}{2}\int_0^R m_b(z)\left(-\cos(\gamma_c)^2 z^2 + 4L_s\sin(\gamma_c)z + 2r_h\cos(\gamma_c)z\right. \\ \left. +2L_s^2 + rh^2 + 2z^2\right)dz \\ +\frac{3}{2}m_h r_h^2 + 3L_s^2 m_h + m_{Na}L_{cg}^2 + I_z \end{aligned} \tag{7.18}$$

The resulting stiffness matrix is

$$\mathbf{K} = \begin{bmatrix} k_x & 0 \\ 0 & G_z \end{bmatrix} \tag{7.19}$$

In the stiffness matrix the spring stiffness can be found on the diagonal, while there is no coupling from the stiffness in the off diagonal elements.
The mass matrix on the other hand is fully populated. On the first element is the total mass of the turbine that will be moved with the tower side-side motion. On the second diagonal element there is the mass moment of inertia for the rotation around the yaw center. This includes the mass moment of inertia of blades, hub and nacelle-shaft assembly, as well as their respective Steiner-radius to the center of rotation. The coupling terms on the off-diagonal the mass elements times the respective radius to the rotational axis.

Aerodynamic Matrices

The resulting stiffness matrix $\mathbf{K}_{aero}$ is only populated in the second column with a coupling term from the tower side-side motion and an aerodynamic stiffness

term for the yaw motion.

$$\mathbf{K}_{aero} = \frac{1}{4} c\rho W^2 \int_0^R \begin{bmatrix} 0 & K_{12,aero} \\ 0 & K_{22,aero} \end{bmatrix} dz \tag{7.20}$$

The coupling coefficient $K_{12,aero}$ from the tower motion to yaw motion is

$$\begin{aligned} K_{12,aero} &= 12C_{y0}\cos(\gamma_c)^3 + 3\lambda\left(C'_{y0} - C_{x0}\right)\cos(\gamma_c)^2 \\ &+3\left(2\lambda^2 C_{y0} - C'_{x0} - 3C_{y0}\right)\cos(\gamma_c) + 3\lambda\left(3C_{x0} - C'_{y0}\right) \end{aligned} \tag{7.21}$$

and the aerodynamic yaw coefficient is

$$\begin{aligned} K_{22,aero} &= -6L_s C_{y0}\cos(\gamma_c)^3 \\ &+ \left[6r_h C_{y0}\sin(\gamma_c) + 3\lambda L_s\left(C_{x0} - C'_{y0}\right)\right]\cos(\gamma_c)^2 \\ &+ \left[\left(3\lambda r_h\left(C'_{y0} - C_{x0}\right)\right.\right. \\ &\left.\left.+3z\left(3C_{y0} + C'_{x0}\right)\right)\sin(\gamma_c) + 3L_s\left(3C_{y0} + C'_{x0}\right)\right]\cos(\gamma_c) \\ &- 3\lambda\left(L_s + sin(\gamma_c)z\right)\left(3C_{x0} - C'_{y0}\right) \end{aligned} \tag{7.22}$$

The aerodynamic damping matrix $\mathbf{C}_{aero}$ is symmetric and fully populated.

$$\mathbf{C}_{aero} = \frac{1}{8} c\rho W \begin{bmatrix} C_{11,aero} & C_{12,aero} \\ C_{21,aero} & C_{22,aero} \end{bmatrix} \tag{7.23}$$

with the aerodynamic tower side-side coefficient

$$\begin{aligned} C_{11,aero} &= -12C_{y0}\cos(\gamma_c)^3 + 6\lambda\left(C_{x0} - C'_{y0}\right)\cos(\gamma_c)^2 \\ &+6\left(C'_{x0} + 3C_{y0}\right)\cos(\gamma_c) + 6\lambda\left(C'_{y0} - 3C_{x0}\right) \end{aligned} \tag{7.24}$$

The aerodynamic coupling coefficients $C_{12,aero} = C_{21,aero}$ wich is $C_{21,aero} = -2K_{22,aero}$

$$\begin{aligned} C_{12,aero} &= 12L_s C_{y0}\cos(\gamma_c)^3 \\ &+ \left[-12r_h C_{y0}\sin(\gamma_c) - 6\lambda L_s\left(C_{x0} - C'_{y0}\right)\right]\cos(\gamma_c)^2 \\ &+ \left[\left(6\lambda r_h\left(C_{x0} - C'_{y0}\right) - 6z\left(3C_{y0} + C'_{x0}\right)\right)\sin(\gamma_c)\right. \\ &\left.-6L_s\left(3C_{y0} + C'_{x0}\right)\right]\cos(\gamma_c) \\ &+ 6\lambda\left(L_s + z\sin(\gamma_c)\right)\left(3C_{x0} - C'_{y0}\right) \end{aligned} \tag{7.25}$$

The aerodynamic damping coefficient of the yaw motion is

$$\begin{aligned} C_{22,aero} &= \left(12\left(r_h^2 - L_s^2\right)C_{y0} - 6z^2\left(C'_{x0} + C_{y0}\right)\right)\cos(\gamma_c)^3 \\ &+ \left[24L_s r_h \sin(\gamma_c)C_{y0} + \left(6L_s^2\left(C_{x0} - C'_{y0}\right) + 12z^2 C_{x0}\right.\right. \\ &\left.\left. -6\lambda r_h^2\left(C_{x0} - C_{y0}\right)\right) + 24r_h z C_{y0}\right] cos(\gamma_c)^2 \\ &+ \left[12L_s\left(z\left(3C_{y0} + C'_{x0}\right) - \lambda r_h\left(C_{x0} - C'_{y0}\right)\right)\sin(\gamma_c)\right. \\ &\left. -12\lambda r_h z\left(C_{x0} - C'_{y0}\right) + \left(6\left(L_s^2 + z^2\right)\left(3C_{y0} + C'_{x0}\right)\right)\right]\cos(\gamma_c) \\ &+ 6\lambda\left(L_s^2 + 2L_s z\sin(\gamma_c) + z^2\right)\left(C'_{y0} - 3C_{x0}\right) \end{aligned} \tag{7.26}$$

Where the subscript 0 indicates the steady state values. The substitutes in the matrix coefficient have the following definitions for the tangential C_{x0} and the normal force C_{y0} coefficient

$$C_{x0} = C_{L0}\sin(\phi_0) - C_{D0}\cos(\phi_0) \tag{7.27}$$

and

$$C_{y0} = C_{L0}\cos(\phi_0) + C_{D0}\sin(\phi_0) \tag{7.28}$$

derivatives of the force coefficients over alpha denoted b $'$ are stated as

$$C'_{x0} = C'_{L0}\sin(\phi_0) - C'_{D0}\cos(\phi_0) \tag{7.29}$$

and

$$C'_{y0} = C'_{L0}\cos(\phi_0) + C'_{D0}\sin(\phi_0) \tag{7.30}$$

7.5 Author contributions

Gesine Wanke and Morten H. Hansen set up the 2DOF model and validated the model. Gesine Wanke and Torben J. Larsen have set up and validated the BEM-code to calculate equilibrium yaw angles. Gesine Wanke carried out the calculations. All authors have interpreted the obtained data. Gesine Wanke has prepared the manuscript with revisions of all co-authors.

Competing interests

This Project is an industrial PhD project funded by the Innovation Fund Denmark and Suzlons Blade Science Center. Gesine Wanke is employed at Suzlons Blade Science Center.

Chapter 8

Control modifications for extreme turbine loads driven by normal operation load cases

Control features are powerful and very cost-efficient methods to reduce wind turbine loads and therefore turbine costs. This chapter presents control changes made for the upwind and the downwind wind turbine configuration with the aim to reduce extreme loads as well as to eliminate fault cases from the spectrum of design driving load cases.

8.1 Introduction

Converting the existing Suzlon S111 2.1MW turbine from the original upwind configuration into the respective downwind configuration has been shown in chapter 4 to come with changes in the design driving loads. Other than the well known increase in fatigue loads for the downwind configurations (e.g. Glasgow et al. (1981)) the design driving extreme loads are also changed with the conversion from the upwind into the downwind configuration: While the rotor blades could benefit from an increased tower clearance and a reduced flapwise bending

moment, the tower bottom bending moment increases significantly. Further, a drop in annual energy production can be expected. Designing a cost competitive downwind turbine could, therefore, be achieved when the cost savings associated with the new rotor design compensate for the higher costs associated with the higher tower loads and the loss in energy production. The other option is to increase the rotor radius and therefore energy production to compensate for the increased tower costs.

Optimization frameworks such as WISDEM (Ning and Petch (2016)) or `Cp-Max` (Bortolotti et al. (2019)) have recently been used to design downwind turbines. As full load base calculations are computationally expensive within such optimization routines, only selected load cases are assessed. In that case, the optimized design might not be realizable as neglected fault cases might dominate the load spectrum.

To avoid such scenario high loads from design load cases (DLC) with fault conditions should be avoided. In case of the load base analysis from chapter 4 this regards the extreme flapwise blade root bending moment, the extreme tower longitudinal and lateral bending moments as well as the extreme main bearing tilt moment. If these loads were instead driven by loads in normal production (DLC 1.x) the loads could be directly associated with fluctuations on top of the mean loads presented in the previous chapter. In this case, a simpler optimization approach could be applied. This could be for example a scaling of the extreme loads with the ratio of mean loads between a baseline and a design iteration. Also, a transfer function could be used to generate extreme loads from linearized models and a wind field input.

To be able to realize such design approaches, the controller routines have to be adjusted to avoid high loads from DLC 2.2y (operation at extreme yaw errors), DLC 3.1 (Start-up), DLC 4.2 (shut down during extreme operational gust) and DLC 6.2 (idling at abnormal yaw errors). This chapter describes the changes made for the control routine and the resulting changes in tower clearance, loads and energy production. This will be seen to reduce the extreme tower bending moments by 12% in the upwind configuration and 19% in the downwind configuration. The flapwise blade root moment is observed to decrease by 4% in the upwind configuration and 11% in the downwind configuration. This comes however at the expense of higher blade torsion fatigue load associated with higher pitch activity of 2%. Further, a fatigue load increase for the downwind configuration is observed for the tower bottom bending moments of 6%. Also, a small reduction in annual energy production of 0.2% is observed for both turbine configurations.

8.2 Method

The Suzlon S111 2.1MW turbine is used in the upwind configuration and the downwind configuration as baselines as also described in chapter 4. The downwind configuration is a pure reassembly of the conventional upwind configuration: Cone and tilt angle increase the distance between the blade tip and the tower, while the blades are prebend towards the blade pressure side. The controller of the baselines is the DTU-controller (Hansen and Henriksen (2013)). The controller is for pitch-regulated variable speed turbines. It switches between a partial load region with optimal C_p-tracking and a full load region with constant torque control. Different events such as start-up or stopping routines or failure situations are initiated via the controller. Three main control features are implemented additionally to the DTU-controller. The implemented features involve a thrust-control for the tower loads, an advanced breaking program for the blade moment related loads and a free-yawing option for parked turbines during grid loss.
With the control modifications a new full design load base (DLB) comparison is conducted in the same manner as for the baselines (see sect. 4.2): The DLB is calculated with HAWC2 Madsen et al. (2019) according to the ICE standard 61400-1 edition3 (IEC (2014)). The results for the upwind configuration and the downwind configuration are presented as a direct comparison to the version with the advanced control denoted as "adv. Ctrl". The results are normalized with the extremes of the upwind configuration, as described in the methods of chapter 4.

8.2.1 Thrust-control

The first implemented control modification is a thrust-control. In this project, the feature is tuned to reduce tower base extreme loads due to DLC 4.2, the shut-down at extreme operational gusts. The routine reduces load fluctuations by keeping the thrust as constant as possible, avoiding high loads associated with the gust rather than the shut-down procedure. Figure 8.1 shows the control diagram of the thrust-control. The sum of the blade root moments is used to calculate an estimation of the thrust T. The signal is on the one hand low pass filtered and on the other hand, a moving average is calculated as a reference thrust T_{ref}. A PD-controller is used on the difference between the reference thrust and the filtered thrust, to create a pitch signal under limit range. The lower limit avoids high loads from turbulence the higher limit avoids high power losses. The low pass filtered nacelle wind speed is used for a wind speed dependent gain scheduling. This guarantees a smooth transition between active and non active thrust control. The transition between nonactive and active thrust control is

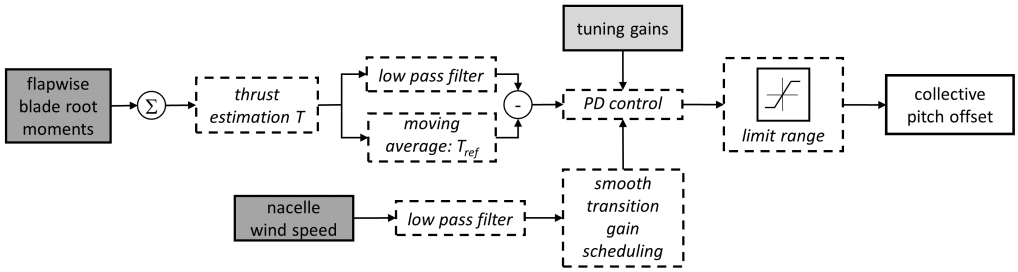

Figure 8.1: Flow chart of the thrust control controller addition.

from rated wind speed to 1ms^{-1} above rated wind speed.

8.2.2 Breaking program to avoid operation at high yaw errors

Turbine controllers can have different breaking routines for different fault signals. It has been observed from the timeseries, that the loads would be significantly lower if the turbine was idling instead of operating at these extreme yaw errors. In order to apply a wind direction-dependent stopping routine, at least two redundant measurements need to supervise the wind direction. This could be done by using two independent wind vanes or by supervising the wind vane signal by the yaw related flapwise blade root moment signal. For simplicity, the approach with two wind vanes is assumed to be suitable.
The implemented addition is a conditional stopping routine that avoids the operation at high yaw errors: If the filtered nacelle wind speed and the filtered nacelle wind direction are above a certain threshold a stop signal is triggered.

8.2.3 Free yaw at grid loss during idling

If the shut-down situation during extreme coherent gust is no longer design driving for the longitudinal tower bottom bending moment, the longitudinal tower bottom bending moment signal can get into a load range that is lower than the range of the lateral tower bottom bending moment. The reason is that the tower can suffer from low damped lateral motion if the turbine is parked at extreme

winds while the gird is lost and the yaw direction can not be adjusted. As the high loads occur only in case of high yaw error, a solution inspired by Hitachi is implemented. Hitatchi (2019) has successfully changed the yaw system to be free yawing in any idling situation as the tower loads were seen to be reduced.
The free yaw at DLC 6.2 the parked situation with grid loss is realized in HAWC2 with the stick-slip bearing from the implemented ESYSTools. It is estimated that reducing the bearing friction by 50% would be possible for 50% higher cost of the yaw system for this turbine.

8.2.4 Start-up and shut-down routines for the downwind configuration

The start-up and shut-down routines need to be adjusted for the downwind configurations. Inherent to the downwind configuration the tower bottom moment consists of a contribution due to the gravity force on the rotor-nacelle assembly that acts in the same direction as the moment due to the thrust force. As a consequence, the start-up and shut-down routines need to be changed to avoid extreme tower bottom-bending moments. For the start-up routine, the pitch speed has to be reduced to avoid thrust overshoots increasing the tower bottom moment. The normal shut-down routine incorporates a two-phase shut down with an initial low pitch speed phase and a second phase with higher pitch speed. In the shut-down routine for the downwind configuration, especially during the occurrence of gusts, the initial pitch speed has to be increased to avoid high loading due to the gust which would again lead to a thrust overshoot and therefore high tower loads. Compared to an emergency stop routine it remains a two-phase shut-down routine and the increased pitch speed of the first phase is 75% of the second phase.

8.3 Results

The following section shows the influence of the control updates on the tower clearance, the extreme loads, the fatigue loads and the annual energy production (AEP) for the upwind configuration and the downwind configuration. All results are normalized with the extreme of the upwind configuration.

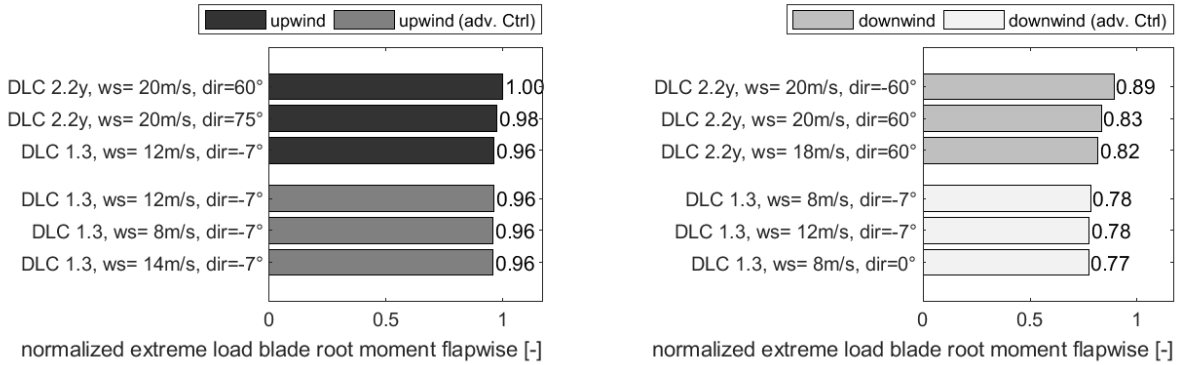

Figure 8.2: Comparison of flapwise blade root bending moments between the upwind and the downwind configuration, without and with advanced control (adv. Ctrl), for the highest three bending moments, normalized with the extreme of the upwind configuration. Design load cases are: DLC 2.2y power production with abnormal yaw error and DLC 1.3 power production in extreme turbulence.

8.3.1 Tower clearance

The advanced control has hardly any influence on the tower clearance on neither turbine configuration. The difference in minimum tower clearance is less than 1%. DLC 1.3 remains the design driving load case with the control update. The controller is not tuned to handle rapid fluctuations in the thrust due to extreme turbulence as the time for slope estimation is relatively long, compared to the time constant for the forecast.

8.3.2 Extreme loads

The following section shows the difference in the normalized extreme loads of the upwind configuration and the downwind configuration with the respective version with advanced control. For normalization, the highest extreme of the upwind configuration is used.
Figure 8.2 shows the extreme load comparison for the flapwise blade root bending moment normalized with the extreme of the upwind configuration. The advanced control has eliminated the design load case of operation at high yaw errors

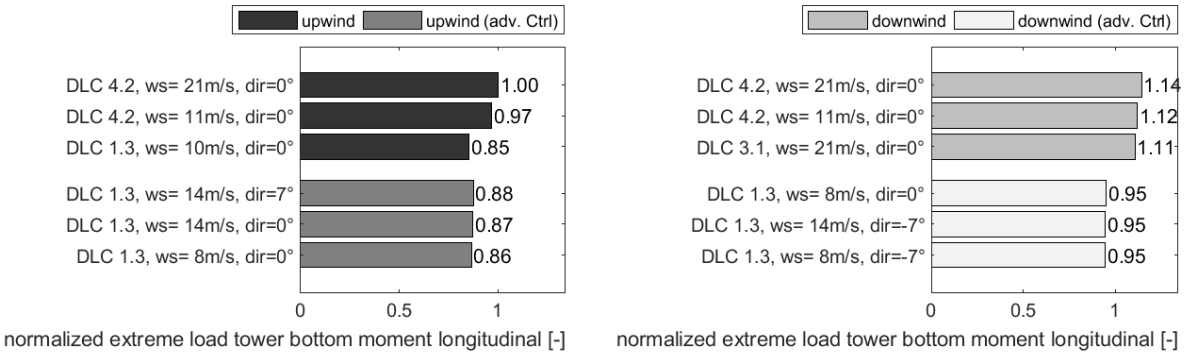

Figure 8.3: Comparison of tower bottom longitudinal bending moments between the upwind and the downwind configuration, without and with advanced control (adv. Ctrl), for the highest three bending moments, normalized with the extreme of the upwind configuration. Design load cases are: DLC 4.2 shut down during extreme operational gust, DLC 3.1 start-up and DLC 1.3 power production in extreme turbulence.

(DLC2.2y) from the design driving load cases for the flapwise blade root moment. While this means a load reduction of 4% in the upwind configuration the downwind configuration shows a load reduction of 11%. This reduces the load of the downwind configuration with advanced control 18% below the load level of the comparable upwind configuration.
The advanced control emphasizes the advantage of the downwind configuration as the blades are unloaded due to the downwind coning direction. As an emergency stop is initiated from the high wind speeds at high yaw errors the loads are significantly reduced in DLC2.2y, resulting in the operation at extreme turbulence being the design driving situation for the flapwise blade root moment.
Figure 8.3 shows the normalized extreme load comparison for the longitudinal tower bottom bending moment for the upwind configuration and the downwind configuration with the respective versions with advanced control. The figure shows that the design driving load case in the upwind and the downwind configuration has been changed from the shut-down during the extreme operational gust to the operation at extreme turbulence. With the implementation of the advanced control, the extreme load is reduced by 12% in the upwind configuration. In the case of the downwind configuration, the load is reduced by 19% with the implementation of the advanced control.

The figure shows that the thrust control is able to significantly reduce the longitudinal tower bottom bending moment which is related to this extreme operational gust. The thrust control can successfully predict the load peaks from the extreme operational gust due to the forecast feature (linear extrapolation).
Also, the tower bottom loads associated with the start-up situation have been successfully reduced with the updated pitch table. The downwind configuration suffers from the alignment of the thrust force and the gravity moment of the rotor-nacelle assembly in the tower bottom bending moment compared to the respective upwind configuration. This is inherent to the configuration.
Table 8.1 shows a summary of the normalized extreme loads and the according design driving load cases for the upwind configuration and the downwind configuration and the respective configurations with the advanced control.

The table shows that the implementation of the advanced control for extreme load alleviation has been successful. The tower bottom bending and main bearing tilt loads reduce more than 10% in the upwind configuration and slight load reductions are observed for the blades root loads. In the case of the downwind configuration, significant tower bottom and blade root load reduction have been achieved, with exception of the edgewise blade root moment which is dominated by reduced edgewise damping (see also chapter 5). Parked conditions (DLC 6.1 and DLC 6.2) remain design driving for the tower bottom lateral bending moment but the total tower load is driven by the longitudinal tower bottom bending moment. The dominant design driving situation for the configurations with advanced control is the operation at extreme turbulence. Further direction changes during the normal operation lead to high loads.

8.3.3 Fatigue loads

Table 8.2 shows the fatigue load difference compared to the upwind configuration for the upwind configuration with the advanced control and the downwind configuration without and with advanced control.

The table shows that in the upwind configuration only the fatigue load for the blade root torsion increases 2% with the implementation of the control update.

Table 8.1: Design driving load cases for the upwind configuration, the upwind configuration with advanced control, the downwind configuration and the downwind configuration with advanced control.In bolt are design driving load cases that changed due to the advanced control. Design driving load cases are: DLC 4.2 shut down during extreme operational gust, DLC 6.2 idling at abnormal yaw error, DLC 6.1 parked at extreme wind, DLC 1.3 power production in extreme turbulence, DLC 2.2y operation at extreme yaw errors.

load sensor	**DLC**			
	upwind	upwind (adv. Ctrl)	downwind	downwind (adv. Ctrl)
tower bottom flange longitudinal	DLC 4.2	**DLC 1.3**	DLC 4.2	**DLC 1.3**
tower bottom flange lateral	DLC 6.2	**DLC 6.1**	DLC 6.2	**DLC 6.1**
tower bottom flange torsional	DLC 1.3	DLC 1.3	DLC 1.3	DLC 1.3
blade root flange flapwise	DLC 2.2y	**DLC 1.3**	DLC 2.2y	**DLC 1.3**
blade root flange edgewise	DLC 1.3	DLC 1.3	DLC 1.3	DLC 1.3
blade root flange torsional	DLC 6.2	**DLC 1.4**	DLC 6.2	**DLC 1.4**
main bearing tilt	DLC 2.2y	**DLC 1.3**	DLC 1.3	DLC 1.3
main bearing yaw	DLC 1.3	DLC 1.3	DLC 1.3	DLC 1.3

load sensor	**Δ normalized extreme load [-]**		
	upwind (adv. Ctrl)	downwind (no prebend)	downwind (no prebend) (adv. Ctrl)
tower bottom flange longitudinal	-0.12	+0.14	-0.05
tower bottom flange lateral	-0.27	+0.10	-0.23
tower bottom flange torsional	+0.00	-0.06	-0.07
blade root flange flapwise	-0.04	-0.11	-0.22
blade root flange edgewise	-0.03	+0.05	+0.06
blade root flange torsional	-0.04	+0.04	-0.10
main bearing tilt	-0.21	+0.05	+0.03
main bearing yaw	+0.01	-0.07	-0.07

Table 8.2: Difference in the normalized lifetime equivalent load between the upwind configuration, the upwind configuration with advanced control, the downwind configuration without prebend and the downwind configuration without prebend with advanced control for DLC 1.2 (normal operation).

load sensor	Δ normalized life time equivalent load [-]		
	upwind vs. upwind (adv. Ctrl)	upwind vs. downwind	upwind vs. downwind (adv. Ctrl)
tower bottom flange longitudinal	-0.00	-0.02	+0.04
tower bottom flange lateral	+0.00	+0.03	+0.09
tower bottom flange torsion	+0.00	-0.00	-0.00
blade root flange flapwise	-0.00	+0.06	+0.07
blade root flange edgewise	-0.00	+0.07	+0.07
blade root flange torsion	+0.02	+0.08	+0.10
main bearing tilt	-0.00	+0.06	+0.06
main bearing yaw	+0.00	-0.02	-0.02

Also for the downwind configuration, this increase is 2%. The fatigue load for the blade root torsion was expected to increase as the pitch system is more active. In the downwind configuration also an increase in the tower bending fatigue loads of 6% is observed with the implementation of the advanced control.

8.3.4 Annual energy production

With the implementation of the advanced control, the annual energy production (AEP) is slightly reduced. The change in AEP is the same for both, the upwind and the downwind configuration. The AEP of the configurations with advanced control is 0.2% lower than the AEP of the configurations without advanced control.

8.4 Conclusion

This chapter showed that significant extreme load reductions could be achieved with control updates. Applying a thrust-control that aims for keeping the thrust level constant can reduce tower bottom longitudinal tower bending moments significantly. This comes at the expense of an AEP loss of 0.2% and higher blade torsion fatigue load due to higher pitch activity. In the cases for the downwind configuration, also higher tower fatigue loads are observed. In the case of the downwind configuration, a better trade-off between extreme and fatigue load could possibly be found by tuning the control parameter differently. This depends however if the tower design is driven by extreme or fatigue loads.
Releasing the yaw for the parked situation with grid loss reduces the tower lateral loads. This assures that the longitudinal tower bottom bending moment still dominates the total tower bottom bending moment.
Finally, the advanced breaking routine that initializes an emergency stop at high wind speeds and high yaw errors reduces the extreme flapwise blade root moment. The standstill load and the emergency stop routine are associated with lower extreme loads than the operation at extreme yaw errors.

Bibliography

Bortolotti, P., Kapila, A., and Bottasso, C. L. (2019). Comparison between upwind and downwind designs of a 10 mw wind turbine rotor. *Wind Energy Science*, 4(1):115–125. https://doi.org/10.5194/wes-4-115-2019.

Glasgow, J., Miller, D., and Corrigan, R. (1981). Comparison of upwind and downwind rotor operations of the doe/nasa l00-kw mod-0 wind turbine. *NASA Report*, TM-8744:225–234.

Hansen, M. and Henriksen, L. (2013). Basic dtu wind energy controller. *DTU-Wind-Energy-Report*, E-0028.

Hitatchi (2019). Hitatchi 5200kw wind turbine, htw5.2-127, htw5.2-136. *Product catalogue*. url: http: //www.hitachi.com /products /energy /wind /Catalog / _ _icsFiles /afieldfile /2018 /01 /31 /HTW5.2 _EG-E109.pdf; Date of Access: 2019-09-30.

IEC (2014). Iec 61400-1 ed.3 wind turbines- part1: Design requirements. Technical report, International Electronical Commission.

Madsen, H. A., Larsen, T. J., Pirrung, G. R., and Zahle, F. (2019). Implementation of the blade element momentum model on a polar grid and its aeroelastic load impact. *Wind Energy Science Discussion*. https://doi.org/10.5194/wes-2019-53, in review.

Ning, A. and Petch, D. (2016). Integrated design of downwind land-based wind turbines using analytic gradients. *Wind Energy*, 19:2137–2152. https://doi.org/10.1002/we.1972.

Chapter 9

Re-design of an upwind rotor for a downwind configuration: design changes and cost evaluation

---

The following will present the manuscript submitted to "Wind Energy Science" for the rotor redesign and the cost evaluation, formatted for the thesis format.
Wanke, G., Bergami, L., Zahle, F. and Verelst, D. R.: **Re-design of an upwind rotor for a downwind configuration: design changes and cost evaluation**

Manuscript submitted: 12 Dec 2019

Re-design of an upwind rotor for a downwind configuration: design changes and cost evaluation

Gesine Wanke[1], L. Bergami[1], F. Zahle[2], D. R. Verelst[2]

[1] Blade Science Center Suzlon, Vejle Denmark
[2] DTU Wind Energy, Technical University of Denmark, Roskilde, Denmark

Correspondence: Gesine Wanke, Suzlon Blade Science Center, Havneparken 1, 7100 Vejle, Denmark. E-mail: gesine.wanke@suzlon.com

Abstract

Within this work, an existing model of a Suzlon S111 2.1MW turbine is used to estimate potential cost savings when the conventional upwind rotor concept is changed into a downwind rotor concept. A design framework is used to get realistic design updates for the upwind configuration as well as two design updates for the downwind configuration, including a pure material cost-out on the rotor blades and a new planform design. A full design load basis according to the standard has been used to evaluate the impact of the redesigns on the loads. A detailed cost model with load scaling is used to estimate the impact of the design changes on the turbine costs and the cost of energy. It is shown that generally lower blade mass can be achieved with the downwind configurations of up to 5% less than the upwind redesign. Compared to an upwind baseline, the upwind redesign shows an estimated cost of energy reduction of 2.3% where the downwind designs achieve a maximum reduction of 1.3%.

9.1 Introduction

Historically the first wind turbines were dominantly downwind turbines, where the rotor was placed behind the tower, seen from the incoming wind. This turbine configuration was considered safer than the alternative upwind configuration with the rotor in front of the tower since the rotor blades would bend away from the tower under turbine operation. Early research, mainly by NASA and as-

sociated partners compared the downwind rotor configuration with the upwind configuration. Glasgow et al. (1981) showed that the wake behind the tower caused significantly higher cyclic flapwise blade root loads in the downwind configuration compared to the loads of the upwind rotor configuration. However, neither for the flapwise mean blade root loads nor for the edgewise blade root loads differences between the two configurations could be shown.
Many residents living near early downwind wind turbines reported high noise levels and especially the high unsteadiness, a "thumping" sound was reported as a nuisance (Metzger and Klatte (1981)). The rotor blades passing through the tower wake caused high low-frequency noise and amplitude modulation. Measurements in an anechoic wind tunnel by Greene (1981) demonstrated that downwind rotors on a lattice tower radiated more noise than downwind rotors on a tubular tower due to the narrower and deeper tower wake. Upwind rotor configurations, on the other hand, were found to be significantly less noisy. Upwind rotor configurations therefore dominated industrial applications as well as the focus in research efforts during the 1990s and 2000s.
Cost driven industrial designs prefer larger rotor areas to capture more energy. The rotor blades for modern sized upwind wind turbines are designed under a constraint of maximum blade tip deflection to avoid a collision of the blades with the tower. Since the blade tip deflection constraint could be eliminated in modern sized wind turbines, the downwind configuration is currently coming into research focus again, especially for future even larger rotors.
Advances in wind turbine noise mitigation techniques since the 1980s as well as airfoil design could overcome the previously reported noise issues, to an acceptable level. Reiso and Muskulus (2013) successfully eliminated the tower shadow effect on the fatigue loads by using a fairing. While the fairing is a rather costly device to implement the study further showed the potential that fatigue loads can be significantly reduced by a reduced flapwise stiffness, alleviating loads by blade deformation.
Ning and Petch (2016) used an optimization framework to compare the levelized cost of energy of land-based upwind and downwind turbines. The study included turbines of different wind classes, rated power and rotor diameter. Modest cost savings could be achieved for the downwind configuration compared to the upwind configuration for wind turbines of wind class III. Blade mass savings had to offset the higher tower cost originating from the increased tower bottom bending moment as the gravity overhanging moment of the rotor-nacelle assembly coincides with the moment from the thrust force.
In a system-level design study for large rotors Zalkind et al. (2019) showed that coned downwind rotors significantly reduce peak blade loads during operation but have a lower annual energy production compared to a coned upwind configuration of the same size. While the group predicts larger main bearing peak loads

for the downwind configuration related to blade length, mass, and cone angle they suggest that the increased tower loads observed by other groups could be overcome by properly balancing the nacelle on the tower.
A reduced edgewise damping for a downwind configuration compared to an upwind configuration was identified by Wanke et al. (2019a), leading to significantly higher edgewise loads in the downwind configuration than in the upwind configuration. In a following study on a 2.1MW turbine Wanke et al. (2019b) showed that large downwind cone angles could reduce the edgewise damping further, as the out-of-plane contribution of the edgewise mode shapes is decreased. A significantly reduced tower torsional stiffness, on the other hand, e.g. a lattice tower configuration would benefit the downwind configuration.
Aligning the blades with the loading direction of aerodynamic forces, gravity, and centrifugal force is an opportunity of the downwind configuration to significantly reduce flapwise bending loads, loading the blade in axial tension instead. Such a load distribution is achieved by adjusting the cone angle and blade prebend. These downwind rotors with so-called "load alignment" have been suggested as an option to reduce blade mass significantly, utilizing large cone angles and downwind prebend by Loth et al. (2017) for a 13.2MW wind turbine. The study also indicated mass savings compared to the conventional upwind rotor when the blade length is increased to compensate for energy production losses.
Bortolotti et al. (2019) used an optimization framework to compare the cost efficiency of an upwind configuration with a downwind configuration and a downwind configuration with "load alignment". The analysis for a 10MW turbine showed difficulties to reach a more cost-efficient design for the downwind configurations than the conventional upwind configuration, due to other component costs.
Often proposed are downwind configurations with a passive wind direction alignment. Such yaw systems could be cost-efficient as they simplify the turbine control, and reduce operation and maintenance costs, as they could purely be used for cable unwinding. However, Wanke et al. (2019c) showed on an example of a 2.1MW turbine with a tilted rotor that such systems align passively at high yaw angles for high wind speeds resulting into significant power loss. The study concluded that tilt angle, cone angle and blade stiffness would need to be specifically designed for a free yawing downwind configuration. This would expose additional constraints on a downwind turbine design, while the benefit in terms of a cost-efficient turbine is questioned.
The cost-efficient design of wind turbines has been approached to a growing extent by the use of optimization frameworks. Over the years it has been questioned that rotors designed for the maximum efficiency result in the most cost-efficient turbine designs. Optimizing a conventional 10MW upwind turbines for the lowest cost of energy (COE) Bottasso et al. (2016) showed, that designing the rotor for minimum cost instead of maximum annual energy production (AEP) results

into rotors with larger chord, higher thickness and lower AEP. Higher absolute thickness could utilize higher stiffness with less material resulting in the lower cost compensating the AEP -loss from the less efficient, thicker airfoils.
Lower rotor loads could potentially result in the possibility to increase the rotor length and therefore increase the overall power capture. This could be a more cost-efficient rotor than a traditional design approach, also for upwind turbines. Bottasso et al. (2015) tried therefore to design a low induction rotor for a 10MW wind turbine with an optimization framework where the blade shape was designed with the common aerodynamic parameters, such as chord, twist and airfoil thickness. Their work showed that maximum AEP solutions might be achievable with low induction rotors, but the minimum cost solutions might be different from the maximum AEP solutions. It was seen to be very dependent on the cost model if the higher AEP could pay for the increased rotor diameter.
Loenbaek et al. (2019) investigated design trends by an optimization of power capture based on 1D momentum theory. Their work indicated that the maximum power capture is achievable by a larger rotor diameter and operation at lower cp than maximum. For a conventional upwind turbine, this is achieved by so-called thrust clipping or peak-shaving. The peak-shaving is a control feature that reduces extreme flapwise loads as well as it increases the minimum blade tip to tower clearance in the upwind configuration while sacrificing AEP.
This paper evaluates the specific example of the Suzlon S111 2.1MW turbine the potential of a downwind turbine configuration compared to the original upwind turbine configuration regarding mass and cost reduction. It is shown that a 5% lower rotor mass can be achieved in the downwind configuration than in the upwind configuration. Despite higher tower and foundation costs the turbine specific cost model indicates lower capital expenditures (CAPEX) for the downwind configuration than the upwind configuration. Due to the difference in AEP, the upwind configuration is the most cost efficient configuration with a 1.0% lower COE.

9.2 Methods

This work aims to compare an upwind configuration of an existing turbine with a downwind configuration, from a cost and mass perspective. The chosen example turbine is the Suzlon S111 2.1MW turbine, a commercial upwind turbine. The turbine is designed for wind class IIIA, with glass fiber blades, a rotor diameter of 112m on a 90m tubular tower. The turbine is pitch regulated with a variable speed generator. The shaft is tilted, the rotor is coned and the blades are prebend. All three geometrical parameters increase the blade-tip to tower clear-

Table 9.1: Turbine configurations regarded in design and cost estimation

Name	configuration	aerodynamic planform	structure
S111uw	upwind	baseline	baseline
S111uw PF	upwind	optimized	optimized
S111dw	downwind	baseline	baseline
S111dw STR	downwind	baseline	optimized
S111dw PF	downwind	optimized	optimized

ance in the upwind configuration.
For this turbine, a new baseline rotor blade is defined, inspired by the commercial blade, which is adapted to the framework. For the baseline rotor, an upwind turbine configuration is generated, called S111uw. Additionally, a downwind baseline turbine configuration is defined with the baseline rotor called S111dw. The downwind configuration utilizes the same cone and tilt angle, both increasing blade tip to tower distance. Since the blade prebend of the rotor is towards the blade pressure side the prebend decreases the blade tip to tower distance in the downwind configuration. Three rotor redesigns are made. For the upwind configuration, a blade planform and internal structural redesign is made. The design is called S111uw PF. For the downwind configuration, two scenarios are regarded. Firstly, a pure blade material reduction is performed, called S111dw STR. This corresponds to a configuration change of an existing upwind configuration into a downwind configuration while keeping the blade molds but saving blade material. Secondly, a blade planform and structure redesign in the same manner as for the upwind redesign called S111dw PF. Table 9.1 shows a summary of the design configurations regarded as well as a name indicator used throughout the study.

The rotor design procedure uses a low fidelity optimization tool to create a blade planform and stiffness distribution. The planform and stiffness distribution are afterwards matched within the HAWTOpt2 framework Zahle et al. (2015, 2016) to create a full HAWC2 (Madsen et al. (2019)) set-up for aeroelastic load calculations. For all designs, a full design load basis (DLB) is calculated. The loads are used to calculate a failure index of the blades, to evaluate if the redesigns are acceptable. From the tower loads, the required tower material is calculated. Finally, the costs of all five designs are calculated with a load and mass scaling cost model. This design procedure is conceptually outlined in Figure 9.1.

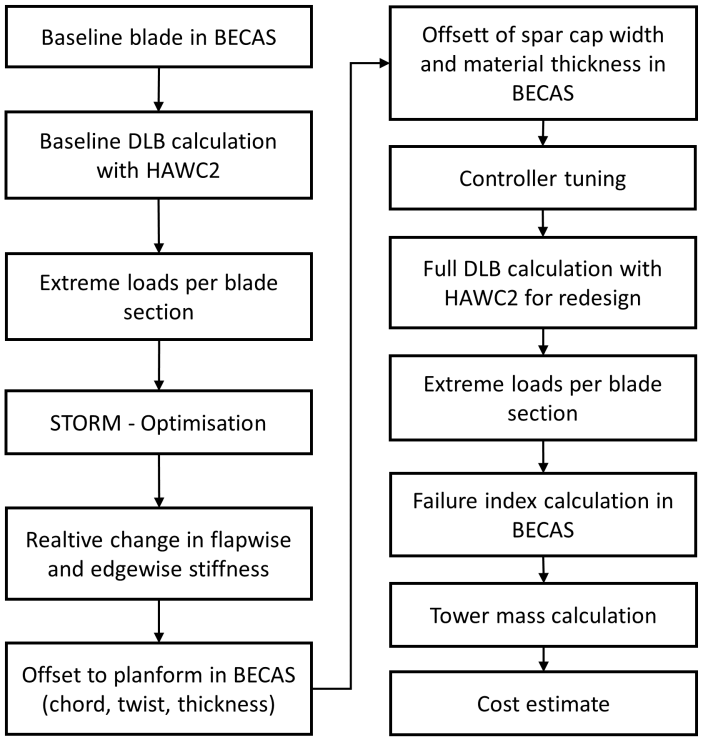

Figure 9.1: Flow chart of the work flow for design and cost estimation.

9.2.1 Baseline blade in BECAS

The baseline blade is set-up in BECAS (a 2D cross-sectional analysis tool, Blasques (2011)), as it is implemented in the HAWTOpt2 framework. This approach has several advantages. Firstly, through BECAS it allows having reasonable structural blade properties, which can be directly exported as inputs for load simulations with HAWC2. Secondly, even though the HAWTOpt2 framework is not utilized for optimization, it allows to parametrically modify the planform and structural dimensions of the baseline blade. Within the workflow of the framework the structural properties are recalculated within BECAS and can be exported for load calculations.
The baseline blade is described according to the parameterization adopted in

HAWTOpt2 Zahle et al. (2016). To set-up the baseline blade in BECAS, the planform geometry is directly loaded into the framework. From blade length, relative thickness, chord, twist and the airfoil geometry the blade surface created as a 3D lofted surface. The chordwise position of the main structural regions, namely trailing edge caps, spar caps, shell panels, trailing edge and leading edge are defined in 19 cross-sections relative to the chord length. For each region, the positioning and material stacking is applied from blade lay-up plans.
For the baseline blade structural properties, total mass, static mass moment and blade eigenfrequencies are compared to the commercial blade to assure the baseline is reasonable and fairly close to the commercial blade. The same has been done with turbine eigenfrequencies and damping, as well as the design driving loads for blades, main bearing, and tower.

9.2.2 Design load basis and controller definition.

Full design load bases are simulated with HAWC2 (version 12.7) according to the IEC-standard 61400-1 Edition 3 (IEC (2014)). The interpretation of the design load basis by the Technical University of Denmark (DTU), described by Hansen et al. (2015), is used. For the downwind configuration the load simulations are conducted with an inflow inclination angle of 0°. The combination of positive flow inclination angle and turbine tilt was seen to be beneficial in downwind configurations by Wanke et al. (2019a). It is therefore assumed to be a more realistic scenario to simulate wind fields without inclination angle for downwind configurations.
The annual energy production (AEP) is calculated for all designs. It is calculated from the normal operation load case with six turbulence seeds, for all configurations without inclination or yaw angle. The turbulence intensity is according to the IEC-standard class A.
For all load calculations, the controller set-up from DTU (Hansen and Henriksen (2013)) is used in this study with two additional features. The controller is for pitch regulated variable speed turbines with partial and full load regions. Optimal C_p-tracking is used in the partial load region and a constant torque strategy in the full load region. The detailed description of the controller can be found in Hansen and Henriksen (2013) and the source code is freely available online (https://github.com/DTUWindEnergy/BasicDTUController). The controller has been automatically tuned using a pole placement routine implemented in HAWCStab2 (Hansen (2004)), and which is described in more detail by Tibalidi et al. (2014). Different events can be initiated from the main controller, such as start-up and shut-down or failure situations.

Start-up and shut-down pitch speed in the implemented routines of the DTU-controller need different values for downwind configurations than comparable upwind configurations. The moment due to thrust force and the gravity overhanging moment of the rotor nacelle assembly both increase the tower bottom bending moment. Start-up routines, especially at high wind speeds, need to have a lower pitch speed in downwind configurations than the comparable upwind configurations. Shut-down routines, especially during gusts, have to be of faster pitch speed in the downwind configuration. Both adjustments have to be made to unload the tower bottom.
For a control routine that reflects an industrial controller, three failure scenarios are adapted. Firstly, the failure scenario of one blade getting stuck at a current pitch angle, the pitch angle of one blade is kept constant at the current pitch angle at the time of failure. The deviation of the pitch angle from the setpoint initiates a stop routine of the turbine. Secondly, the pitch run away (DLC 2.2p) is not included, since the failure mode is prevented by the type of pitch actuators used. Thirdly, for the scenario of a parked turbine with high yaw errors the wind field is interpreted as a wind direction change of 360° over 570 seconds.
To eliminate fault cases from the design driving loads, and to stay similar to an industrial controller, two additional control features are implemented as separate dlls manipulating the output or input from the controller to HAWC2, for practical reasons. The first addition is a thrust control aiming to reduce fluctuations of the thrust. The second addition is a conditional stop routine avoiding operation at high yaw errors and high wind speeds. The following explains the two additions in more detail.
Figure 9.2 shows the thrust control feature. The thrust control uses the sum of

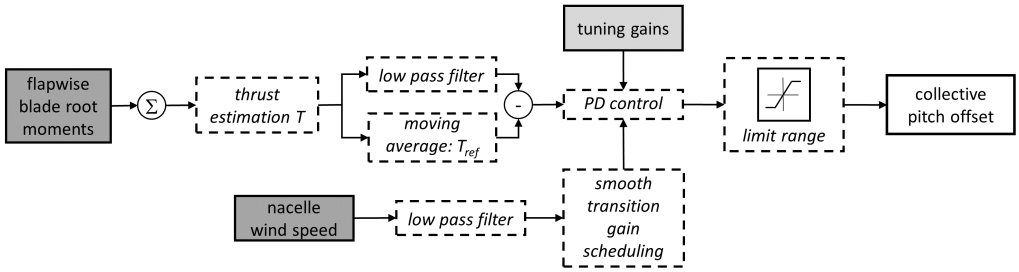

Figure 9.2: Flow chart of the thrust control controller addition.

the flapwise blade root moments to estimate the thrust T. The thrust signal is on one hand low pass filtered and on the other hand, a reference thrust T_{ref} is calculated as a moving average. A PD-controller is used to generate a collective

pitch offset under range limitation. The pitch range is limited to avoid high loads from turbulence (lower limit) and high power losses (upper limit). The filtered wind speed of the nacelle anemometer is used for wind speed dependent gain scheduling to guarantee a smooth transition between active and not active thrust control.
The conditional stopping routine triggers the turbine stop, as soon as the filtered wind speed and the filtered wind direction are above a certain threshold. For practical reasons of implementation, the emergency stop is triggered.

9.2.3 STORM - Optimization

The re-design of the rotor blades is performed using the in-house code STORM (Suzlon Turbine Optimization fRaMework). The code is aimed at fast conceptual rotor design optimization studies, and couples steady aerodynamic AEP considerations, with a simplified blade structural estimation. The code, written in Matlab, is organized as a nested optimization problem. The outer optimization loop controls the blade geometrical planform, and minimizes the blade mass subject to: linear constraints on the geometrical design variables, non-linear constraints on minimum AEP, and feasibility of all the inner optimization problems (Eq. 9.1).
In this study, the blade geometry design variables are limited to four spline control points that set the thickness-over-chord (TOC) ratios in fixed points along the blade span. The geometry at the blade root is fixed up to the point of maximum chord for all configurations. For each iteration of the outer optimization loop, six steps are taken; they are described in the following sections, and briefly consists of:

1. The blade TOC spline is defined from the control points (the four design variables).
2. The blade geometrical planform is outlined in terms of chord, twist and thickness distribution. An inner optimization returns the chord distribution that minimizes the squared difference from a target axial induction distribution.
3. Steady operational loads and the power curve are retrieved from a standard steady BEM formulation. An inner optimization sets the pitch angle to maximize aerodynamic power, subject to limitation on maximum: power, thrust, aerodynamic flapwise bending moment, and angle of attack (for stall considerations).

4. The steady BEM loads are scaled to extreme loads to be used in the structural optimization.

5. The blade structural properties are determined solving a fast low-fidelity structural optimization problem. The blade structure is simplified to two symmetric glass fiber spar-caps joined by an ellipse, Fig. 9.3. The inner optimization sets the thickness and width of the spar cap, and the ellipse thicknesses to minimize the blade static mass moment, subject to constraints on: maximum strain, maximum deflection, maximum linear buckling index, and design variables range.

6. Finally, the outer loop optimization objective function is evaluated. The estimated blade mass is here taken as objective function, and minimum AEP output is enforced as a non-linear constraint.

9.2.3.1 Outer optimization loop

The outer optimization problem (Eq. 9.1) is solved using the Matlab Pattern Search method (G. Kolda (2014)). The algorithm is set up to perform a complete search and pooling around the current point.

$$\begin{aligned} \underset{\vec{a},\vec{t},\vec{e},\vec{h}\in\mathbb{R}^N}{\text{minimize}} \quad & m\left(\vec{a},\vec{t},\vec{e},\vec{h}\right) \\ \text{subject to} \quad & AEP\left(\vec{h}\right) \geq AEP^{min}, \\ & \delta\left(\vec{a},\vec{t},\vec{e},\vec{h}\right) \leq \delta^{max}, \\ & \varepsilon_i\left(a_i,t_i,e_i,h_i\right) \leq \varepsilon^{max}, \quad i=1,\ldots,N, \\ & \eta_i\left(a_i,t_i,h_i\right) \leq \eta^{max}, \quad i=1,\ldots,N \end{aligned} \tag{9.1}$$

where m is the mass of the blade, depending on the variables of spar cap width $\vec{a} = [a_1,\ldots,a_N]$, spar cap height $\vec{t} = [t_1,\ldots,t_N]$, the shell thickness $\vec{e} = [e_1,\ldots,e_N]$ and the section height $\vec{h} = [h_1,\ldots,h_N]$ at each of the N cross sections. The constraints are a minimum AEP, a maximum blade deflection δ, a maximum strain ε, and a maximum buckling coefficient η. A list of all formula symbols can also be found in Table 9.5 in the appendix.
The design variables are here the four thickness-over-chord (TOC) control points ratios. Linear constraints on the design variables are enforced to ensure they maintain within reasonable ranges, and that monotonically decreasing values are selected from root to tip. The objective function consists for this problem of

minimizing the estimated blade mass, subject to non-linear constraints to: reach a minimum AEP output (as derived from the BEM steady power curves) and ensure feasibility in all the inner optimization problems.

9.2.3.2 Blade geometrical planform

Once the iteration TOC control points are fixed, the TOC distribution along the blade span is outlined with a Piecewise Cubic Hermite Interpolating Polynomial. A wind speed in the below-rated variable speed range is chosen, and the target axial induction distribution for the blade at that wind speed is fixed as an input. Similarly, also the angles of attack at which the airfoils are expected to operate at that wind speed point are also fixed. Both the target induction and the target angles of attack of the airfoils could in principle also be driven by the outer optimization loop but are considered as fixed inputs in this study.
With the given input set (TOC, target induction, target AoAs) the blade geometry is then retrieved in terms of chord, twist angle, and thickness for each section along the blade span. The chord is retrieved by solving a set of independent minimization problems (Eq. 9.2), one for each section along the blade span. The optimization objective is to minimize the square error between the target axial induction for that section, and the current induction, function of chord, subject to a linear constraint on the minimum and maximum chord.

$$\begin{aligned} &\underset{c_i \in \mathbb{R}^N}{\text{minimize}} && \left(ind_{target\ i} - ind_i\right)^2 \\ &\text{subject to} && c^{min} < c_i < c^{max} \end{aligned} \tag{9.2}$$

In the current iteration the axial induction is retrieved from a steady BEM formulation, following Ning's implementation (Ning (2014)), where the BEM convergence is solved by minimizing a residual function of the flow angle. Once the chord is fixed, the twist angle is simply set as the difference between the converged flow angle returned by the BEM, and the input angle of attack for that section (minus eventually a chosen constant reference pitch angle).

9.2.3.3 Steady loads and power curves

Given the blade geometrical definition as from the step above, the steady power and loads curves are then determined running a standard steady BEM formulation, Hansen (2008), sweeping wind speeds between cut-in and cut-out. From the

steady power curve, the Annual Energy Production (AEP) is retrieved accounting for the chosen wind speed distribution.
The operational pitch angle at each wind speed is retrieved from a simple optimization loop, where the objective is to maximize the aerodynamic power output, subject to constraints on: maximum power (the aerodynamic rated power), maximum thrust force, maximum aerodynamic blade flapwise bending moment, and minimum "stall distance" (Eq. 9.3). The latter is defined as a minimum margin in degrees between the steady BEM angle of attack and the point of maximum lift for the corresponding airfoil; the stall constrained is only enforced for the outer 40 % of the blade span.

$$\begin{aligned} \underset{\beta \in \mathbb{R}}{\text{maximize}} \quad & P(\beta) \\ \text{subject to} \quad & P < P^{max}, \\ & T < T^{max}, \\ & M_{flap} < M_{flap}^{max}, \\ & \alpha < (\alpha^{max} - \alpha_{stall\ distance}) \end{aligned} \tag{9.3}$$

where β is the pitch angle, P is the aerodynamic power, T is the thrust force, M_{flap} is the flapwise bending moment. The angle of attack is α and $\alpha_{stall\ distance}$ is the "stall distance". In the case of this study, the constraint of maximum thrust and maximum aerodynamic flapwise bending moment are not active.

9.2.3.4 Loads scaling

The maximum aerodynamic steady flapwise bending moment is retrieved from the step above, and is scaled up to an extreme load using a ratio retrieved from full DLB HAWC2 simulations of the baseline blade:

$$M_{extreme} = M_{extreme\ baseline} \frac{M_{BEM}}{M_{BEM\ baseline}} \tag{9.4}$$

$M_{extreme\ baseline}$ is the extreme load distribution of the baseline rotor, extracted from full DLB simulations in HAWC2 for the baseline blade. The distribution is fitted with a fourth-order polynomial to ensure that it can be differentiated. The $M_{BEM\ baseline}$ moment is the corresponding maximum steady BEM model retrieved for the same baseline blade.
In the case of the downwind configuration, a second flapwise design load case for cut-out wind speed is considered, as the minimum tower-blade clearance arises in different loading conditions. The load distribution for the maximum deflection

towards the tower $M_{extreme\ deflection}$ is thus scaled from the baseline loads at cut-out wind speed as:

$$M_{extreme\ deflection} = M_{extreme\ baseline\ deflection}\left(2 - \frac{M_{BEM}}{M_{BEM\ baseline\ wsp\ out}}\right) \tag{9.5}$$

For the downwind configuration, a decrease in the loading results into a larger deflection towards the tower.
The edgewise loads remain unscaled, as they are driven by the aerodynamic torque as well as the gravity load.

9.2.3.5 Blade structural design

The simplified blade structural model is based on the work of Blasques and Stolpe (2012), also presented in the thesis work of Carstensen (2017) and Andersen (2018). The blade is described as a sequence of beam elements, each with a cross-section simplified to the elements shown in Fig. 9.3. The main load-carrying structure is simplified as a symmetric girder with two glass-reinforced-plastic (GRP) spar caps, connected by a GRP ellipse. The ellipse major axis is taken equal to the section chord, and the distance between the spar caps taken equal to the section height, thus coupling the structural problem to the aerodynamic planform definition. The structural optimization problem has thus three design variables for each structural section i along the blade: the spar cap thickness t_i and width a_i, and the ellipse thickness e_i. The load cases described in the previous section are applied to the finite beam element model, and the structural optimization aims at minimizing the blade static-mass moment, subject to constraints on: range of the design variables, maximum strain levels on caps and ellipses, maximum tip deflection for the deformed blade and maximum buckling coefficient for a single spar cap. The structural optimization problem can be stated as

$$\begin{aligned} \underset{\vec{a},\vec{t},\vec{e},\in\mathbb{R}^N}{\text{minimize}} \quad & m\left(\vec{a},\vec{t},\vec{e},\right) \\ \text{subject to} \quad & \delta\left(\vec{a},\vec{t},\vec{e},\right) \leq \delta^{max}, \\ & \varepsilon_i\left(a_i,t_i,e_i,\right) \leq \varepsilon^{max}, \quad i=1,\ldots,N, \\ & \eta_i\left(a_i,t_i,\right) \leq \eta^{max}, \quad i=1,\ldots,N \end{aligned} \tag{9.6}$$

with the tip deflection for the deformed blade δ, the strain levels on caps and ellipses ε and the buckling coefficient η.
The buckling coefficient is added to the optimization problem compared to the references. The buckling coefficient is calculated under the assumption of an

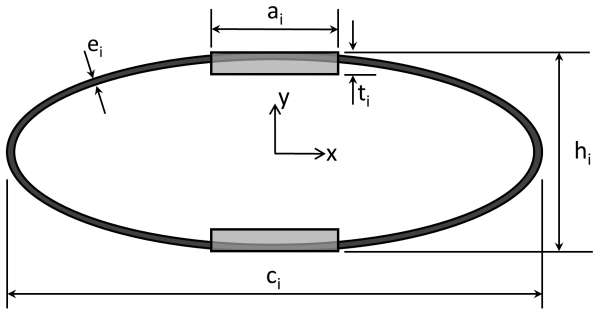

Figure 9.3: Simplified model of the blade structure for each cross section, as applied in STORM. The section height h and chord length c are fixed with the blade geometry for each iteration. The structural optimization design variables are then for each section: the spar caps thickness t_i and width a_i, and the ellipse thickness e_i.

orthotropic plate under compression load. The compression load N_z is obtained from the bending moment, assuming that the internal flapwise bending moment M_x can be distributed as two forces acting on one girder side as compression forces and on the other girder side as tension forces.

$$N_z = \frac{M_x}{h}\frac{1}{a} \tag{9.7}$$

The buckling coefficient η is then obtained via

$$\eta = \frac{6M_x}{\pi^2 Q h}\frac{a}{t^3} \tag{9.8}$$

$$Q = \frac{\nu_{12}E_2}{1-\nu_{12}\nu_{21}} + 2G_{12} + \sqrt{\frac{E_1}{1-\nu_{12}\nu_{21}}\frac{E_2}{1-\nu_{12}\nu_{21}}}$$

with the elastic modulus E, the Poisson ration ν, and the shear modulus G.
The optimization is solved with the Interior Point Optimizer Ipopt (Wächter and Biegler (2006)), and analytical gradients are given for objective and the constraints functions, thus speeding up considerably the process (Blasques and Stolpe (2012)). The solution returns a reliable estimate of the overall blade mass (and hence cost), which is here taken as the objective for the outer optimization loop.

9.2.4 Design evaluation

The optimized planform (chord, twist, and thickness distribution), as well as the changes in the structural geometry (spar cap width, thickness of the spar and trailing edge caps), are applied in HAWTOpt2 according to the planform calculated by STORM. All thickness distributions are fitted by hand at 5 control points and a spline fit is applied in between the control points. The HAWC2 inputs are extracted from HAWTOpt2 and a DLB is calculated for each redesign. From the DLB the maximum load at each blade cross-section is extracted. The failure index is calculated with BECAS for each cross-section. The design is accepted if the failure index i_f is $-1 < i_f < 1$. The failure index calculated by BECAS is not used in the design process.
The DLB calculation is further used to calculate the tower wall thickness w for a tubular tower of given outer wall diameter D. The tower is divided into 50 cross-sections and the outer diameter, as well as the load distribution, are varied linearly between tower top and tower bottom. Within a for-loop, the wall thickness is increased until the stress σ_{steel} reaches the allowed stress of the tower steel material.

$$\sigma_{steel} = \frac{M\ SF}{W_b} \tag{9.9}$$

Where the bending moment M is the bending moment of the cross section, SF is the safety factor for steel material and the W_b is the section modulus calculated as

$$W_b = \frac{\pi}{32} \frac{D^4 - (D - 2w)^4}{D} \tag{9.10}$$

The iteration is done twice, once for the extreme loads and the according stress limit for steel, and once for the lifetime equivalent load from the fatigue calculation and the fatigue stress limit for steel. From the two resulting wall thicknesses, the maximum thickness is picked for each cross-section. Constant masses for the tower interior are added and kept the same as for the baseline. The new tower mass distribution, as well as the stiffness redistribution, do not enter the DLB calculations.

9.2.5 Cost estimation

The cost model used for the cost evaluation consists of costs that scale with the mass, such as tower and blade costs. For other components, the costs scale with a design driving load or measure called cost driver CD. The cost driver is scaled

with a factor $f_{CD\ to\ mass}$ to the component mass $Cost_{component}$. A second factor $f_{mass\ to\ cost}$ is defined to scale component masses to component costs.

$$Cost_{component} = f_{mass\ to\ cost}\,(f_{CD\ to\ mass}\ CD) \tag{9.11}$$

Other cost components e.g. logistics or operation and maintenance costs are scaled directly with the factor $f_{CD\ to\ mass}$ from a cost driver to the cost. Table 9.2 shows the cost drivers for the components entering the applied cost model. All component costs sum up to the capital expenditures (CAPEX). The operation and maintenance costs form the operational expenditures (OPEX). The OPEX costs are calculated with a net present value for a turbine lifetime of 20 years. The COE is calculated from the CAPEX, the OPEX and the AEP of 20 years lifetime.

$$COE = \frac{CAPEX + OPEX}{20AEP} \tag{9.12}$$

The component costs and total turbine costs (CAPEX+OPEX) of the baseline have been compared to the commercial turbine to assure a reasonable cost scaling and cost distribution within the present study.

9.3 Results

The following section presents the resulting design configurations regarding the planforms and resulting blade masses. Further, the design driving loads and the resulting changes in turbine costs and COE are presented. All results are shown relative to the S111uw design configuration, as the data is confidential.

9.3.1 Design configurations

Figure 9.4 shows the planforms resulting from the design workflow. All values are normalized with the maximum chord. The figure shows that the chord and the twist distribution change only slightly, while larger differences can be observed for the thickness over chord distribution, which is likely primarily due to the induction distribution being kept fixed during the optimization, while the larger changes in thickness are due to the direct coupling between AEP constraint, blade structural constraints and blade mass. For the S111uw PF and S111dw PF, the thickness over chord ratio increases from the 70% span and inboard compared to the baseline (S111uw). The S111dw PF has a slightly lower thickness than the

Table 9.2: Cost drivers CD for turbine cost and mass, split by main cost components (* indicates cost that are not scaled within the study due to CD)

turbine component and cost design driver	
nacelle	
gear box incl. cooling*	nominal torque
pitch bearing	maximum static flapwise moment
main bearing	rotor static mass moment
main frame	extreme tilt moment
hub	extreme flapwise moment, blade static mass moment
main shaft	rotor own weight moment
gear rim	extreme yaw moment, tower top diameter
yaw drives	extreme yaw moment
pitch drives	maximum pitch moment, maximum pitch rate
converter*	nominal power
nacelle nose cone cover*	nominal power
power cables*	nominal power, tower height
lift*	tower height
electrical	
generator*	nominal power
bottom panel*	nominal power
top panel*	nominal power
hub panel	maximum pitch moment, maximum pitch rate
transformer*	nominal power
blades	mass 70% (30% constant labor cost)
tower	mass
civil (foundation)	extreme tower bottom bending moment
cost component and cost design driver	
logistics	nacelle mass, blade length* tower height*
electrical balance of plant	
yard*	blade length squared
electrical lines*	nominal power, average length of lines
installation (main crane)	nacelle mass times tower height
Operation and maintenance (OPEX)*	AEP

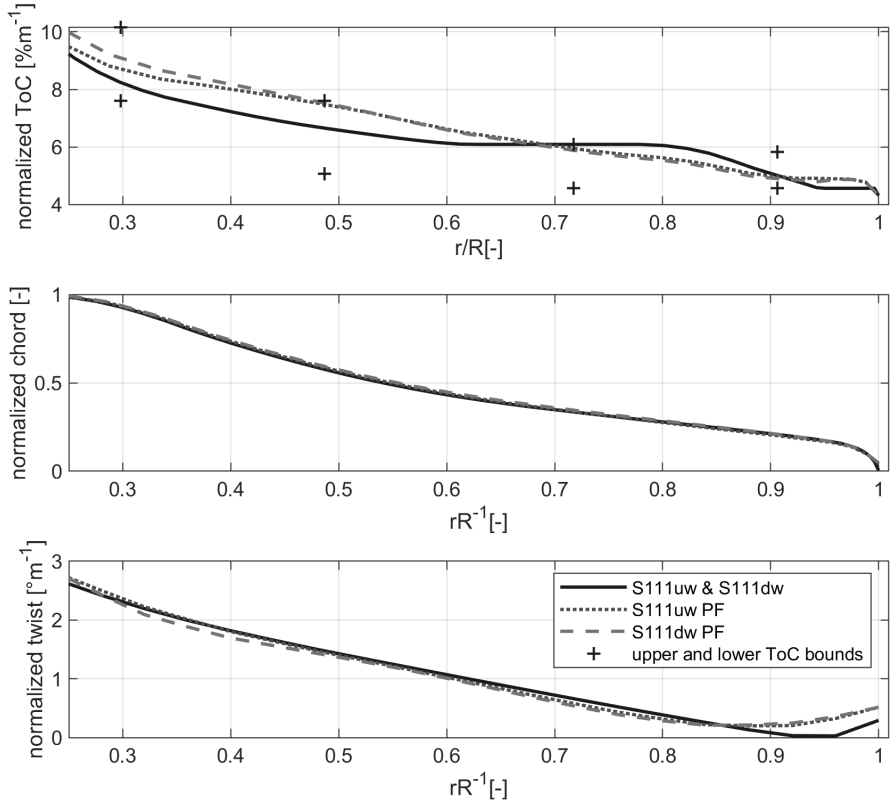

Figure 9.4: Comparison of planforms for different designs. Thickness over chord ratio as well as the range of the thickness constraints, chord and twist are normalized with the maximum chord.

S111uw PF design in this area up to the tip. From 40% span and inboard to the displayed region the S111dw PF design shows a larger thickness over chord ratio than the S111uw PF design. In the outer 8% of the blade span, the PF redesigns show a larger thickness than the baseline blade. The latter is an artifact of the combination of the spline type chosen and the fixed airfoil thickness at the blade tip. For none of the redesigns the constraint on thickness over chord is active.
While the S111uw PF design is constrained in blade deflection, in none of the downwind designs the blade deflection constraint is active. All the resulting redesigns are generally utilizing the maximum strain of the material over a larger blade span than the S111uw and S111dw design configurations. All downwind redesigns are fully strain constrained in the spar caps. In the structural module of the optimization, the buckling constraint is active along the full blade span. The downwind configurations generally show larger shell thickness than the upwind configuration.
For all redesigns of the rotor blade, significant savings could be achieved of at least 12%. The lowest blade mass savings are achieved by the upwind configuration. For the S111uw PF 12.5% of blade mass could be saved. For the S111dw STR 14.5% mass savings are achieved and 17.1% blade mass reduction was observed for S111dw PF. Table 9.4 summarizes the blade masses for all design configurations together with other achieved data.
The planform redesigns utilize higher stiffness with less material by using thicker airfoils in the inboard part. In the outboard part thinner, more efficient airfoils compensate for a production loss of the inboard part of the blade. This effect is amplified as a small AEP penalty was allowed in the design procedure. From the S111dw STR, it can be seen that the downwind configuration benefits from lower flapwise loads, and a release of the tower clearance constraint resulting in a reduced blade mass. A higher shell thickness is required to carry the higher edgewise loads in the downwind configurations. Comparing the S111dw PF design to the S111uw PF design a further effect of the edgewise load increase can be seen. To carry the increased edgewise loads there are two options. The first one is to increase the shell thickness as for the S111dw STR design. The second option is to increase the stiffness by using airfoils with higher relative thickness. The solution found in the optimization routine for the S111dw PF is a combination of both, showing slightly thicker airfoils on the inboard part for the S111dw Pf than for the S111uw PF. Another solution to carrying the increased edgewise loads is an increased chord, but since the variation in chord is limited due to a fixed induction and tip speed ratio, this design freedom is not utilized. The lower flapwise loads in the S111uw PF design allow, on the other hand, to compensate for a power loss with slightly thinner airfoils in the outboard part. The chord distribution is hardly changing as the AEP is constrained to not deviate from the baseline AEP and the induction distribution is frozen. The twist is simply

adjusting the given operational point of the airfoils at the given spanwise position.

9.3.2 Cost driving loads from full DLB calculation

The following section shows the loads driving either the cost components in Table 9.2 or the designed tower and blade mass. For all regarded designs the minimum tower clearance is guaranteed. For all loads entering the cost model either directly or via the mass calculations DLC1.3, the operation at extreme turbulence remains design driving. The only exception is the extreme blade root torsion moment where load cases of operation during wind direction change, operation at extreme yaw errors or yaw errors during parked situations with a locked rotor (DLC 1.4, DLC 2.2y or DLC 7.1) are design driving. Table 9.3 shows the loads influencing the cost estimation of the designs relative to the S111uw configuration. It can be seen, that the S111uw PF design clearly benefits, from the reduced

Table 9.3: Turbine loads for mass and cost drivers, Blade root moment (BRM), tower bottom bending moment (TBM), tower top moment (TTM)

load sensor	Δ normalized load relative to S111uw configuration			
	S111uw PF	S111dw	S111dw STR	S111dw PF
max. mean flapwise BRM	-0.03	-0.40	-0.38	-0.35
extreme flapwise BRM	-0.01	-0.17	-0.19	-0.18
extreme edgewise BRM	-0.12	+0.08	+0.02	-0.06
extreme torsion BRM	-0.18	+0.50	-0.18	-0.06
extreme TTM yaw	+0.08	-0.06	-0.09	-0.08
extreme TTM tilt	-0.09	+0.27	+0.15	+0.14
extreme TBM longitudinal	-0.04	+0.10	+0.07	+0.07
fatigue flapwise BRM	-0.02	+0.05	+0.00	+0.00
fatigue edgewise BRM	-0.11	+0.06	+0.00	-0.10
fatigue TTM tilt	-0.01	+0.06	+0.06	+0.05
fatigue TBM longitudinal	-0.01	-0.05	-0.07	-0.07

blade mass on the edgewise extreme and fatigue blade root bending moment, as well as on the tower bottom bending moment. The only disadvantage is an increase in the tower top yaw moment.
The table also shows that the downwind designs generally benefit on the flapwise

mean, flapwise extreme blade root moment and the related tower top yaw moment, mainly from the alignment of the rotor cone and the rotor forces ("load alignment"). In the tower top tilt moment, the influence of the tower shadow, as well as the alignment of the rotor overhanging gravity moment and the moment due to thrust force is observed. Due to the latter also an increase in the extreme tower bottom bending moment is seen compared to the S111uw design. The gravity-related loads, e.g. tower top tilt moment and longitudinal tower bottom bending moment are reduced for each configuration by the reduction of mass due to the redesign. With the reduced flapwise stiffness of the S111dw PF design, the fatigue load is reduced to the level of the S111uw and the tower shadow effect is overcome. A relative reduction of the flapwise stiffness compared to the edgewise stiffness increases the edgewise damping which results in the load decrease for edgewise extreme and fatigue loads of the S111dw STR and S111dw PF compared to the S111dw.

9.3.3 Turbine mass, cost and COE estimate

This section shows the estimated costs resulting from the load and mass difference of the design configurations. Figure 9.5 shows the summary of the main cost components of the turbine with an indication of the cost that is not affected by the design process (constant cost). The costs sum up to the total CAPEX. All results are normalized by the CAPEX of the S111uw design. It can be seen that the nacelle is the main cost component, followed by the blades, the tower, and the costs for electrical equipment. The figure shows that more than a third of the CAPEX is not affected by the chosen redesigns. In the CAPEX distribution of the nacelle, major cost differences are associated with the pitch bearing, the mainframe and the pitch drives. The blade costs reduce significantly with the redesign of the blades. Where the S111dw PF shows the lowest blade costs associated with the lowest blade mass. The tower and foundation costs are for the downwind configurations generally higher than for the upwind configurations, as the associated extreme loads and also the tower top fatigue loads are significantly higher. The costs of the electrical components reflect the change in hub panel costs as these scale with the extreme blade root torsion. Only small differences in the logistics costs are observed due to the change in nacelle mass. The balance of the plant is achieved for the same estimated costs while the installation reflects the changes in total main frame mass, driven by the extreme tilt moment. Overall, the total CAPEX costs of the turbine vary only marginally between all the redesigns. The OPEX costs, on the other hand, are lower for all the downwind designs since the OPEX costs scale with the lower AEP. As a result, the combined turbine

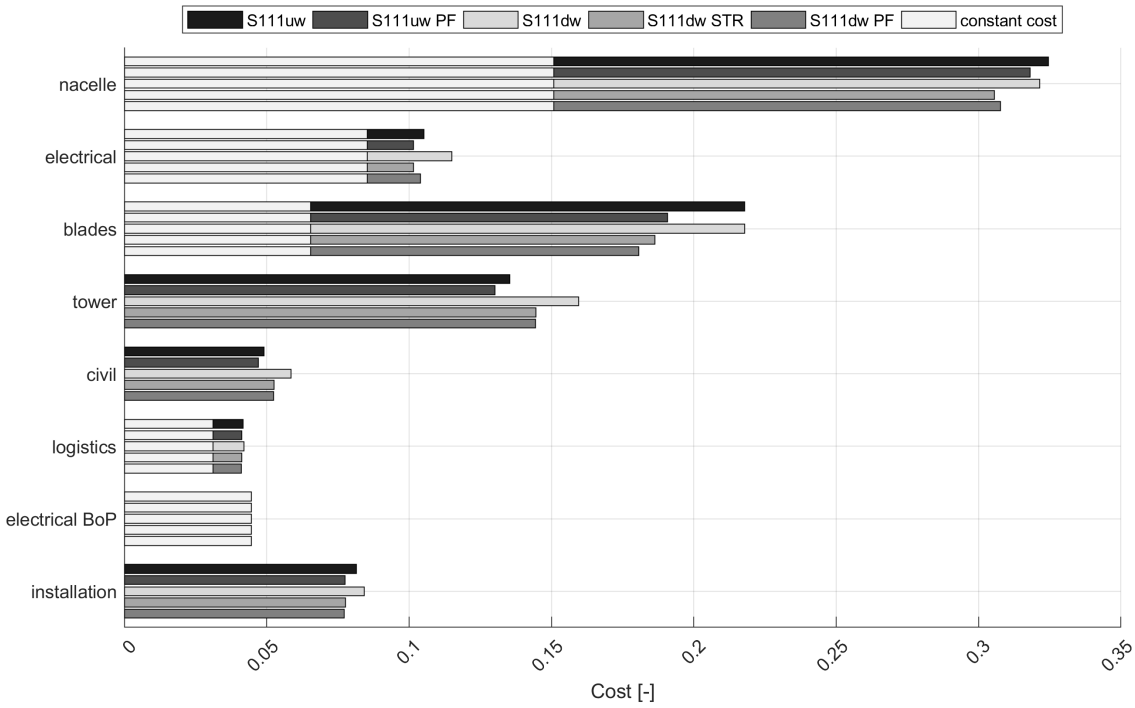

Figure 9.5: Turbine CAPEX cost split by main cost components normalized by the sum of the S111uw configuration with indication of constant costs not affected by redesign process.

costs of the redesigned downwind configurations (S111dw STR and S111dw PF) are lower than for the S111uw PF design.
Table 9.4 summarizes the achieved blade and tower mass, as well as the AEP and the estimated COE differences compared to the S111uw design. With a

Table 9.4: Blade mass, Tower mass, CAPEX, AEP and COE difference for the regarded turbine configurations, relative to the S111uw design.

Name	Δ blade mass [%]	Δ tower mass [%]	Δ AEP [%]	Δ COE [%]
S111uw PF	-12.5	-3.9	-0.33	-2.3
S111dw	0.0	+17.8	-2.0	+3.1
S111dw STR	-14.5	+6.8	-2.32	-1.2
S111dw PF	-17.1	+6.6	-2.37	-1.3

COE reduction of -2.3% the S111uw PF shows the lowest COE, as the CAPEX is low, while the AEP is high. A pure configuration change from S111uw to S111dw is most expensive in terms of COE, due to the high CAPEX mainly caused by high tower and foundation loads. A structural redesign of the blades for the downwind configuration achieves significant COE savings of -1.2%, due to reduced rotor mass. A planform optimization of the downwind configuration reduces the COE -1.3% below the S111uw baseline turbine. Overall, the S111uw PF remains of lowest COE, since the rotor mass is only 5% above the S111dw PF while the tower is 10% lighter and the AEP is 2% higher.

9.4 Summary

Within this study, the COE reduction potential for the Suzlon S111 2.1MW turbine has been estimated changing the original upwind configuration into a downwind configuration. A design framework including a low fidelity in-house optimization tool has been used to redesign rotors for upwind and downwind configurations. A full design load basis has been simulated for every design configuration. The design configurations have been evaluated by a COE estimation. New planforms were optimized for upwind and downwind configurations for minimum blade mass under the constraint of a minimum AEP. The new planforms were shown to have higher thickness over chord ratios inboard, utilizing higher stiffness with less material. This design trend agrees well with findings by Bottasso et al. (2016) and Zahle et al. (2016).
The downwind design were generally subject to lower flapwise blade root moments than the comparable upwind designs, due to the coning direction, as also

proposed by for example Ichter et al. (2016) and Bortolotti et al. (2019). As a result lower blade mass could be achieved for downwind configurations than for upwind configurations. The S111dw PF design showed, for example, 4.6% lower blade mass than the S111uw PF design.
The load saving on the blade in the downwind configuration is offset by an increase in the tower bottom bending moment as the gravity overhanging moment of the rotor nacelle assembly is aligned with the thrust force, as also shown by Ning and Petch (2016). As a result around 10.5% higher tower masses were seen in the direct comparison of the S111uw PF design and the S111dw PF design.
The downwind configurations are subject to a lower AEP production due to the coning direction. This effect has also been observed by for example Zalkind et al. (2019) or Ning and Petch (2016). In the direct comparison, the AEP of the S111dw PF is 2.04% lower than the AEP of the comparable S111uw PF.
Lower rotor and nacelle costs can be achieved by the downwind designs. However, the downwind designs also come with higher tower and foundation costs. Overall, the downwind configurations of comparable rotor size achieve a lower total turbine cost than the upwind design configuration. The difference in cost is due to the lower OPEX cost and does heavily depend on the cost model. Overall the lower turbine cost does not compensate for the loss in AEP. The lowest COE level is achieved by the S111uw PF design configuration which achieves a significant mass and load reduction for a small sacrifice in AEP compared to the baseline.

9.5 Discussion and future work

This study has shown, for the example of the Suzlon S111 2.1MW turbine, that a downwind rotor configuration could be achieved with lower total turbine costs than the comparable upwind configuration. Due to a lower AEP of the downwind configurations, the upwind configuration, on the other hand, showed overall the lowest COE. A downwind configuration would, therefore, be the configuration to choose on a turbine cost-driven market, while for COE driven markets the upwind configuration would be chosen.
These results depend on the very baseline specific cost model. Scaling the OPEX with the AEP has been the only cost driver for the OPEX which results in the lower turbine costs for the downwind configuration. It could be expected, that the higher fatigue load of the downwind configuration would increase the material wear, but this does not enter the OPEX model.
The cost model generally depends on the loads simulated. This comes with uncertainty due to the seed number, the seeds themselves as well as and the assump-

tions of wind field inclination angle. In the case of the downwind configuration additionally, the dynamic effect of the tower shadow is not captured correctly within the HAWC2 simulations. Within HAWC2 the tower shadow model for downwind configurations is a pure deficit model and the increased vorticity behind the tower is not reflected. It can be expected that especially flapwise blade root and tilt related fatigue loads are under-predicted. Further research would need to be done to quantify the impact of this effect.
Generally fatigue loads should be part of the design process in future work. In the chosen approach fatigue loads are not regarded in the design process and hardly reflected in the cost model. This might be a valid assumption in the upwind configurations, but for downwind configurations, this approach needs to be proven. Due to the tower shadow effect as well as a possible decrease in edgewise damping, it might be possible that rotors of downwind configurations are driven by edgewise fatigue loads rather than flapwise extreme loads.
Prescribing the induction distribution in the optimization is a major restriction of the chosen design approach. The resulting chord and twist distributions are therefore very similar. The induction should be a design variable in future work as unloading the tip might allow for increases in rotor diameter and therefore AEP increase. The latter does not just hold for the downwind configuration, but also for the upwind configuration.
Prescribing the induction distribution did, however, have the advantage that the load scaling approach was possible. Scaling loads from the BEM-code loads to the extreme loads has decreased computation time significantly. A drawback of the load scaling approach is that a change in aerodynamic damping is not reflected. For the downwind configuration the flapwise stiffness could be significantly reduced, while the edgewise stiffness had to be increased, the edgewise whirl modes can, therefore, be expected to increase in damping due to the frequency placement of the edgewise frequency compared to the second yaw frequency. An increase in damping decreases the blade extreme loads. The effect of the loads has been observed in the downwind designs, but there is no feedback within the optimization reflecting the change in damping. In future work, the framework would need to be enhanced with either time consuming load calculations or with a set of transfer functions that can transfer a wind field to extreme loads from a linearized turbine model. Such a linearized turbine model could be extracted for example from HawcStab2 which uses these models for eigenvalue analysis. In this case, a representative wind field could be used that represents extreme loads from a simulation set with a much larger seed number and with known uncertainty. This would decrease the computational time drastically while achieving reasonable results.
The COE estimation and therefore success criteria of the downwind concept does also depend on the cost-share between the different components. Since in the

chosen example turbine the rotor and the tower are similar in the CAPEX share, it is difficult in the downwind configuration to offset the increased tower cost with savings on the rotor. If the baseline had a comparably more expensive rotor and a cheaper tower, the downwind configuration would be more competitive. Possible scenarios could be lower steel prices or higher blade material prices.
Another possibility to increase the competitiveness of the downwind configuration would be a change in the tower configuration, such as a wired tower, where wires are a cheap measure to take the bending loads. Alternatively, a low labor cost market could give the options of low tower costs with lattice or hybrid-lattice towers which generate bending stiffness from an increased foot-print of the tower, rather than large tower wall thicknesses for a tubular tower. These options could make the downwind configuration competitive as the cost share of the tower decreases. However, the cost model with the chosen baseline is not able to reflect such drastic design changes.
Compensating the AEP loss in the downwind configuration with a larger rotor area could be an option to decrease the COE. Nevertheless, this does also increase the turbine cost, not just due to an increased rotor diameter and therefore rotor mass, but also mass related loads such as tilt loads and tower base loads. The rotor diameter has not been part of the rotor design as the cost model is very specific and does not reflect large differences from the baseline. Especially for components such as generator or gearbox which are not available in any possible configuration but are bought as "off-the-shelf" components the linear cost scaling is insufficient. A rotor diameter increase of 4% has been investigated, indicating the potential to decrease the COE for the downwind configurations further with an increase of rotor diameter.
Future work should also consider a redesign of the nacelle for better balancing of the rotor mass on the tower for the downwind configuration, as suggested by Zalkind et al. (2019). However, it should be kept in mind, that the upwind configuration will always be beneficial in terms of tower bottom bending moment. Masses that can not be relocated for balancing such as rotor, hub, pitch, and yaw system related masses account for around 50% of the mass of the rotor-nacelle assembly. Extending the lengthwise dimensions of the remaining components to relocate the center of gravity might be more expensive than the higher tower costs of downwind configurations.
It should not be forgotten in the discussion of the cost efficiency of downwind configurations, that simple control features such as peak shaving, as suggested by Loenbaek et al. (2019) might benefit the upwind configuration in the same manner as the configuration change: the tower clearance is increased, the flapwise blade root moment is decreased with a penalty on AEP. Since the tower bottom load does in this case not increase as in the case of the downwind configuration, such an upwind configuration might out-perform a downwind configuration in

terms of COE.

9.6 Conclusion

Overall, the study shows, that a downwind configuration of the chosen example 2.1MW turbine would need to be pushed to much larger rotor sizes than investigated. Further, low-cost measures would need to be chosen to carry the increased tower loads if the downwind configuration should become competitive in terms of COE with the comparable upwind configuration.
The optimization framework would need to be extended to be able to capture the design changes regarding the rotor, but also different tower configurations need to be included. To be able to evaluate such changes, a more comprehensive cost model is required to do a fair comparison of the designs.
It can be concluded from the study, that it will be difficult to design a downwind configuration in the 2MW range, which can show significant economic benefits unless the design targets a different market than the upwind configuration, or more drastic changes are made than just a rotor redesign and a structural redesign of the tower.

Data availability. The data is not publicly accessible, since the research is based on a commercial turbine and the data is not available for disclosure by Suzlon.

Bibliography

Andersen, M. (2018). Conceptual aerodynamic and structural design optimization of wind turbine blades. Master's thesis, Technical University of Denmark (DTU), Roskilde, Denmark.

Blasques, J. (2011). Optimal design of laminated composite beams. *PhD thesis, Technical University of Denmark*, DCAMM Special Repport, No. S134.

Blasques, J. P. and Stolpe, M. (2012). Multi-material topology optimization of laminated composite beam cross sections. *Composite Structures*, 94(11):3278–3289. https://doi.org/10.1016/j.compstruct.2012.05.002.

Bortolotti, P., Kapila, A., and Bottasso, C. L. (2019). Comparison between

upwind and downwind designs of a 10 mw wind turbine rotor. *Wind Energy Science*, 4(1):115–125. https://doi.org/10.5194/wes-4-115-2019.

Bottasso, C. L., Bortolotti, P., Croce, A., and Gualdoni, F. (2016). Integrated aero-structural optimization of wind turbines. *Multibody System Dynamics*, 38:317–344. https://doi.org/10.1007/s11044-015-9488-1.

Bottasso, C. L., Croce, A., and Sartori, L. (2015). Free-form design of low induction rotors. *Wind Energy Symposium*, 33:1–8. https://doi.org/10.2514/6.2015-0488.

Carstensen, C. (2017). Large scale structural topology optimization of wind turbine blades with eigenfrequency constraints. Master's thesis, Technical University of Denmark (DTU), Roskilde, Denmark.

G. Kolda, T. (2014). A generating set direct search augmented Lagrangian algorithm for optimization with a combination of general and linear constraints. https://doi.org/10.1.1.146.2289.

Glasgow, J., Miller, D., and Corrigan, R. (1981). Comparison of upwind and downwind rotor operations of the doe/nasa l00-kw mod-0 wind turbine. *NASA Report*, TM-8744:225–234.

Greene, G. C. (1981). Measured and calculated characteristics of wind turbine noise. *NASA Report*, CP-2185.

Hansen, M. (2004). Aeroelastic stability analysis of wind turbines using an eigenvalue approach. *Wind Energy*, 7:113–143. https://doi.org/10.1002/we.116.

Hansen, M. (2008). Aerodynamics of wind turbines. *Earthscan*, pages 44–62. edition 2.

Hansen, M. and Henriksen, L. (2013). Basic dtu wind energy controller. *DTU-Wind-Energy-Report*, E-0028.

Hansen, M., Thomsen, K., Natarajan, A., and Barlas, A. (2015). Design load basis for onshore turbines revision 00. *DTU Report; DTU Wind Energy*, E-0074.

Ichter, B., Steele, A., Loth, E., Moriarty, P., and Selig, M. (2016). A morphing downwind-aligned rotor concept based on a 13-mw wind turbine. *Wind Energy*, 19:625–637. https://doi.org/10.1002/we.1855.

IEC (2014). Iec 61400-1 ed.3 wind turbines- part1: Design requirements. Technical report, International Electronical Commission.

Loenbaek, K., Bak, C., Madsen, J. I., and Dam, B. (2019). Optimal relationship between power and design driving loads for wind turbine rotors using 1d models. *Wind Energy Science Discussions*, 2019:1–29. https://doi.org/10.5194/wes-2019-28.

Loth, E., Steele, A., Qin, C., Ichter, B., Selig, M. S., and Moriarty, P. (2017). Downwind pre-aligned rotors for extreme-scale wind turbines. *Wind Energy*, 20:1241–1259. https://doi.org/10.1002/we.2092.

Madsen, H. A., Larsen, T. J., Pirrung, G. R., and Zahle, F. (2019). Implementation of the blade element momentum model on a polar grid and its aeroelastic load impact. *Wind Energy Science Discussion*. https://doi.org/10.5194/wes-2019-53, in review.

Metzger, F. and Klatte, R. (1981). Status report on downwind horizontal axis wind turbine noise prediction. *NASA Report*, N82-23684 14-44:425–430.

Ning, A. and Petch, D. (2016). Integrated design of downwind land-based wind turbines using analytic gradients. *Wind Energy*, 19:2137–2152. https://doi.org/10.1002/we.1972.

Ning, S. A. (2014). A simple solution method for the blade element momentum equations with guaranteed convergence. *Wind Energy*, 17(9):1327–1345.

Reiso, M. and Muskulus, M. (2013). The simultaneous effect of a fairing tower and increased blade flexibility on a downwind mounted rotor. *Journal of Renewable and Sustainable Energy*, 5(3):033106–1–1033106–11. https://doi.org/10.1063/1.4803749.

Tibalidi, C., Hansen, M. H., and Henriksen, L. C. (2014). Optimal tuning for a classical wind turbine controller. *Journal of Physics: Conference Series 555; p.1-11*. https://doi.org/10.1088/1742-6596/555/1/012099.

Wanke, G., Bergami, L., Larsen, T. J., and Hansen, M. H. (2019a). Changes in design driving load cases: Opterating an upwind turbine with a downwind rotor configuration. *Wind Energy*, 22:1500–1511. https://doi.org/10.1002/we.2384.

Wanke, G., Bergami, L., and Verelst, D. R. (2019b). Differences in damping of edgewise whirl modes operating an upwind turbine in a downwind configuration. *Wind Energy Science Discussions*, 2019:1–19. https://doi.org/10.5194/wes-2019-88.

Wanke, G., Hansen, M. H., and Larsen, T. J. (2019c). Qualitative yaw stability analysis of free-yawing downwind turbines. *Wind Energy Science*, 4(2):233–250. https://doi.org/10.5194/wes-4-233-2019.

Wächter, A. and Biegler, L. T. (2006). On the implementation of an interior-point filter line-search algorithm for large-scale nonlinear programming. *Mathematical Programming*, 106(1):25–57. https://doi.org/10.1007/s10107-004-0559-y.

Zahle, F., Tibaldi, C., Verelst, D., Bak, C., Bitsche, R., and Blasques, J. (2015). *Aero-Elastic Optimization of a 10 MW Wind Turbine*, volume 1, pages 201–223. American Institute of Aeronautics & Astronautics.

Zahle, F., Tibalidi, C., Pavese, C., McWilliam, M. K., Blasques, J. P. A. A., and Hansen, M. H. (2016). Design of an aeroelastically tailored 10mw wind turbine rotor. *Journal of Physics: Conference Series 753; p.1-11.* https://doi.org/10.1088/1742-6596/753/6/062008.

Zalkind, D., Ananda, G. K., Chetan, M., Martin, D. P., Bay, C. J., Johnson, K. E., Loth, E., Griffith, D. T., Selig, M. S., and Pao, L. Y. (2019). System-level design studies for large rotor. *Wind Energy Science*, 4:595–618. https://doi.org/10.5194/wes-4-595-2019.

9.7 Appendix

The following Table 9.5 states the symbols used in the equations.

Table 9.5: List of symbols used in the STORM model

Greek symbol	definition
α	angle of attack
β	pitch angle
ε	material strain
δ	blade deflection
η	buckling coefficient
ν	Poisson ratio
σ_{steel}	steel material stress
Latin symbol	definition
a	spar cap width
CD	cost driver
D	outer tower diameter
e	shell thickness
E	elastic (Young's) modulus
f	cost scaling factor
G	shear modulus
h	section height
ind	induction
m	mass
M	local mending moment
N	number of cross sections
N_z	buckling load
SF	safety factor
t	spar cap thickness
w	tower wall thickness
W_b	section modulus

Author Contributions. GW has created the baseline model and implemented the downwind design case in the optimization framework. LB has developed and set-up the optimization framework. FZ has set-up HAWTOpt2 framework for baseline and design case evaluation. All authors have revised the models and results. With revisions of all co-authors GW and LB prepared section 2.3, GW prepared the remaining paper.

Competing interests This project is an industrial PhD project funded by the Innovation Fund Denmark and Suzlons Blade Science Center. Gesine Wanke is employed at Suzlons Blade Science Center.

Appendix A

List of papers

Within the PhD the following articles have been published:

Changes in design driving load cases: Operating an upwind turbine with a downwind rotor configuration; Gesine Wanke, Leonardo Bergami, Torben J. Larsen and Morten H. Hansen; *Wind Energy*; Vol. 22; p. 1500-1511; DOI: https://doi.org/10.1002/we.2384

Wanke, G., Hansen, M. H., and Larsen, T. J.: **Qualitative yaw stability analysis of free-yawing downwind turbines**, *Wind Energy Science*, 4, 233-250, https://doi.org /10.5194 /wes-4-233-2019, 2019

Within the PhD the following manuscripts have been submitted:

Wanke, G., Bergami, L., and Verelst, D. R.: **Differences in damping of edgewise whirl modes operating an upwind turbine in a downwind configuration**, *Wind Energy Science Discussion*, https://doi.org/10.5194/wes-2019-88, in review, 2019

Wanke, G., Bergami, L., Zahle, F., and Verelst, D. R.: **Re-design of an upwind rotor for a downwind configuration: design changes and cost evaluation**, *Wind Energy Science*,2019